UNIVERSITY OF CALIFORNIA
Los Angeles

Simultaneous Transmission of Robust Wireless Power that is Immune to Coupling and Load Variations and Reverse High-Speed Low-Power Wireless Data over One Pair of Coils

A dissertation submitted in partial satisfaction
of the requirements for the degree
Doctor of Philosophy in Electrical and Computer Engineering

by

Jiacheng Pan

2018

ABSTRACT OF THE DISSERTATION

Simultaneous Transmission of Robust Wireless Power that is Immune to Coupling and Load Variations and Reverse High-Speed Low-Power Wireless Data over One Pair of Coils

by

Jiacheng Pan
Doctor of Philosophy in Electrical and Computer Engineering
University of California, Los Angeles, 2018
Professor Asad A. Abidi, Chair

In this work, a general theory of coupled resonators is proposed. On one hand, it provides a design-oriented analysis while also preserving rigorousness throughout the derivation; on the other hand, it uses graphical methods to offer an intuitive understanding. Using an impedance loci analysis, it then ties the above to aspects together to render an integrated body of theory.

Guided by the developed theory, a robust wireless power transfer system using an oscillator driver is designed, capable of providing more than 90 mW of power to a brain implant. Its maximum operating range spans 4.2 cm and handles up to 40× load variations. It achieves a peak efficiency of more than 80%.

Building upon this wireless power system, a novel data modulation, Load-Induced Resonance-Shift Keying (L-RSK) is implemented to transmit reverse data simultaneously with the forward regulated power, at high rate and low power, through the same pair of coils. It can support up to 5 Mb/s data rate and burns negligible power (at most 0.395 mW) compared with the total delivered amount.

The milli-Watt level wireless power for biomedical implants can be extended to Watt level so that it can be used for charging portable consumer electronics. The scaled system can provide up to 11 W power with 85% peak efficiency.

Lastly, second harmonics in LC oscillators are analyzed. Analysis on the second harmonics at the output and at the tail current source of current-mode LC oscillators provides useful insights on how to improve power-conversion efficiency. Anslysis on the second harmonics in oscillators with mismatch in threshold voltages of FETs shows that flicker noise at switching FETs of an LC oscillator can be up-converted to become phase noise at the output of the oscillation.

The dissertation of Jiacheng Pan is approved.

Danijela Čabrić

Dejan Marković

Sudhakar Pamarti

Asad A. Abidi, Committee Chair

University of California, Los Angeles

2018

"Ten thousand years are too long.

Seize the day, seize the hour!"

– Man Chiang Hung

TABLE OF CONTENTS

LIST OF FIGURES

LIST OF TABLES

ACKNOWLEDGMENTS

I would like to express my sincere gratitude to Prof. Abidi, who allowed me the freedom to explore the area which I was interested in, guided me patiently with his wisdom, motivated me when I was in depression, and taught me to have faith in the power of theory. I feel so fortunate that I was able to meet him when taking introductory-level circuit course eight years ago, and got the chance to be educated by him since then. His passion and excitement in electric circuits, in what he loves, have greatly influenced me, and I've learned from him how to solve problems intelligently rather than being lost in the maelstrom of mindless trial and error.

I want to thank Prof. Marković for the wonderful opportunities to realize my thoughts into actual systems. Galileo Galilei once said "I think that in the discussion of natural problems we ought to begin not with the Scriptures, but with experiments, and demonstrations." Without actual implementation and experiments, even the most beautiful theory will find itself standing upon pillars of sand. I also thank him for teaching me to always keep an eye on the practicalness of research in real-world applications.

I would like to thank Prof. Pamarti, who can always offer me a different perspective to look at or understand the same problem, even after having seen it for a long time. The EE215E class taught by him was the first time for me to go through the entire process of system design: first understanding the background theory, then devising the general system, and finally delving into the detailed circuit designs. I've truly benefited a lot from that experience.

I also want to thank Prof. Čabrić for her kindness, and for being on my committee and offering me precious advice. In her EE209AS class, I thoroughly learned about different types of data communication. Without a good understanding of that, I will never be able to invent any new data modulation scheme. I really appreciate her help.

Prof. Chih-Kong Ken Yang, though not on my dissertation committee, offered me a lot of help. I would like to thank him for that. Minji Zhu made it very convenient and smooth for

me when I wanted to rent devices or use various services from CHFE such as wire-bonding, board fabricating, etc. I really appreciate that.

I am also very grateful for the help from my colleagues and my friends. It is so difficult to thank everyone in the limited pages here, but here I would like to acknowledge the help by some of them who are directly related to the work described in this dissertation: Weiyu Leng helped me with the design of coils. Wenlong Jiang helped with the digital implementations of control circuits of AAC in the wireless power system and the L-RSK demodulators. Yi Li implemented and tested the Watt-level wireless power system, and I was very impressed with his ability to understand new concepts and implement PCBs quickly. Zhiwei Zhang helped with the verification of some digital systems. Kejian Shi helped me with the measurement of system's EM radiations and the FCC requirement check. I have worked closely with Dejan Rozgić, Vahagn Hokhikyan, Sina Basir-Kazeruni, Hariprasad Chandrakumar, Alireza Yousefi, Sam Barclay and Ahmed Al Zuhair on the project of brain implant. It was a wonderful experience working with them, and I want to thank them for their generous help. I have had many discussions with Hao Xu, Qaiser Nehal, Usama Anwar, Uneeb Rathore, Daisong Zhang, Alvin Chen, Xiao Wang, Dihang Yang, Yikun Chang, Long Kong, Wenhao Yu, Shaodi Wang, Min Gao, Heng Zhao, Yilei Li, Shengzhe Jiao, Rui Zhu, Mahmoud Elhebeary, Szu-Yao Hung, Jieqiong Du, Shi Bu, Hani Esmaeelzadeh, Neha Sinha, Soheil Golara, Mohammadhasan Fayazi, Liangxiao Tang, and Jiyue Yang, etc. on various different topics; these discussions form great inspirations for my research.

VITA

2013	B.S. (Electrical Engineering), UCLA. (*Summa Cum Laude*)
2015	M.S. (Electrical Engineering), UCLA. (Outstanding Master's Thesis in Circuits and Embedded Systems)
2015 – present	Ph.D. Candidate (Electrical and Computer Engineering), UCLA.

CHAPTER 1

Introduction

1.1 Motivation of this Research

Next-generation biomedical implants for the brain-computer interface (BCI) can sense neural signals and stimulate the brain accordingly [1, 2, 3, 4]. To support all these functions in a long-term treatment, it is desired that the implant is wirelessly powered by an external piece. Furthermore, a reverse wireless data link provides non-stop monitoring of the patient's state with the potential of optimizing the stimulation therapy. To shed light on a quantitative understanding of the requirements by the wireless power/data interface, a state-of-the-art brain implant [5] can be used as an example.

Let's look at the fundamental requirements for the power/data link. In terms of power, the neuromodulator has four stimulation engines in total, each consuming up to 1.8 mW of power. That amounts to 7.2 mW in total. To give it some extra margin, the link should aim at delivering ~ 20 mW. In terms of data, to sense local-field potential signals, the neuromodulator has 32 channels, each sampling the neural activity at 500 samples/sec with 10-12 bit resolution, which amounts to 192 kb/s data rate in total. To allow for margin, the link should support ~ 1 Mb/s data rate.

Moreover, it's desired that the wireless power and data can be robust. This means several additional requirements must be met:

1. Due to patient's motion, the external piece may change its location or angle with respect to the implant. Wireless power delivery should remain stable over a reasonable range.

2. The implant may often switch in between sensing and stimulating modes, consuming significantly different levels of power. The wirelessly delivered voltage supply should remain the same over mode-changing.

3. Simultaneously with the forward wireless power, the reverse high-rate data should be transmitted using minimum power compared with the total delivered power.

1.2 Contribution of this Work and Organization of this Dissertation

Motivated to build a robust wireless power and data link for the system described above, a general theory on the operation and properties of coupled resonators was first developed (Chapter 2). The theory aims at providing a design-oriented analysis that tries to organize every equation in a low-entropy form; also, it aims at providing some insights and intuitions by utilizing graphical methods.

Having developed the theory, a robust wireless power transfer system was designed that achieved the goal of robust wireless power immune to both distance/alignment variations and load variations. The wireless power system also largely overcame the trade-off between the ability to handle the two variations mentioned above, and details will be explained in Chapter 3.

With the wireless power ready, in order to transmit reverse data at the same time, a new data modulation scheme, what's called Load-Induced Resonance-Shift Keying (L-RSK) was then developed (Chapter 4). This novel data modulation solved the problem of being unable to simultaneously deliver robust wireless power and transmit reverse data through the same pair of coils.

Furthermore, the design methodology of wireless power has proven itself to be robust. The original wireless power system designed for mW-level products such as brain implants can be easily scaled up to Watt-level applications. A wireless charging system that provides up to 11 mW was developed and tested (Chapter 5).

As will be shown later, key to the designs of wireless power or data systems is a free-running oscillator driver. More theories on the second harmonics in LC oscillators were also developed and will be discussed in Chapter 6.

CHAPTER 2

A General Theory of Coupled Resonators

2.1 Existing Analyses on Coupled Resonators and Organization of Theories Introduced in this Chapter

The analysis of coupled resonators dates back to as early as 1940s when people were actively researching on using coupled resonators to implement analog filters, etc. N. I. Korman in 1943 [6], G. E. Valley et al. in 1948 [7], R. Martin et al. in 1952 [8], S. B. Cohn in 1957 [9], and D. C. Galbraith et al. in 1987 [10] have all contributed to this. Common to their analyses is the rigorousness manifested as taking a coupled resonator system, writing out the expressions for input impedance/admittance, or transimpedance, etc., introducing some extra constraints/assumptions, and finally plotting the frequency responses to reveal the properties of coupled resonators. This method was carried on to the recent few decades when people looked at coupled resonators again when they were used as the link for wireless power or data transmission [11, 12, 13], with the difference that frequency responses could be plotted automatically and more precisely using much-advanced software.

Complementary to the existing analyses and theories, this work would like to go a different way. First, it will start from rigorous derivations based on the coupled resonators circuits but aim at organizing every step into low-entropy form [14] so that it can offer more insights and easily provide design advice. Accompanying this it will use equivalent circuits (sometimes with minor approximations) to intuitively show how coupled resonators work. (Theory I)

Second, it will follow the analysis of maximum power transfer and exploit the power of graphical methods. It will intuitively illustrate a few important properties of coupled

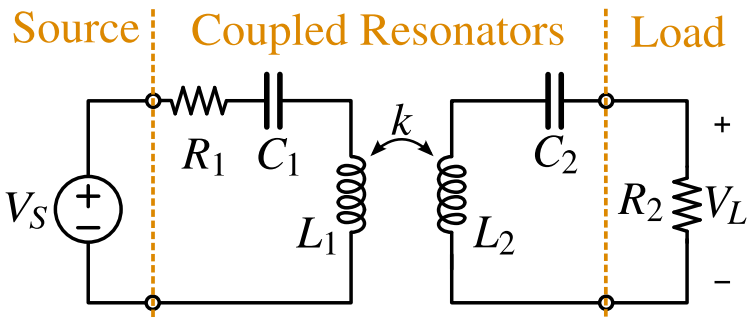

Figure 2.1: A general equivalent circuit for near-field wireless power or data system.

resonators using simple graphs. (Theory II)

Next, Theory I and Theory II will be linked together through the help of impedance loci analysis. It will be shown that though the two theories were developed using two completely different methods, but essentially they are the same thing. Theory II is no more than a special form of Theory I and, similarly, Theory I in most cases can be represented using graphical methods in Theory II for ease of understanding. Moreover, the impedance loci analysis will prove itself to be useful in deriving the new data modulation scheme, L-RSK (with greater details covered in Chapter 4).

Finally, the unified theory will be extended from series-LC coupled resonators to parallel-LC coupled resonators so that it covers all different forms existing in coupled resonators.

2.2 Theory I - Design-Oriented Analysis

In general, a near-field wireless power or data system is composed of a source driver and a load, linked together through coupled resonators (Fig. 2.1). For ease of analysis, let's start with series coupled resonators and it will be shown that parallel coupled resonators have similar properties. R_1 lumps the source resistance and the series resistance of L_1; similarly, R_2 lumps the load resistance and the series resistance of L_2. Also, suppose that when uncoupled (coupling coefficient $k = 0$), each side resonates at the same frequency:

$$\omega_0 = \frac{1}{\sqrt{L_1 C_1}} = \frac{1}{\sqrt{L_2 C_2}}. \tag{2.1}$$

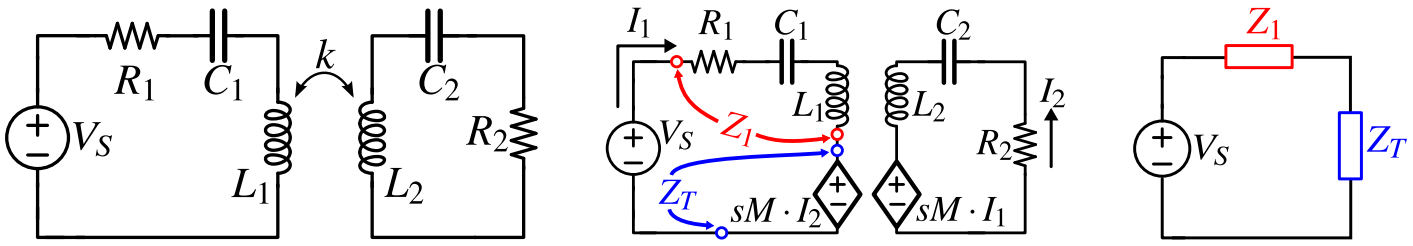

(a) (b) (c)

Figure 2.2: (a) The original circuit. (b) Replacing coupled inductors with z-parameter equivalent circuit. (c) Lump several components to form source Z_1 in series with transformed load Z_T.

Now, with nonzero coupling k, the coupled inductors in Fig. 2.1 (also shown in Fig. 2.2(a)) can be replaced by its z-parameter equivalent circuit involving controlled voltage sources (Fig. 2.2(b)). The input impedance seen at the port of the left controlled source is

$$Z_T(s) = \frac{-(sM)^2}{Z_2(s)}, \tag{2.2}$$

calculated by simply taking the ratio of the voltage across the controlled source over the current through it. Note that

$$Z_1(s) = R_1 + \frac{1}{sC_1} + sL_1, \tag{2.3}$$

$$\text{and } Z_2(s) = R_2 + \frac{1}{sC_2} + sL_2. \tag{2.4}$$

This is a fourth-order system, and to see its resonant frequencies, simply set:

$$Im\{Z_1(j\omega) + Z_T(j\omega)\} = 0. \tag{2.5}$$

Z_1 and Z_T can be replaced by expressions in (2.3) and (2.2) (also substitute s with $j\omega$), which gives the following equation:

$$(1 - \frac{1}{\omega^2 L_1 C_1}) = k^2 \frac{(\omega L_2)^2 (1 - \frac{1}{\omega^2 L_2 C_2})}{{R_2}^2 + (\omega L_2 - \frac{1}{\omega C_2})^2}. \tag{2.6}$$

Provided that (2.1), one solution for (2.6) would be $\omega = \omega_0$. In this case, both sides equal to zero, and this is the trivial solution.

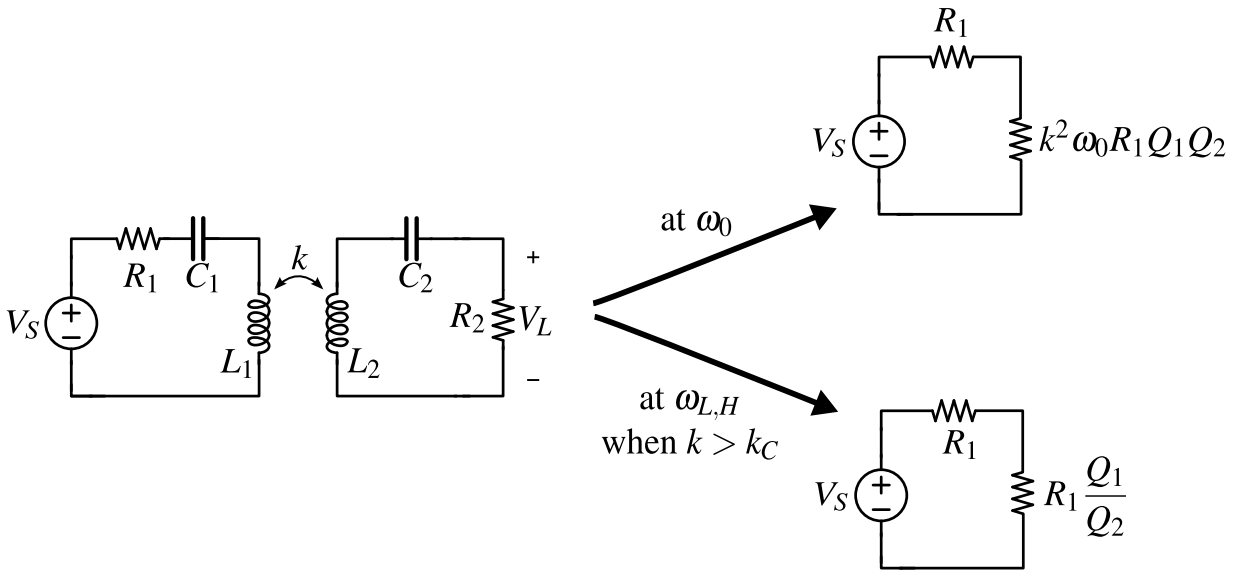

Figure 2.3: The input impedance at ω_0 or at $\omega_{L,H}$.

Non-trivial solutions can be calculated by cancelling the term to the left of the equality and the upper right term to the right of the equality, which gives

$$1 = k^2 \frac{(\omega L_2)^2}{{R_2}^2 + (\omega L_2 - \frac{1}{\omega C_2})^2}. \tag{2.7}$$

If assuming the quality factor of the secondary side, when uncoupled, $Q_2 \gg 1$, which is a valid assumption for any wireless power design to maintain a good efficiency, then (2.7), a quadratic equation of ω^2, only has solution provided

$$k \geq \sqrt{\frac{C_2}{L_2}} R_2 = \boxed{\frac{1}{Q_2} \triangleq k_C,} \tag{2.8}$$

defined as the critical coupling coefficienc. The non-trivial solutions are

$$\omega_L, \omega_H \approx \frac{\omega_0}{\sqrt{1 \pm k}}. \tag{2.9}$$

Since $0 < k < 1$, $\omega_L < \omega_0 < \omega_H$. Both $\omega_{L,H}$ split around the original ω_0, and with increasing k they split further apart.

Purely resistive as it is seen by the source V_S at all three resonant frequencies, however, one important observation is that the actual resistance values are quite different at ω_0 or $\omega_{L,H}$ Fig. 2.3. This can be calculated by taking the expressions for ω_0 (2.1) and $\omega_{L,H}$ (2.9),

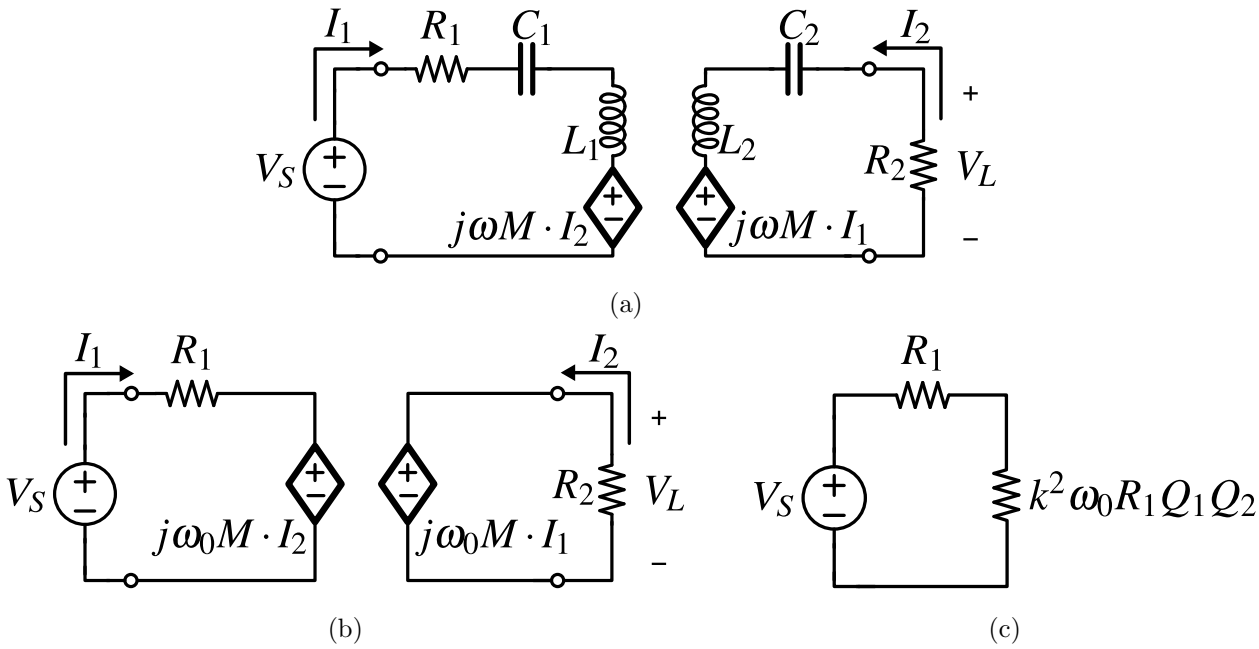

Figure 2.4: (a) One equivalent circuit to Fig. 2.1. (b) At ω_0, reactances of L_1 and C_1 cancel. So do reactances of L_2 and C_2. (c) The final equivalent circuit when driven at ω_0.

and plugging into the original circuit. However, a much more concise way to see this without overly complicating the derivation is through equivalent circutis.

For the given system, the coupled inductors can be modeled by many different equivalent circuits. Two are chosen to clearly show the relation in Fig. 2.3. One equivalent circuit is the one used previously, by replacing inductive coupling with controlled voltage sources as shown in Fig. 2.4(a), in effect the z-parameter representation of the coupled pair of inductors. At ω_0, L_1 resonates with C_1; L_2 resonates with C_2. Now the circuit is composed of resistors only, coupled with controlled voltage sources that are dependent on k (Fig. 2.4(b)). Therefore, at the frequency ω_0, the source is terminated by a pure resistance that depends on the coupling k (Fig. 2.4(c)). Q_1 and Q_2 are the quality factors for uncoupled LC resonators:

$$Q_1 = \frac{1}{R_1}\sqrt{\frac{L_1}{C_1}}, \text{ and } Q_2 = \frac{1}{R_2}\sqrt{\frac{L_2}{C_2}}. \tag{2.10}$$

The input impedance at $\omega_{L,H}$ is readily seen through a different equivalent circuit of coupled inductors [15, Ch. XVII, Sec. 5] than in Fig. 2.4 (a). It now comprises an ideal transformer of fixed turns ratio together with self- and leakage inductors that depend on k

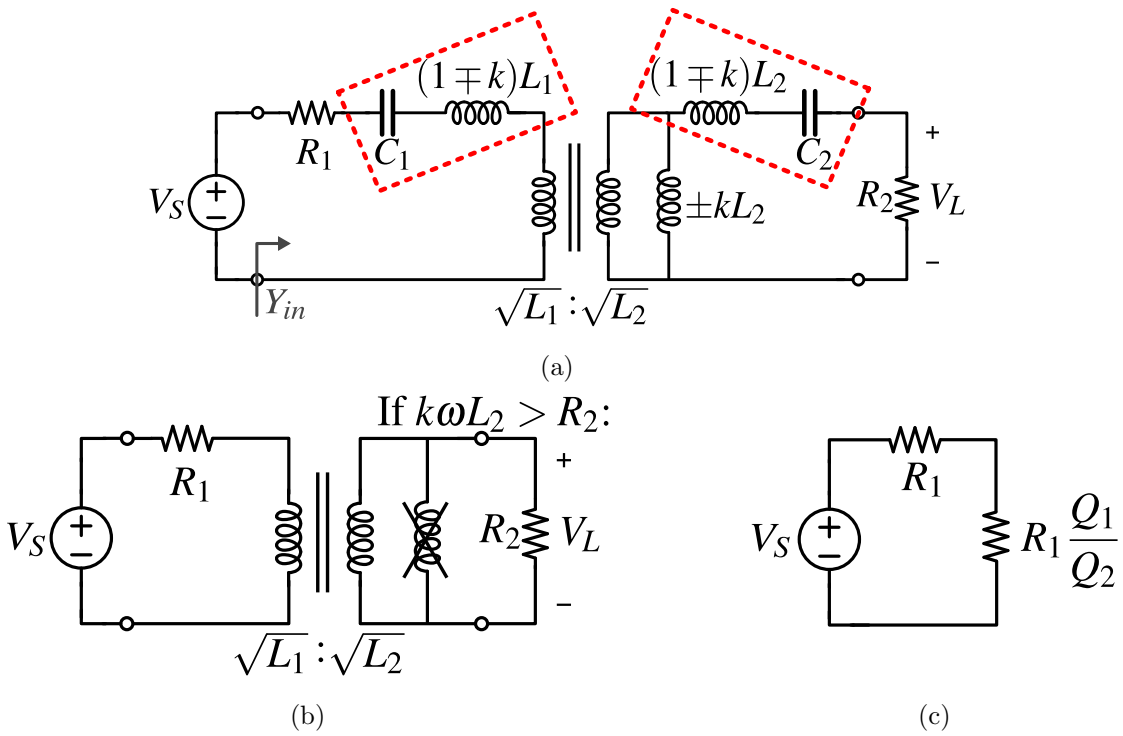

Figure 2.5: (a) A different equivalent circuit to Fig. 2.1. (b) Reactances on both sides can cancel at two frequencies: ω_L or ω_H. (c) When $k > k_C$, the system is purely resistive at $\omega_{L,H}$, and load appears as a fixed value, independent of k.

(Fig. 2.5(a)). For this system, both LC tanks enclosed in the red dashed boxes resonate at $\omega_{L,H}$ given in (2.9) When driven at ω_L or ω_H, the circuit simplifies to Fig. 2.5(b). Now, if the reactance $k\omega L_2$ is larger than R_2, then this becomes approximately a resistor-only two-port coupled with a transformer of fixed turns ratio. The load is independent of the coupling coefficient k (Fig. 2.5(c)). Ignoring the shunt inductor requires that

$$k\omega_0 L_2 > R_2 \quad \Rightarrow \quad k > \frac{R_2}{\omega_0 L_2} = \frac{1}{Q_2} = k_C, \tag{2.11}$$

which is the same condition as what was derived at (2.8). The typical range for k in applications related to this work is 0.05∼0.3. Other similar applications should have roughly the same range.

Note that in Fig. 2.5(b), the susceptance $\mp j/(\omega_{L,H} k L_2)$ was neglected when the coupling is strong enough. But including this non-zero susceptance, the input admittance Y_{in} will be

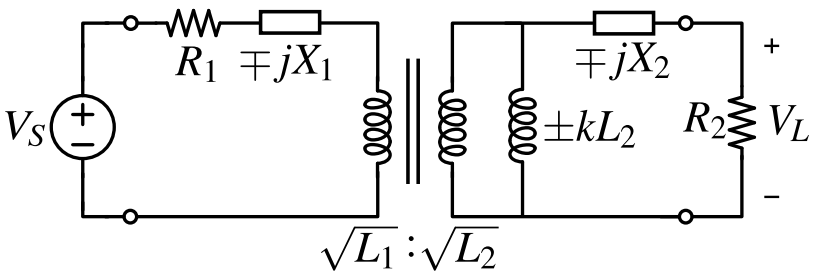

Figure 2.6: Equivalent circuit to Fig. 2.5 (a) at frequency that slightly deviates from $\omega_{1,2}$. All reactances can now cancel exactly (without approximation) and the system becomes purely resistive.

zero phase not exactly at $\omega_{L,H}$ but at small frequency offset such that the reactances in the dashed boxes of Fig. 2.5(a) do not cancel exactly, but leave some remainder reactances of the right signs shown in Fig. 2.6. Now these remaining reactances will cancel the reactance of $\pm kL_2$ at the slightly offset frequencies which will still be denoted as $\omega_{L,H}$ to avoid notational clutter.

2.3 Theory II - Graphical Methods

Having derived everything rigorously by solving equations, it is of interest to analyze the system from a different perspective. In Fig. 2.2(c), it was shown that the system can be simplified to Z_1 in series with Z_T.

Now, if Z_1 is treated as the source impedance, and Z_T as the load impedance which lumps the influence of coupling and loading on the secondary side (Fig. 2.7), it is of interest to learn about the system's available power. This is not only because in some cases it is desired to extract all the available power from the source and achieve maximum power transfer, but also, a system's available power is a function of its source and source impedance only, independent of the load and in this case, independent of the coupling.

In addition to the initial assumption (2.1), also assume that the quality factors Q_1 and

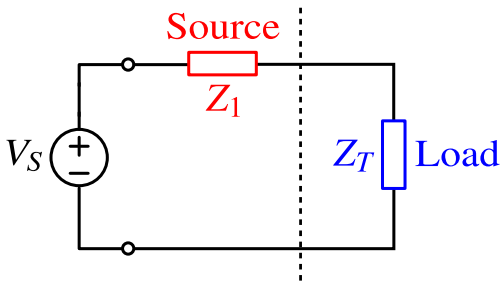

Figure 2.7: V_S driving source Z_1 and load Z_T.

Q_2 as given in (2.10) are equal and very large.

$$Q_1 = Q_2, \tag{2.12}$$

$$\text{and } Q_1, Q_2 \gg 1. \tag{2.13}$$

Note that (2.12) is a special-case assumption that is not the case for many practical applications, and will be removed in the next section when the conclusion is generalized. To extract the available power from the source, Z_T and Z_1 need to form a conjugate pair:

$$Z_1(j\omega) = Z_T(j\omega)^* \quad \Rightarrow \quad Z_1(j\omega) = \left[\frac{k^2\omega^2 L_1 L_2}{Z_2(j\omega)}\right]^*, \tag{2.14}$$

which, by definition of conjugacy, indicates Z_1 and Z_T equal in magnitude and opposite in phase:

$$\left|Z_1(j\omega)\right| = \left|\frac{-(j\omega)^2 k^2 L_1 L_2}{Z_2(j\omega)}\right| \quad \Rightarrow \quad \left|\frac{Z_1(j\omega)}{j\omega L_1}\right| = k^2 \left|\frac{j\omega L_2}{Z_2(j\omega)}\right|; \tag{2.15}$$

$$\angle Z_1(j\omega) = -\angle\left[\frac{-(j\omega)^2 k^2 L_1 L_2}{Z_2(j\omega)}\right] \quad \Rightarrow \quad \angle Z_1(j\omega) = \angle Z_2(j\omega). \tag{2.16}$$

Since both $Z_1(j\omega)$ and $Z_2(j\omega)$ are second-order systems, (2.15) and (2.16) can be visualized as shown in Fig. 2.8 (a) and (b). Normally, it's hard to satisfy both conditions simultaneously.

With the assumptions of (2.1), (2.12) and (2.13), the phase curves of Z_1 and Z_2 in Fig. 2.8 (b) will coincide each other, and solutions exist at the frequency where curves in Fig. 2.8 (a) intersect. Depending on the strength of the coupling k, there are three different scenarios as listed in Fig. 2.9.

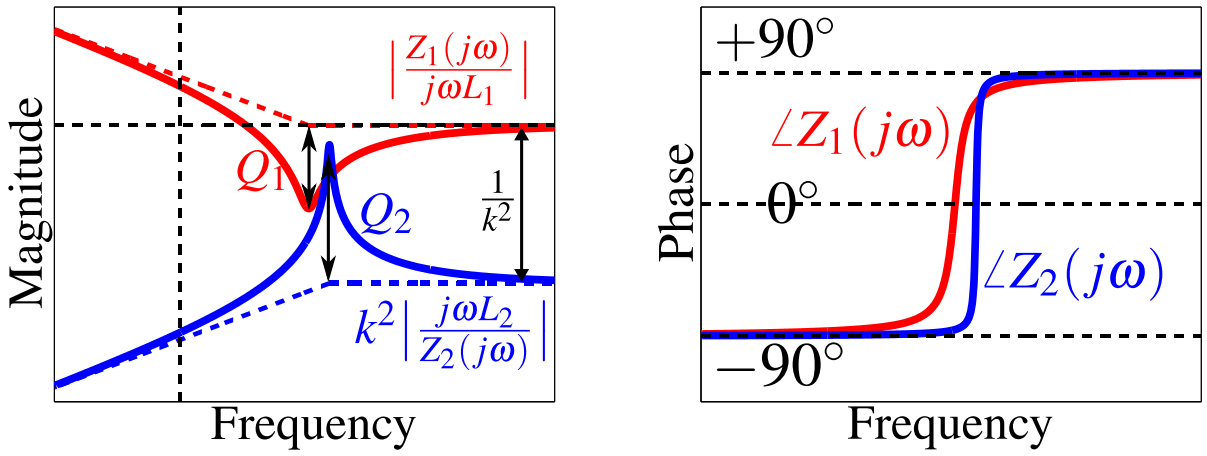

(a) (b)

Figure 2.8: (a) The magnitude plot visualizing (2.15). (b) The phase plot visualizing (2.16).

Apparent from the figures, $k_C = 1/Q_2$, which matches the previous derivation of the critical coupling (2.8). It can also be verified that the approximate expression (2.9) for split frequencies $\omega_{L,H}$ matches with what's shown in the figures.

For $k \geq k_C$, at any intersection frequency (ω_0 for $k = k_C$ and $\omega_{L,H}$ for $k > k_C$), maximum power is transfered from source to load with 50% efficiency. The equivalent circuit changes from Fig. 2.10 (a) to Fig. 2.10 (b).

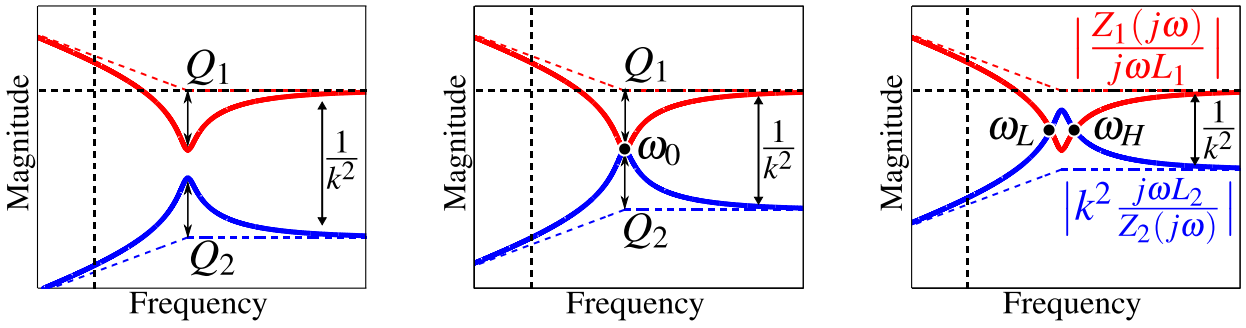

(a) (b) (c)

Figure 2.9: Graphical illustrations of equations (2.15) and (2.16) under the assumptions of equal ω_0 and equal Q: (a) under-coupled, (b) critical-coupling, and (c) over-coupled.

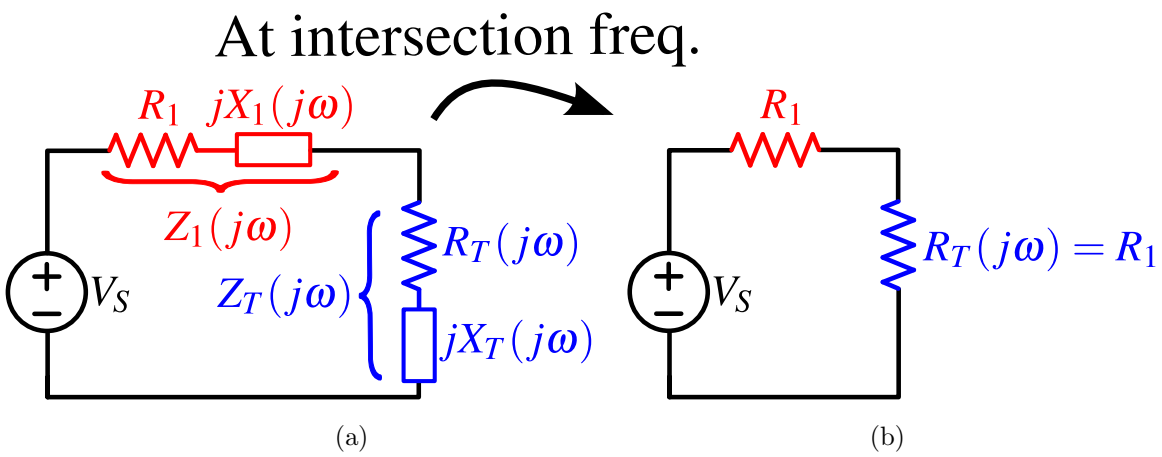

Figure 2.10: At the intersection frequency(ies) shown in Fig. 2.9, the original circuit composed of Z_1 and Z_T is simplified to be purely resistive.

Despite the fact that detailed physics expressions in the previous section can explain what's exactly going on in a system, graphical methods can provide a more intuitive understanding by omitting tedious details and only preserving the important aspects, which can be helpful in guiding designs. For example, by looking at Fig. 2.9 , several questions can be answered:

1. The reason why having equal resonance (ω_0) for both standalone LC-tanks, often referred to as "resonant wireless power system" (Fig. 2.11(a)) as opposed to "inductive

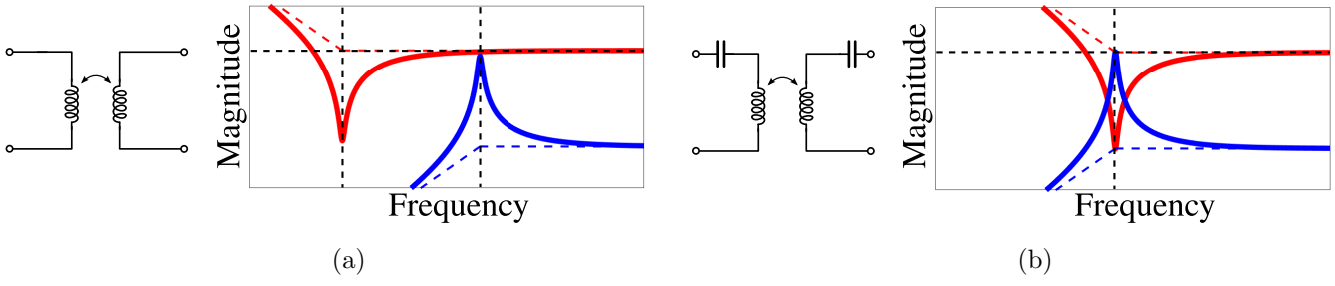

Figure 2.11: (a) Sometimes referred to as "Inductive wireless power". (b) Sometimes referred to as "resonant wireless power" in which the two sides, when uncoupled, resonate at the same frequency.

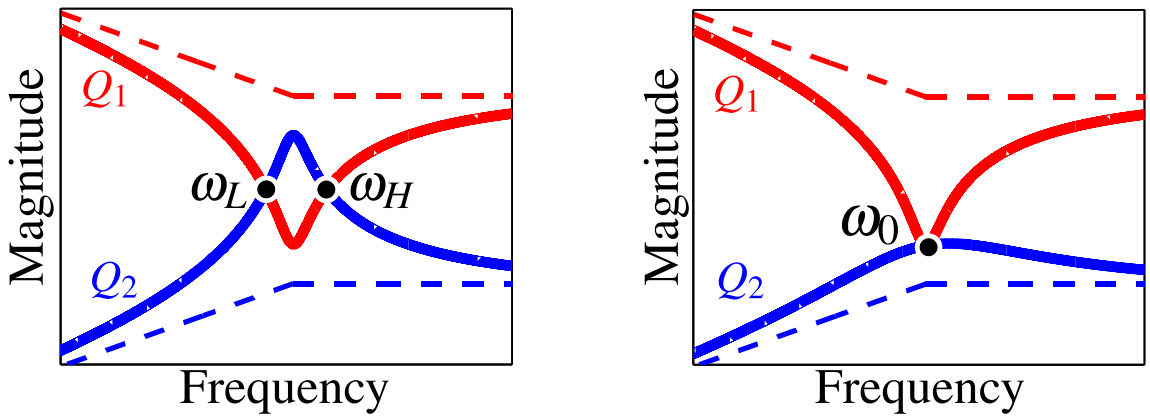

Figure 2.12: Two ways to ensure a stable power delivery in a dynamic environment where coupling changes frequently: (a) Tune the operating frequency to $\omega_{L,H}$. (b) Fix the frequency at ω_0 and adjust the quality factor insteady.

wireless power system" (Fig. 2.11(b)) is because by aligning the "peaks" of both Q-curves it's possible for them to intersect at the minimum coupling k.

2. Similarly, the reason why high quality factors are desired is also because they ensure the two curves can still intersect at a minimum coupling k compared with systems of lowered Q_1 and Q_2.

3. In general, there are two types of strategy to make the load extract maximum power, or, as will be shown later, to make the load receives constant power under change in coupling k. As illustrated in Fig. 2.12, for $k > k_C$, the power driver's operating frequency can be tuned to be one of the $\omega_{L,H}$; alternatively, the driving frequency can be fixed at ω_0 and the quality factor of either tank can be dynamically adjusted (preferably in a lossless way) to ensure the curves intersect at ω_0.

2.4 Link Theory I and Theory II Together

One of the assumptions for the graphical analysis in the previous section is equal quality factors Q_1 and Q_2 for both LC tanks (2.12). In practice, this assumption is often not

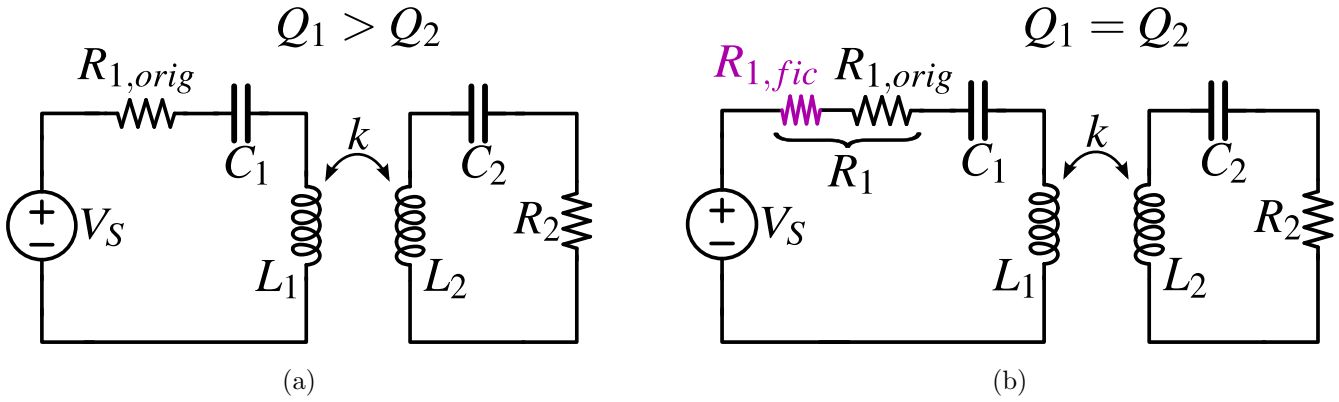

Figure 2.13: (a) Equivalent circuit for a general-case coupled resonators where Q_1 and Q_2 don't have to be equal. (b) A fictitious resistance can be introduced to equalize the quality factors of both sides.

satisfied. Moreover, in a lot of applications the goal of wireless power design is to deliver stable power under variations in coupling, etc. at a highest possible efficiency, rather than to achieve max. power transfer which only happens at 50% efficiency.

It turns out that Theory-II can be easily generalized to cover those cases, and thus can be linked to Theory-I. Consider the equivalent wireless power system of a general case in Fig. 2.13 (a). Here, the resonance frequencies of both standalone LC tanks are equal ω_0. It is also assumed that the quality factors are large (2.13). But they no longer necessarily

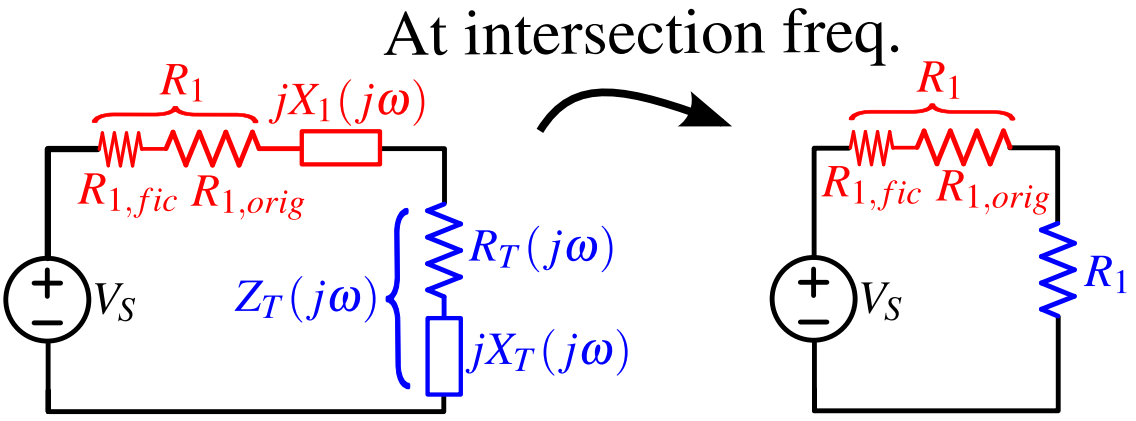

Figure 2.14: With or without the fictitious resistance, the system's intersection frequency(ies) remains unchanged.

equal one another.

Without loss of generality, let's also assume that $Q_1 > Q_2$. Then for the given system, imagine that fictitiously an appropriate $R_{1,fic}$ is added to reduce Q_1 and make it equal to Q_2 (Fig. 2.13 (b)). The system now becomes the same as that in Fig. 2.10 (a), with R_1 now equal to the summation of the original $R_{1,orig}$ and the fictitiously added $R_{1,fic}$. Exactly the same conclusions can be drawn, and therefore, at any intersection frequency $\omega_{L,H}$, the equivalent circuit now becomes Fig. 2.14.

One important observation is: neither $X_1(j\omega)$ nor $Z_T(j\omega)$ is related to R_1 in any form. This means that even if the fictitiously added $R_{1,fic}$ is taken away, the system still has an equivalent circuit shown in Fig. 2.14, but with $R_{1,fic}$ removed.

The intersection frequency remains the same as the system with fictitiously added $R_{1,fic}$. Graphically (Fig. 2.15), this means that for systems with $Q_1 \neq Q_2$, "fictitiously", Q_1 can be changed to be equal to Q_2 for the purpose of locating the values of ω_L and ω_H. After that it can be concluded that, for $k > k_C$, if operating at $\omega_{L,H}$, the source sees a purely-resistive

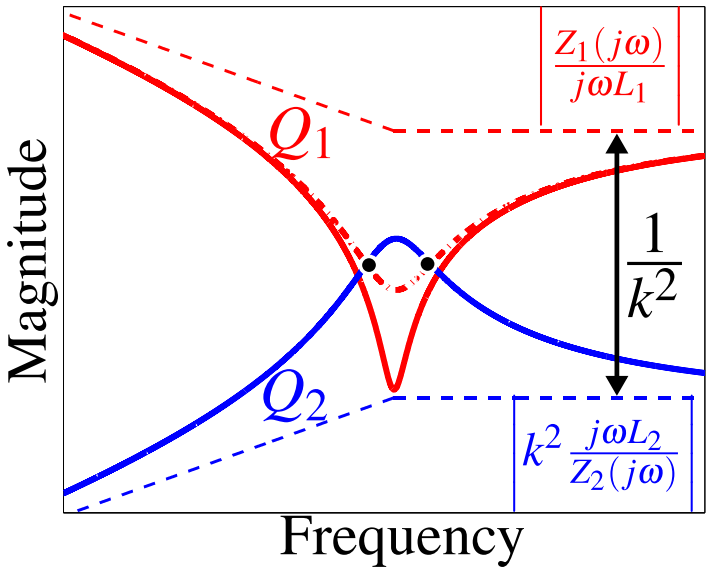

Figure 2.15: For systems with unequal Q, the split frequencies could be found by setting $Q_1 = Q_2$ and observing the intersection frequency(ies).

load that is a constant value, regardless of change in k. The power transfer efficiency is no longer 50% as in the max. power transfer case, it becomes

$$\eta = \frac{R_1}{R_1 + R_{1,orig}} = \frac{Q_1}{Q_1 + Q_2}, \tag{2.17}$$

where $R_1 = R_{1,orig} + R_{1,fic}$.

Another way to understand this is through the help of impedance loci with varying ω. The total input impedance $Z_{in}(j\omega)$, which is the summation of $Z_1(j\omega)$ and $Z_T(j\omega)$, can be plotted on the complex plane as a locus of varying ω (Fig. 2.16).

When the system is weakly coupled ($k \leq k_C$) corresponding to Fig. 2.9 (a) and (b), as shown in Fig. 2.16 (a), with increasing ω, the $Z_{in}(j\omega)$ trace moves upwards as indicated by the arrows on the dashed curve, and intersects the real-axis when $\omega = \omega_0$. Note that the trace of $Z_1(j\omega)$ moves along a vertical line orthogonal to the real axis. This is because $Re\{Z_1(j\omega)\} = R_1$ is a constant value independent of ω. Moreover, at $k = k_C$, the real part of source Z_1 and Z_T are equal at ω_0, where maximum power is transferred at 50% efficiency.

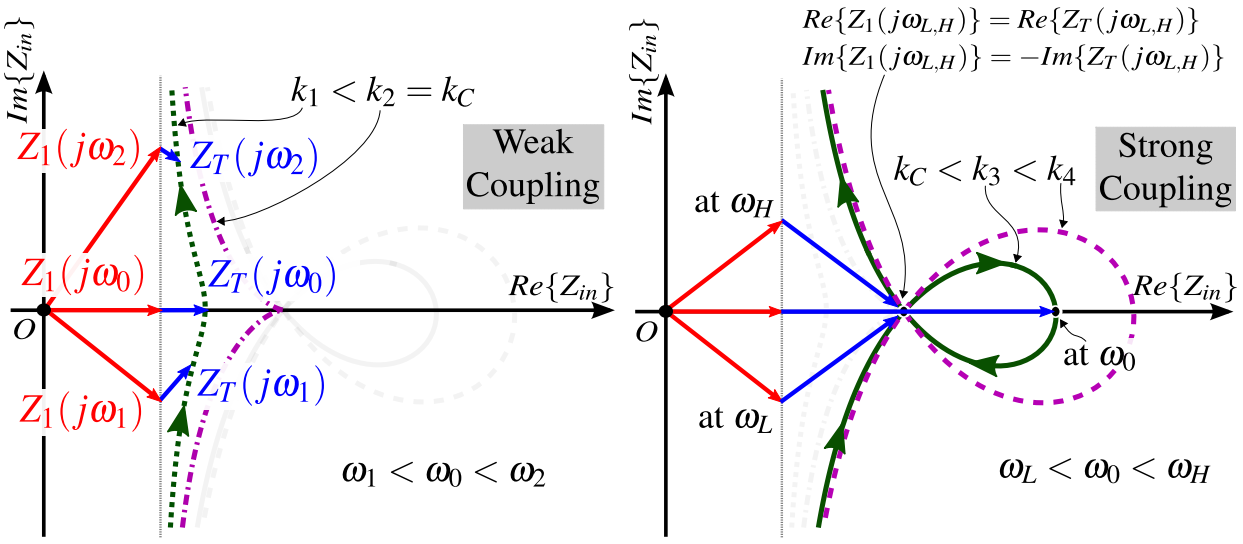

Figure 2.16: (a) For weak coupling ($k \leq k_C$), the loci of input impedance intersect the real axis only once at ω_0. (b) For strong coupling ($k > k_C$), the loci of input impedance intersect the real axis at $\omega_{L,H}$ in addition to ω_0.

When the coupling gets stronger ($k > k_C$) corresponding to Fig. 2.9 (c), Fig. 2.16 (b) shows that the impedance locus intersects the real-axis three times, at ω_L, ω_0, and ω_H. At ω_L or ω_H, $Re\{Z_1(j\omega)\} = Re\{Z_T(j\omega)\}$ so that maximum power transfer happens. As k changes, the values of ω_L and ω_H also change. But $Z_{in}(j\omega)$'s locus always intersects the real-axis at the same spot at $\omega = \omega_{L,H}$. However, apparently from the figure, the intersection with real-axis at ω_0 varies with k. These correspond to the previously derived conclusions shown in Fig. 2.3.

Now, without loss of generality, consider changing R_1 to a smaller R_1' (from Fig. 2.17(a) to Fig. 2.17(b)). Neither $Z_T(j\omega)$ or $Z_1(j\omega)$'s imaginary part is related to R_1. Only Z_1's real part shrinks. Therefore, it's as if the impedance loci are horizontally shifted to the left by the amount $(R_1 - R_1')$, with the rest of quantities remain unaffected at all.

As a result, for series-LC coupled resonators, provided (2.1) holds, for $k \geq k_C$, as long as the system operates at one of $\omega_L(k)$ or $\omega_H(k)$, both are functions of k, the source sees a purely resistive and constant load, and stable power is delivered regardless of coupling variations.

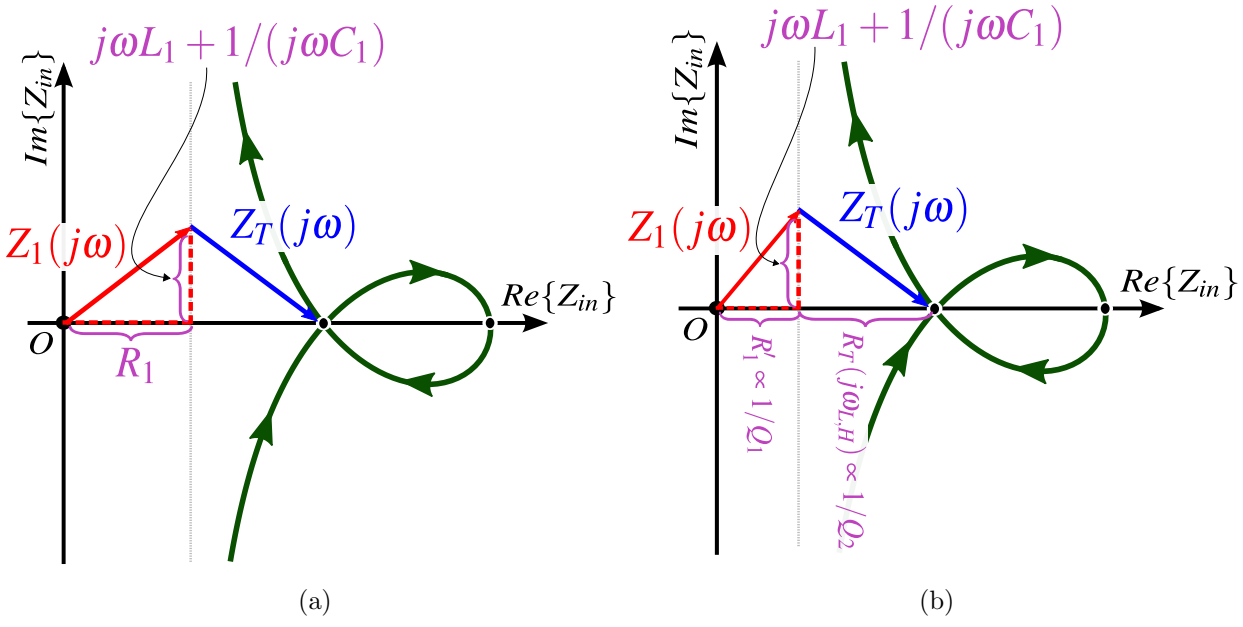

Figure 2.17: (a) Impedance loci when $Q_1 = Q_2$. (b) General case when $Q_1 \neq Q_2$. The curve is shifted horizontally with everything else staying unchanged.

The system's power transfer efficiency is $\eta = Q_1/(Q_1+Q_2)$. The maximum power transfer is a special case of the aforementioned generalized stable power delivery scenario with $Q_1 = Q_2$, which gives exactly 50% efficiency.

2.5 Extend to Parallel-LC Coupled Resonators

Practical wireless power systems may desire parallel-connected LC coupled resonators. As what's shown next, despite the fact that the equivalent circuit of coupled inductors is in nature a z-parameter circuit which is incompatible with the parallel-connected LC, parallel LC coupled resonators are still approximately the dual case of series LC resonators. Most of the derivations below can also be found at [16].

After replacing coupled inductors with the equivalent circuit using controlled voltage sources (Fig. 2.18), it can be shown that the input admittance can be approximately rep-

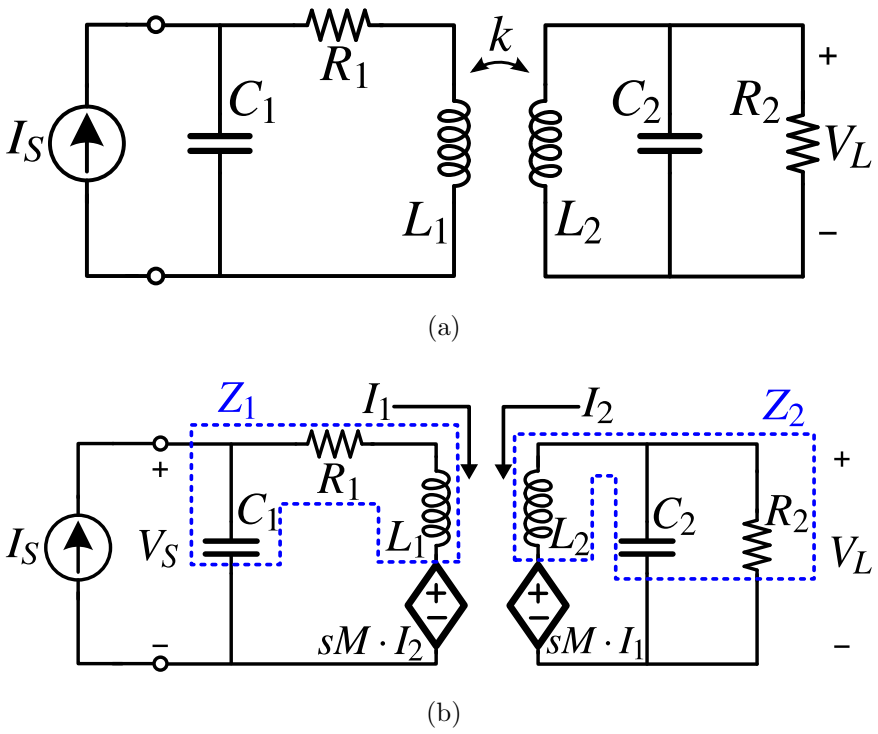

Figure 2.18: (a) The equivalent circuit for parallel-LC coupled resonators. (b) Replacing the coupled inductors with its z-parameter equivalent circuit.

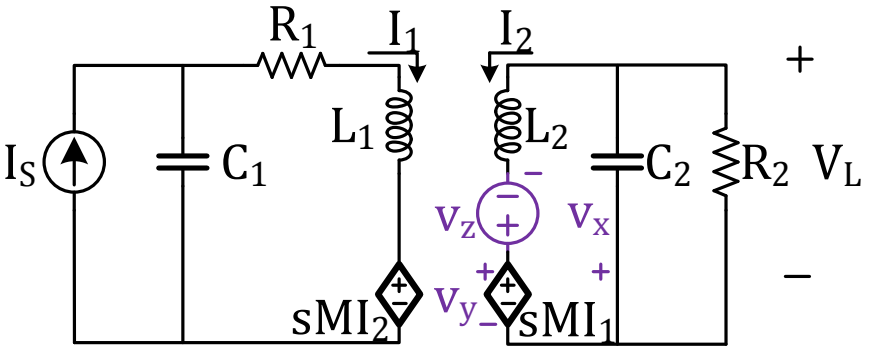

Figure 2.19: v_z can be injected to facilitate feedback analysis.

resented as the parallel combination of a source admittance Y_1 and a transformed load admittance Y_T.

There are many ways to arrive at this result. Among them, feedback analysis [17] is used in this work for its low-entropy forms. With the circuit structure undisrupted, a voltage source v_z can be injected in series with the controlled source on the right side (Fig. 2.19). Then, following the principles of null-double injection [18], it could be calculated that:

$$H = \frac{V_L(s)}{I_S(s)} = H^{u_y} \frac{1 + \frac{1}{T_n}}{1 + \frac{1}{T}}, \tag{2.18}$$

with

$$H^{u_y} = \left.\frac{V_L(s)}{I_S(s)}\right|_{v_y=0} = \frac{-I_2(R_2 \| \frac{1}{sC_2})}{(sM)(sC_1) \cdot I_2} = -\frac{R_2 \| \frac{1}{sC_2}}{(sM)(sC_1)}, \tag{2.19}$$

$$T_n = \left.\frac{v_y(s)}{v_x(s)}\right|_{V_L=0} = \frac{sM \cdot I_1}{0} = \infty, \tag{2.20}$$

$$\text{and } T = \left.\frac{v_y(s)}{v_x(s)}\right|_{I_S=0} = \frac{sM \cdot I_1}{-\frac{I_1 \cdot Z_1}{sM} \cdot Z_2} = \frac{-(sM)^2}{Z_1 \cdot Z_2}. \tag{2.21}$$

where $Z_1(s) = 1/sC_1 + R_1 + sL_1$ and $Z_2(s) = 1/(sC_2 + G_2) + sL_2$ are the series impedance as shown in the dashed boxes in Fig. 2.18(b).

T is the loop gain of this feedback system. Now that the loop gain has been calculated, the next step would be to figure out an equivalent circuit that looks like the parallel dual of Fig. 2.7.

The input admittance to the feedback system is:

$$Y_{in}(s) = (Y_{in}|_{T=0}) \cdot \frac{(1+T)}{(1+T')}, \tag{2.22}$$

with

$$Y_{in}(s)|_{T=0} = sC_1 + \frac{1}{sL_1 + R_1}, \tag{2.23}$$

$$T(s) = -\frac{(sM)^2}{Z_1 Z_2}, \tag{2.24}$$

$$\text{and } T'(s) = -\frac{(sM)^2}{(sL_1 + R_1)Z_2}. \tag{2.25}$$

Therefore, input admittance is a parallel combination of source $Y_1 = Y_{in}|_{T=0}$ and transformed admittance $Y_T = Y_{in}|_{T=0} \cdot T$, both scaled by a correction factor $1/(1+T')$:

$$Y_{in}(s) = (Y_1 + Y_T) \cdot \frac{1}{1+T'} \tag{2.26}$$

For ease of analysis, it could be temporarily assumed that the influence of T' is ignorable, i.e. $1+T' \approx 1$, and evaluate the actual influence of T' later. Now, provided that the quality factors of the LC tanks on both sides, when uncoupled ($k = 0$), $Q_1, Q_2 \gg 1$, Z_2 can be rewritten as $Z_2 = \frac{1}{sC_2} + R_2' + sL_2$, with $R_2' = \frac{1}{(\omega C_2)^2 R_2}$; the new resonance frequency for

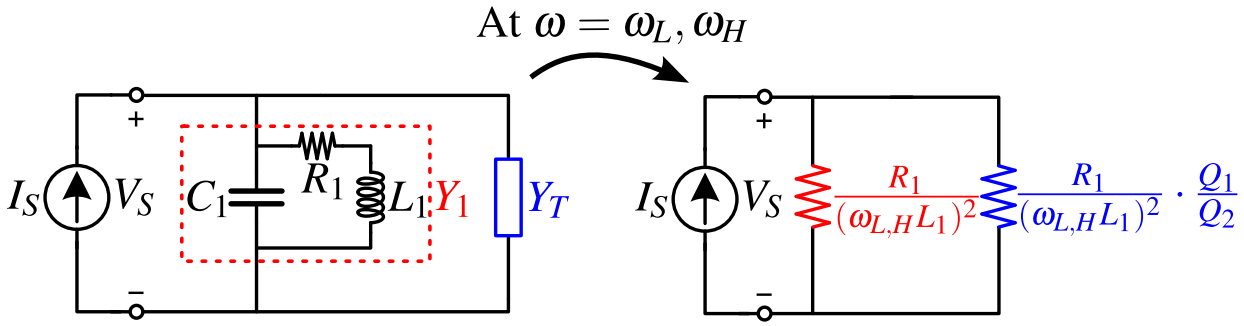

Figure 2.20: The input admittance of parallel-LC coupled resonators (when assuming correction factor $1/(1+T') = 0$) at $\omega_{L,H}$ becomes purely conductive, but not constant for different coupling k.

non-zero k can be calculated by:

$$Im\{Y_1(j\omega) + Y_T(j\omega)\} = 0 \tag{2.27}$$

$$\Rightarrow (1 - \frac{1}{\omega^2 L_1 C_1}) = k^2 \frac{(\omega L_2)^2 (1 - \frac{1}{\omega^2 L_2 C_2})}{R_2'^2 + (\omega L_2 - \frac{1}{\omega C_2})^2}. \tag{2.28}$$

(2.28) resembles the form of (2.6), and thus has a trivial solution at ω_0, and non-trivial solutions at $\omega_{L,H}$ given by (2.9) if the coupling satisfies $k > k_C$. The input admittance at $\omega_{L,H}$ can be shown to be two purely-conductive terms that are dependent on $\omega_{L,H}$, both are functions of k (Fig. 2.20).

Now going back to evaluate the influence of the correction factor $1/(1 + T')$, rather than look at the entire frequency spectrum, it may be of particular interest to focus on the frequencies of interest, ω_L and ω_H. Under the assumption of $Q_1, Q_2 \gg 1$,

$$T'(j\omega) = \frac{\omega^2 k^2 L_1 L_2}{(j\omega L_1 + R_1)(Z_2)} \tag{2.29}$$

$$\approx \frac{\omega^2 k^2 L_1 L_2}{-\omega^2 L_1 L_2 + j\omega R_1 L_2 + \frac{j\omega L_1 + \cancel{R_1}}{j\omega C_2 + \cancel{G_2}}} \tag{2.30}$$

$$= \frac{k^2}{(\frac{\omega_0^2}{\omega^2} - 1) + j\frac{1}{Q_1}}. \tag{2.31}$$

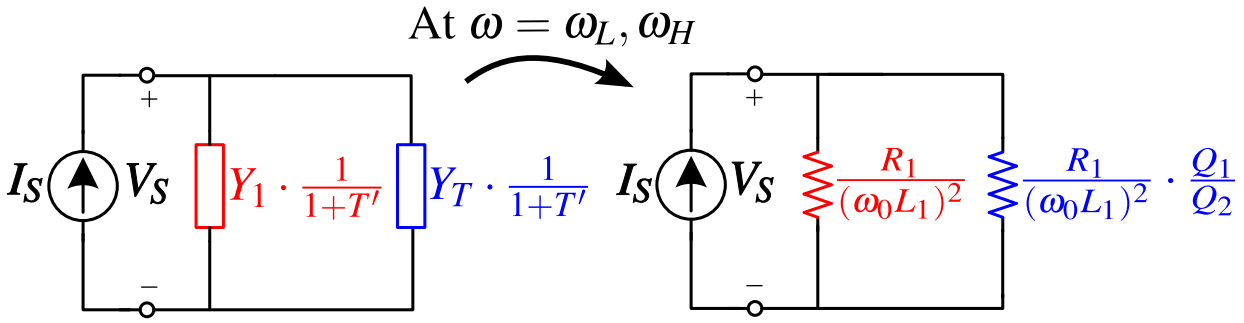

Figure 2.21: When taking into account of the correction factor $1/(1 + T')$, the input admittance at $\omega_{L,H}$ becomes constant conductance for different coupling $k > k_C$.

At the frequencies of interest, $\omega_L, \omega_H \approx \frac{\omega_0}{\sqrt{1\pm k}}$,

$$T'(j\omega_{L,H}) = \frac{k^2}{(\pm k) + \frac{j}{Q_1}} \tag{2.32}$$

$$\Rightarrow \frac{1}{1+T'(j\omega_{L,H})} = \begin{cases} \frac{1}{1\pm k} = \frac{\omega_{L,H}^2}{\omega_0^2} & \text{, if } k > \frac{1}{Q_1}; \\ \frac{1}{1+Q_1k^2/j} \approx 1 & \text{, if } k < \frac{1}{Q_1}. \end{cases} \tag{2.33}$$

With (2.33), two conclusions come to light: (1) It was previously assumed that T' has no influence on the system's new resonance frequency (when $k > 0$). This assumption is valid, because T' is purely real and thus has negligible influence on when the imaginary part of $(Y_1 + Y_T)/(1 + T')$ becomes zero. (2) Figure 2.20 shows that at $\omega_{L,H}$, the input conductance are dependent on the values of $\omega_{L,H}$, which varies with k. However, it turns out that the correction factor $1/(1 + T')$ "fixes" such problem by

$$Y_{in}\Big|_{\omega_{L,H}} = \frac{1}{1 \pm k}\Big[Y_1 + Y_T\Big]_{\omega_{L,H}} = \frac{\cancel{\omega_{L,H}^2}}{\omega_0^2}\frac{R_1}{\cancel{\omega_{L,H}^2}L_1^2}(1 + \frac{Q_1}{Q_2}), \tag{2.34}$$

for as long as $k > 1/Q_1$, which presumably covers the entire range of $k > k_C = 1/Q_2$ because as will be shown later, good system designs should have $Q_1 > Q_2$. Even if this is not the

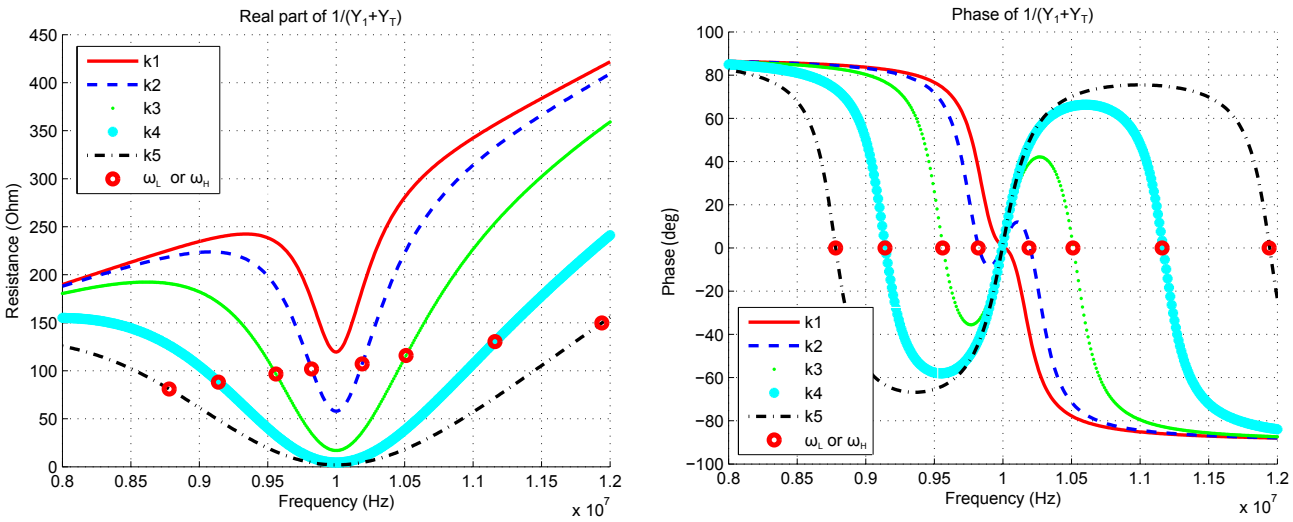

Figure 2.22: For better illustration, the inverse of $(Y_1 + Y_T)$, is plotted. Left part plots the real part of it; clearly its magnitude is not constant at $\omega_{L,H}$ for different k. and right part plots the phase of it. Also, $k_1 < k_2 < k_3 < k_4 < k_5$.

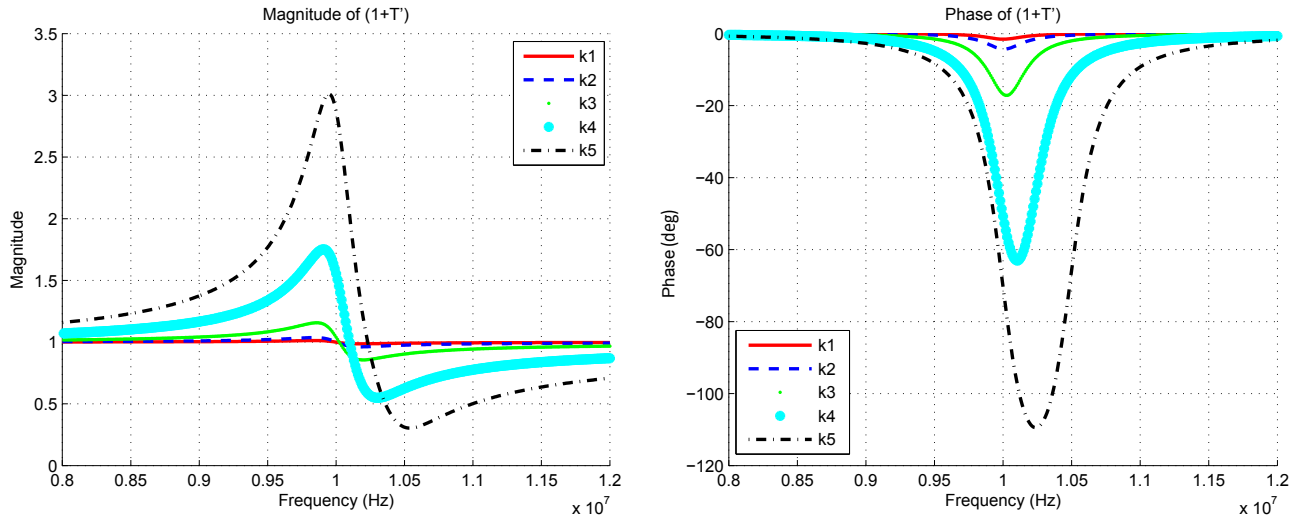

Figure 2.23: The magnitude and phase of the inverse of the correction factor, $(1+T')$, is plotted. Although it seems that at some frequency, $(1+T')$'s influence might be significant, however, as shown by (2.33), its influence at the frequencies of interest, $\omega_{L,H}$, is negligible and sometimes even beneficial. $k_1 < k_2 < k_3 < k_4 < k_5$.

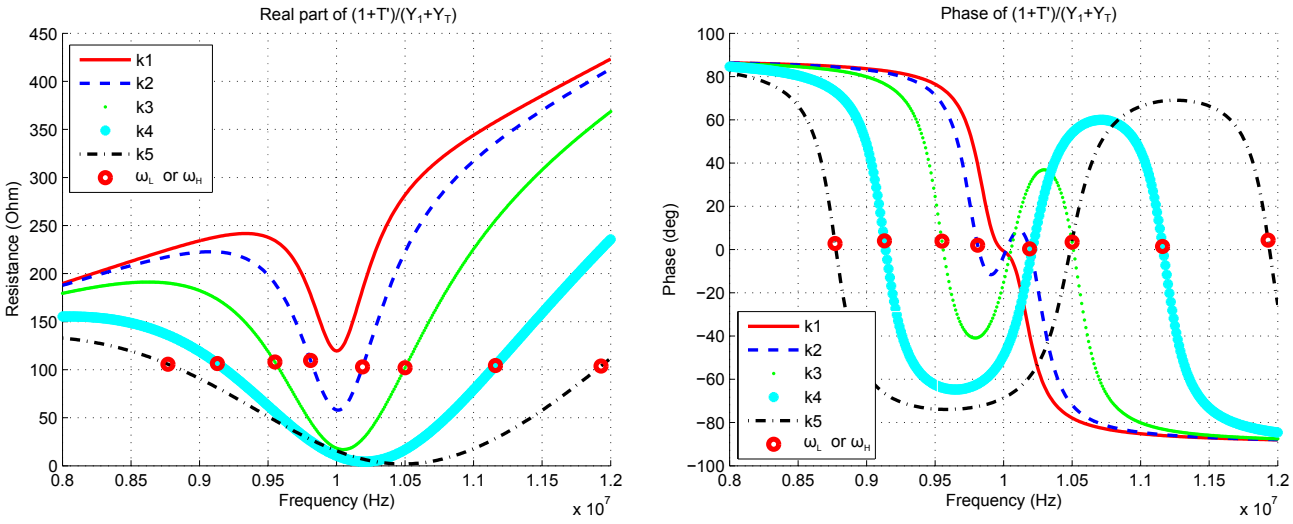

Figure 2.24: With the correction factor, the input admittance's phase at split frequencies $\omega_{L,H}$ remain unaffected. However, the magnitude at $\omega_{L,H}$ is fixed to be constant over different k. $k_1 < k_2 < k_3 < k_4 < k_5$.

case, for $k < 1/Q_1$, the difference between ω_L and ω_H already becomes negligible as indicated by (2.9). As a result, the source sees a constant conductance at $\omega_{L,H}$ (Fig. 2.21).

Fig. 2.22, Fig. 2.23, and Fig. 2.24 show how the correction factor $1/(1+T')$ "fixes" the non-constant input conductance at $\omega_{L,H}$. Originally, it is clear that $|(Y_1+Y_T)|$ at $\omega_{L,H}$ is not constant. With the correction factor $1/(1+T')$, it fixes the magnitude of (Y_1+Y_T) at $\omega_{L,H}$ to be constant while almost not disturbing the phase at all.

The equivalent circuit in Fig. 2.21 is derived from the perspective of input admittance. It is of great interest to map the power dissipation in the two components, $Y_1/(1+T')$ and $Y_T/(1+T')$, to the actual power dissipation in the primary (source) side and secondary (load) side.

From Fig. 2.21, it's apparent that power dissipated in $Y_S/(1+T')$ at $\omega_{L,H}$ is

$$P_{Y_S} = \frac{\left|V_S\right|^2}{2\omega_0^2 {L_1}^2/R_1}. \tag{2.35}$$

And from Fig. 2.18 (b), power dissipated in R_1 is

$$P_{R_1} = \frac{1}{2}\left|I_1\right|^2 R_1. \tag{2.36}$$

V_S for both circuits refers to the same thing, and the relation between V_S and I_1 can be revealed by applying KVL to the circuit in Fig. 2.18 (b)

$$V_S = (sL_1+R_1)\cdot I_1 - \frac{(sM)^2}{Z_2}\cdot I_1. \tag{2.37}$$

It could be seen that the power into Y_S does not equal the power into R_1:

$$\frac{P_{Y_S}}{P_{R_1}} = \frac{\left|V_S\right|^2}{\left|I_1\right|^2\cdot\left|sL_1\right|^2}\cdot\left(\frac{\omega}{\omega_0}\right)^2 \tag{2.38}$$

$$= \left|1-\frac{(sM)^2}{(sL_1+R_1)(Z_2)}\right|^2\left|\frac{1}{1+T'}\right| = \left|1+T'\right|. \tag{2.39}$$

They differ by the same correction factor $\left|1+T'\right|$.

Taking into account this correction factor, it could be derived that the power dissipated in R_1 is:

$$P_{R_1} = P_{Y_S}|1+T'| = \frac{1}{2}\left|V_S\right|^2\frac{R_1}{\omega_0^2 L_1^2}\cdot\frac{1}{1\pm k}. \tag{2.40}$$

Provided that the total power:

$$P_{total} = P_{Y_S} + P_{Y_T} = \frac{1}{2}\left|V_S\right|^2 \frac{R_1}{\omega_0^2 L_1^2} \cdot \frac{Q_1 + Q_2}{Q_2} \tag{2.41}$$

$$= P_{R_1} + P_{R_2}, \tag{2.42}$$

it could be calculated that for $k > k_C$ at $\omega_{L,H}$, the actual delivered power to the load is

$$\boxed{P_{R_2} = \frac{1}{2}\left|V_S\right|^2 \frac{R_1}{\omega_0^2 L_1^2}\left(\frac{Q_1}{Q_2} + \frac{\pm k}{1 \pm k}\right).} \tag{2.43}$$

Obviously from (2.43), the larger the Q_1 with respect to Q_2, the less sensitive the fluctuation in delivered load power is to the coupling k.

There is one more relation that can be useful for practical design, the load power can also be represented as

$$P_{R_2} = \frac{|V_L|^2}{2R_L}. \tag{2.44}$$

Therefore, provided that

$$\frac{Q_1}{Q_2} \gg \frac{\pm k}{1 \pm k}, \tag{2.45}$$

equating (2.43) and (2.44), it could be derived that (again, provided $k > k_C$ and at $\omega_{L,H}$)

$$\boxed{\left|\frac{V_L}{V_S}\right| \approx \sqrt{\frac{L_2}{L_1}}.} \tag{2.46}$$

For $k > k_C$ and at $\omega_{L,H}$, the ratio of the magnitudes of load and source voltages is a fixed value determined by self-inductances only.

To better understand it intuitively, let's look at the equivalent circuits in Fig. 2.25(a). R_{L1} and R_{L2} represent the series resistance of the coils, and R_L represents the load. Ignore the source resistance for now. Note that the expressions for Q_1 and Q_2 have changed:

$$Q_1 = Q_{L1} = \frac{\omega_0 L_1}{R_{L1}}; \tag{2.47}$$

$$Q_2 = (\frac{1}{Q_{L2}} + \frac{1}{Q_{RL}})^{-1}, \tag{2.48}$$

$$\text{where } Q_{L2} = \frac{\omega_0 L_2}{R_{L2}}, \text{ and } Q_{RL} = \frac{R_L}{\omega_0 L_2}. \tag{2.49}$$

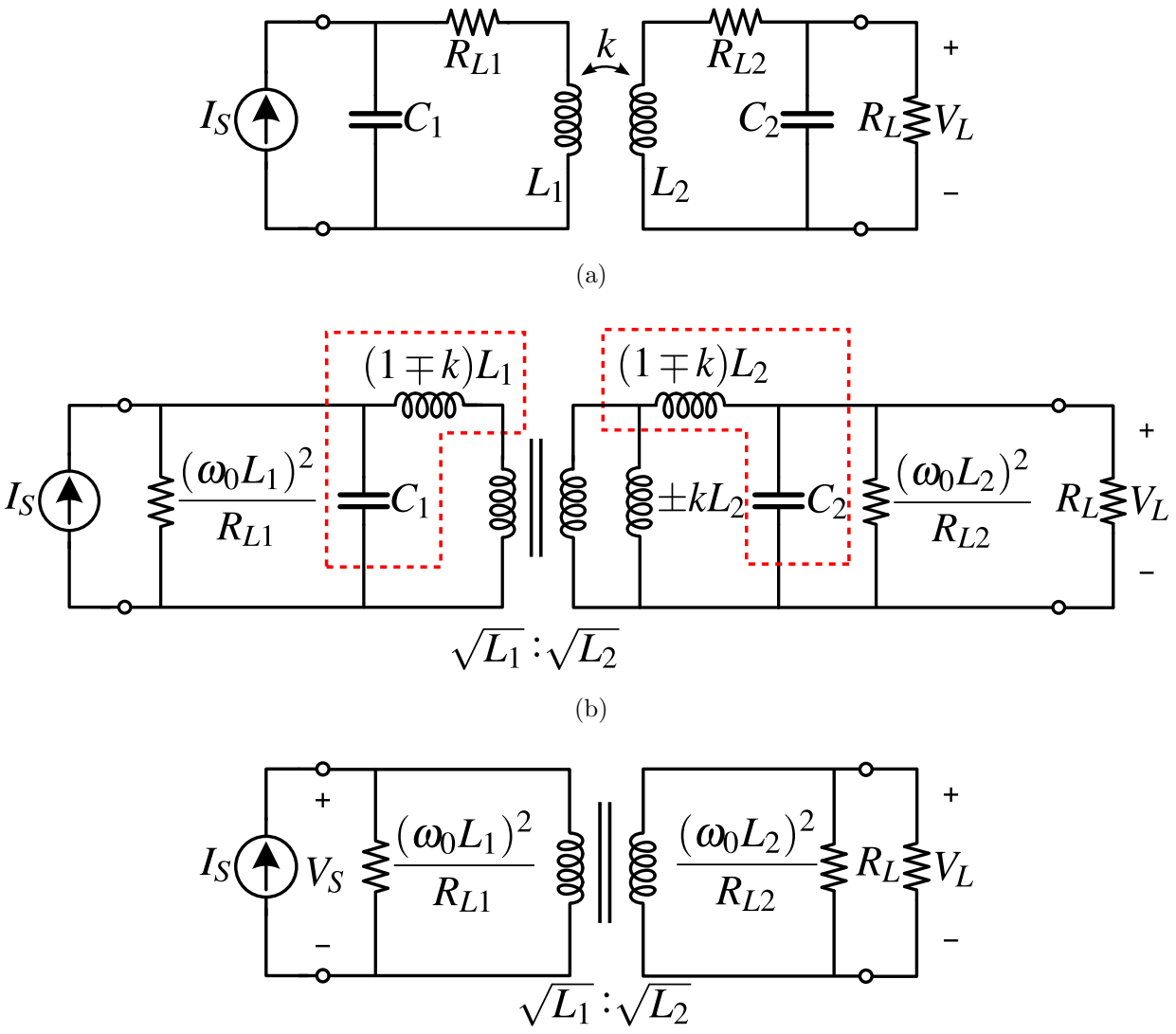

Figure 2.25: (a) Equivalent circuit for near-field wireless power or data system that is composed of parallel coupled resonators. (b) shows the intermediate step of the circuit transformation. (c) shows the final simplified circuit when the system is within regulation range ($k > k_C$) and operates at around either ω_L or ω_H.

If $Q_{L2} \gg Q_{RL}$, then $Q_2 \approx Q_{RL}$. Provided that, when uncoupled, (2.1) holds, and also that quality factors for each LC resonator Q_1, $Q_2 \gg 1$, for $k > k_C$ calculated as before to have resistors dominate inductors, the system can be approximately simplified to Fig. 2.25(c) when I_S is a sinewave at either ω_L or ω_H in (2.9). The input impedance is now purely resistive

and independent of k.

The intermediate step is shown in Fig. 2.25(b). Similar to the derivation illustrated in Fig. 2.5, in Fig. 2.25, (a) $\rightarrow$ (b) by replacing the coupled inductor with its equivalent circuit used before, and performing series-to-parallel transformation for R_{L1} and R_{L2} under the high-Q (Q_1, $Q_2 \gg 1$) assumption; (b) $\rightarrow$ (c) by removing the resonating components in the dashed boxes at $\omega_{L,H}$ (to be more detailed, proper series-to-parallel or parallel-to-series transformations for this high-Q system need to be done), and ignoring the $\pm kL_2$ term provided $k > k_C$.

Apparently from Fig. 2.25(c), the power transfer efficiency is the ratio of power delivered into R_L over the total dissipated power, which includes the power wasted in the two resistors representing inductor series resistance R_{L1} and R_{L2}. Therefore, the total efficiency is given by

$$\boxed{\eta = \frac{Q_1}{Q_1 + Q_2} \times \frac{Q_{L2}}{Q_{L2} + Q_{RL}},} \tag{2.50}$$

where the second term accounts for power loss in R_{L2}, the first for loss in R_{L1}. In practice, the efficiency should take into consideration of other factors such as the power conversion efficiency of the driver, etc., and more details will be convered later.

(2.43), (2.46), and (2.50) are the key equations to guide the design of a robust wireless power transfer system, discussed in the next chapter.

CHAPTER 3

Robust Wireless Power

In Chapter 1, it was discussed that the motivation for this work is to have robust wireless power and reverse data for brain implants. This chapter discusses the design of robust wireless power. It starts with a review of existing state-of-the-art systems and what they were not able to achieve. Following that it discusses how immunity against coupling and load variations (within a certain range) for wireless power can be achieved under the guidance of a thorough understanding of coupled resonators and their key properties introduced in Chapter 2. This chapter also covers the design of power receivers. It then investigates the trade-off between the ability to regulate against coupling and load variations and introduces a method to overcome this trade-off. Finally, the measured performance of a implemented system is shown.

3.1 Prior Arts

Traditionally, to deliver a stable power at the receiver side, the power delivery info can be sent to the transmitter side so that the power level can be adjusted to the optimum. The reverse communication link can be implemented in the form of dedicated data coils [19], an antenna to support 2.4 GHz communication [20], or Load-Shift-Keying (LSK) [21]. However, such methods occupy precious reverse data communication bandwidth. Moreover, to reach the optimum, the system needs to repeat the following step for many times until it converges: the receiver sends the power delivery info. back $\rightarrow$ the transmitter adjusts power level $\rightarrow$ receiver waits until it settles and measures the new power delivery state $\rightarrow$ the receiver sends the new power delivery info. back $\rightarrow$ ... These steps may result in a long latency and do not

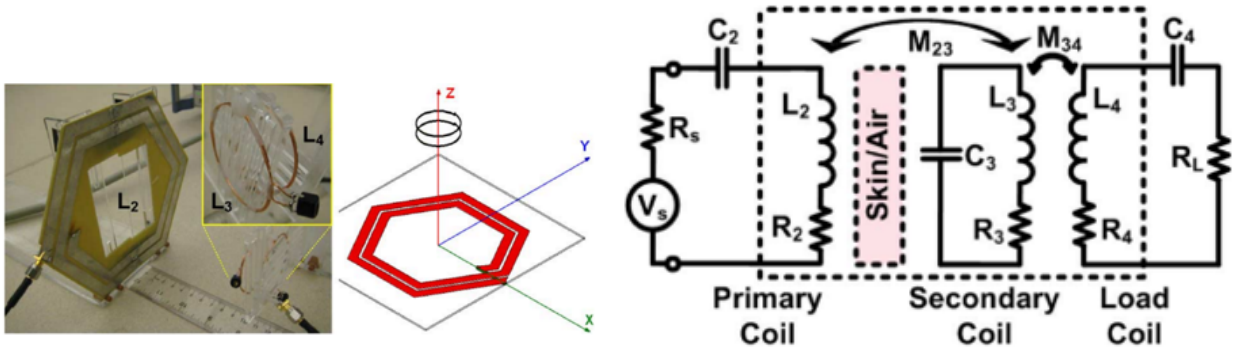

(a) (b)

Figure 3.1: Multi-coil wireless power system from [22]. (a) Photo of the actual design. (b) Schemetics of the system.

work well for highly dynamic environment such as biomedical implants charged by external pieces.

[23] proposed coupled resonators for wireless power transfer, adding a multi-coil configuration to adjust for changes in coil spacing. This has been investigated further by [24, 22, 25]. It requires one or more additional freely-moving coils that are positioned between transmitter and receiver to adjust delivered power. Fig. 3.1 shows a sample design. Similar to the steps in Fig. 2.4, in Fig. 3.1(b), when driven at ω_0, L_4 and C_4 resonate, and R_L can be reflected to middle part as a resistance varying with M_{34}; L_3 and C_3 resonate, reflecting the total resistance to the primary side. Finally, L_2 and C_2 resonate, the driver sees a source R_S and transformed load resistance depending on both M_{23} and M_{34}. If one coupling changes, the other can be adjusted accordingly to ensure stable power delivery. That is as if the quality factor of the receiver is adjusted so that the system acts as in Fig. 2.12(b), where the two Q-curves always intersect at ω_0. A multi-coil method requiring adjustable position is clearly not feasible for biomedical implants.

Toggling the rectifier at the receiver side among multiple modes (e.g. $1\times$, $2\times$, or $1/2\times$, etc.) with a duty-cycle varying with coupling or loading can maintain a constant output voltage across the load, as realized by the R^3 rectifier [27, 26, 28] and Q-modulation [29] techniques. For example, Fig. 3.2 shows the design in [26]. The receiver can be configured

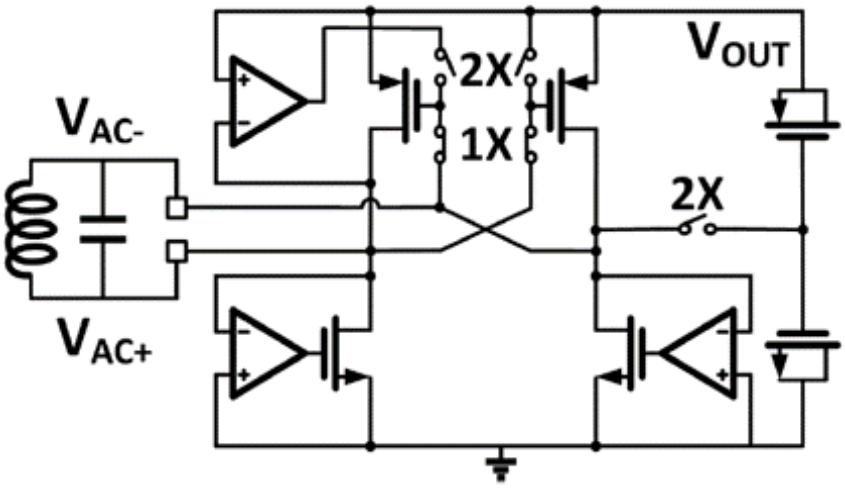

Figure 3.2: 1× 2× wireless power receiver from [26].

as either full-wave rectifier (1×) or voltage doubler (2×). When it's in full-wave rectifier mode, the equivalent AC input resistance is half of the output DC load Fig. 3.3(a); when it's in voltage doubler mode, the equivalent AC input resistance is output DC load divided by eight Fig. 3.3(b). That's as if there are two Q-curves for the receiver, each with different quality factor as shown in Fig. 3.4. With a continuous duty-cycle, any arbitrary average quality factor can be generated so that the average curve can intersect with the transmitting curve exactly at the driving frequency ω_0. However, this design needs power-hungry control blocks at the implant, which is undesirable because the total dissipation inside the human body is strictly limited.

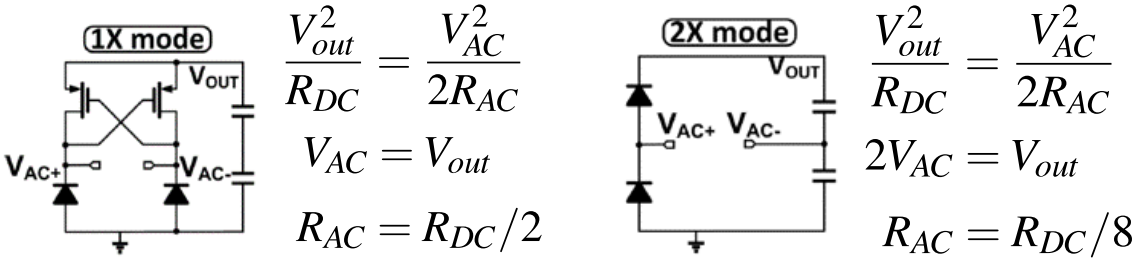

(a) (b)

Figure 3.3: The equivalent circuits and equivalent AC input resistance for 1× and 2× modes for [26].

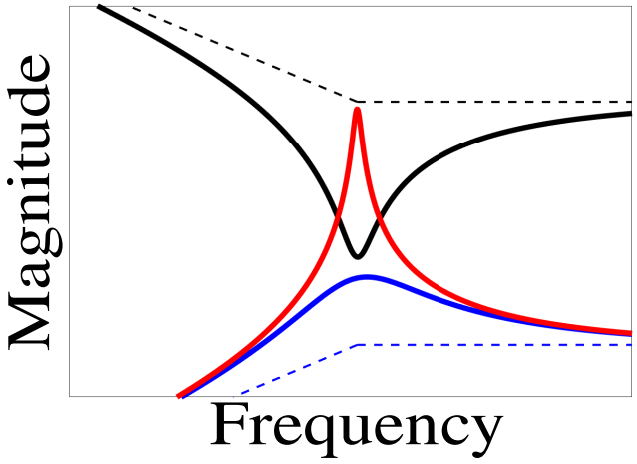

Figure 3.4: Duty-cycling in between the two curves at the bottom can make the system look like Fig. 2.12(b).

There are also reports on adaptive algorithms to adjust transmission to an optimal frequency [30][12][13]. Every time, the operating frequency can be incremented or decremented, and after repetitions the optimal frequency (Fig. 2.12(a)) can be reached. However, the adaptation has a long response time, and is thus not suitable for a dynamic environment. Also, this method requires extra circuitry implementing adaptive algorithms, increasing the complexity of the system and adding extra power-consuming blocks.

Zierhofer [31][32] proposed a wireless power system that self-tunes the carrier frequency to maintain constant power delivery under change in coil separations. This idea was later improved by [33]. But this method was not developed into robust designs that can handle both distance and load variations.

What's desired for a brain implant is robust wireless power that is immune to both coupling and load variations, and operates at high power transfer efficiency. In the next few sections, details of a robust wireless power design will be discussed.

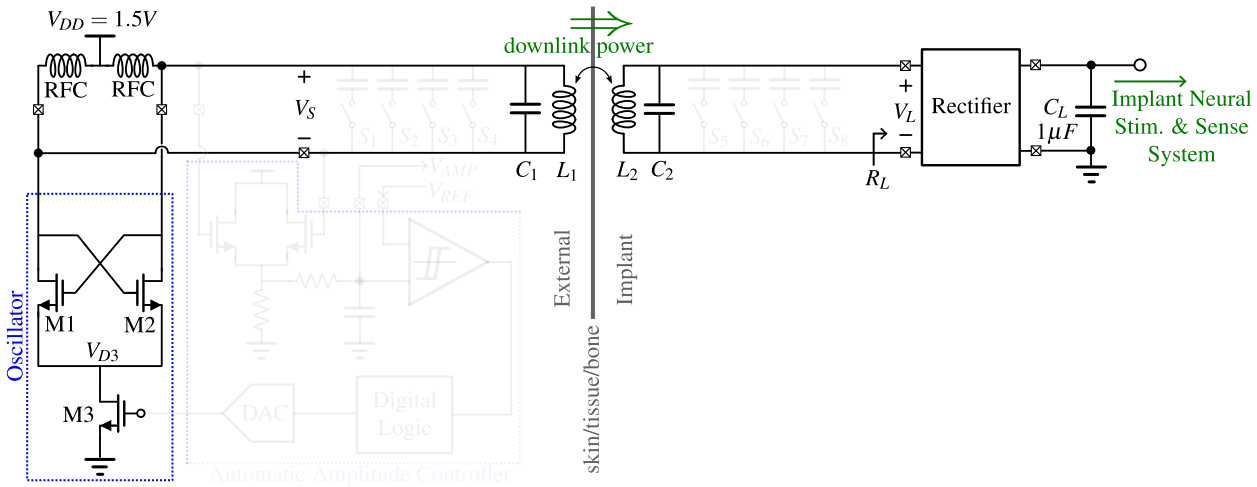

Figure 3.5: When driven by a free-running oscillator, the system is automatically tuned to $\omega_{L,H}$ when $k > k_C$, and the delivered load voltage V_L remains constant under change in k.

3.2 Wireless Power Immune to Coupling Variations

As shown by (2.43), a wireless power transfer system will be largely immune to coupling variations (manifested as change in coil separation distance, misalignment, etc.) if it operates at $\omega_{L,H}$, where these frequencies change with distance. The question now is how to tune the operating frequency automatically to the correct values.

Since the input admittance has zero phase at $\omega_{L,H}$, then if the entire coupled resonator link, including load, is used as the tuning circuit of a cross-coupled differential FET pair (Fig. 3.5), the Barkhausen criterion restricts oscillation to either ω_L or ω_H. The cross-coupled FET pair M1 and M2 with tail current source M3, forms a current-mode free-running oscillator. As the coil separation or misalignment changes, the oscillator adjusts $\omega_{L,H}$ to maintain constant V_L (provided, again, that $k > k_C$). When the coils drop out of the regulation range ($k < k_C$), the two resonant frequencies $\omega_{L,H}$ coalesce into ω_0. The system is then best captured by the equivalent circuit Fig. 2.4(c), sensitive to change in k. With increasing separation distance, the delivered load voltage $|V_L|$ diminishes gradually to zero as $k \to 0$. Fig. 3.6 illustrates this frequency bifurcation.

The oscillator driver needs to satisfy two requirements unique to this application:

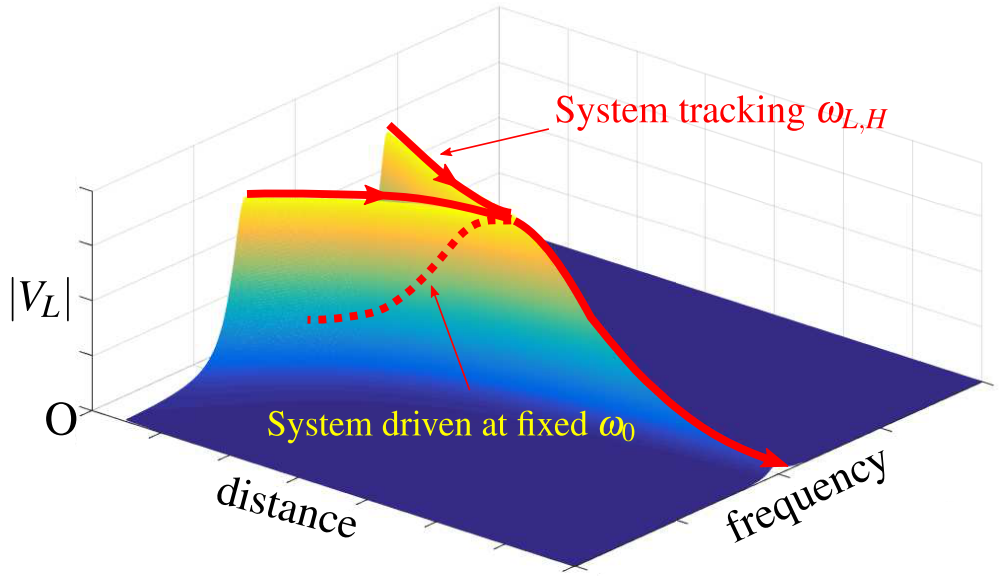

Figure 3.6: Amplitude of load voltage vs. coil separatin distance and system operating frequency. Clearly from the figure, by tracking one of $\omega_{L,H}$, load voltage remains constant as compared with fixing the operating frequency at ω_0.

1. It needs to have a good power conversion efficiency.

2. It needs to ensure a large loaded Q_1 so that (2.45) is satisfied with good margin to make eq. (2.46) hold.

To meet requirement 1, the commutating FETs M1 and M2 are of big width ($W_1 = W_2 =$ 5 mm) so that they act almost like ideal switches. In addition, the average drain voltage of M3 should be small to minimize energy waste in the tail current source:

$$\langle V_{D3}(t) \rangle \downarrow . \tag{3.1}$$

To meet requirement 2, M3 should act like a current source at all times, indicating that the minimum drain voltage of M3 should always be above M3's saturation voltage so that M3 never enters into triode region:

$$min\{V_{D3}(t)\} \geq V_{DSAT}. \tag{3.2}$$

In summary, it's desired to achieve (3.1), given the constraint:

$$V_{DSAT} \leq min\{V_{D3}(t)\} \leq \langle V_{D3}(t)\rangle. \tag{3.3}$$

As will be shown later in Chapter 6, the RF-chokes in the oscillator and the ratio of the junction capacitances of M1,2 and M3 suppress the even harmonics in M3's drain voltage waveform: the ratio of even harmonics in M1,2 over those in M3 equals the ratio of the reactance of (RFC || M1,2's junction capacitance) to the reactance of M3's junction capacitance at frequency of interest. Given that M3's sizing ($10\,\text{mm} \times 1.25\,\mu\text{m}$) is much greater than the sizings of M1 and M2 ($5\,\text{mm} \times 0.35\,\mu\text{m}$), and that the RF chokes are huge ($40\,\mu$H each), V_{D3} is essentially constant with very small ripples. Also, since the tail FET is sized wide enough (10 mm), the saturation voltage of M3 is minimized. Therefore, if the driving strength is selected properly so that the minimum value of V_{D3} stays just above V_{DSAT}, then eq. (3.3) now becomes

$$V_{DSAT} \downarrow = min\{V_{D3}(t)\} \approx \langle V_{D3}(t)\rangle. \tag{3.4}$$

Both requirements for the oscillator drivers are now satisfied simultaneously.

3.3 Wireless Power Immune to Load Variations

As load R_L changes, it is desired that a constant load voltage $|V_L|$ is maintained. Provided that the system operates at one of the split frequencies, (2.46) indicates that $|V_L|$ is a fixed multiple of $|V_S|$. Therefore, as long as the source voltage is held constant, the load voltage remains unchanged as well. This is realized by an automatic amplitude control (AAC).

As shown in Fig. 3.7, the AAC first rectifies the oscillator output voltages into a DC value V_{AMP} by converting the differential oscillation into a single-ended value through the amplitude detector and passing it through a RC low-pass filter. V_{AMP} is proportional to the oscillation amplitude and is then compared with a reference voltage using a hysteresis comparator which absorbs the small remaining ripples on V_{AMP}. Based on the comparison result, the digital logic programs the DAC, implemented with resistor ladders, to set a proper

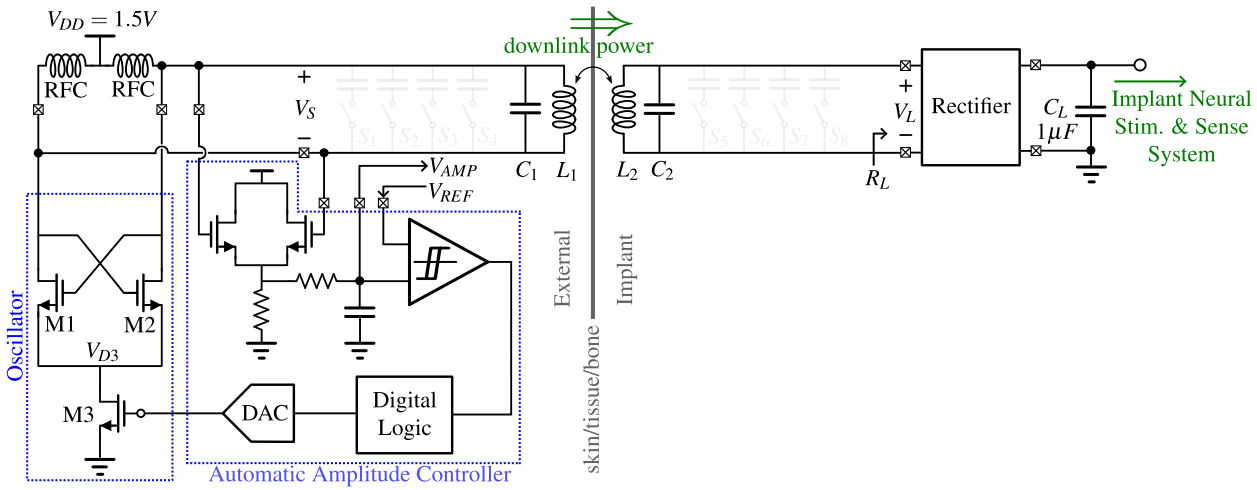

Figure 3.7: Provided the system operates at $\omega_{L,H}$ when $k > k_C$, an automatic amplitude control (AAC) that holds V_S's amplitude constant will also ensure a constant-amplitude V_L at the secondary side.

biasing voltage of the tail current source of the oscillator, so that the right amount of tail current is provided to ensure a constant oscillation amplitude $|V_S|$ under load variations. When k falls below k_C, $|V_S|$ still remains constant but (2.46) no longer applies and therefore $|V_L|$ gradually falls off.

Depending on the application, AAC can be turned off when not needed to further save

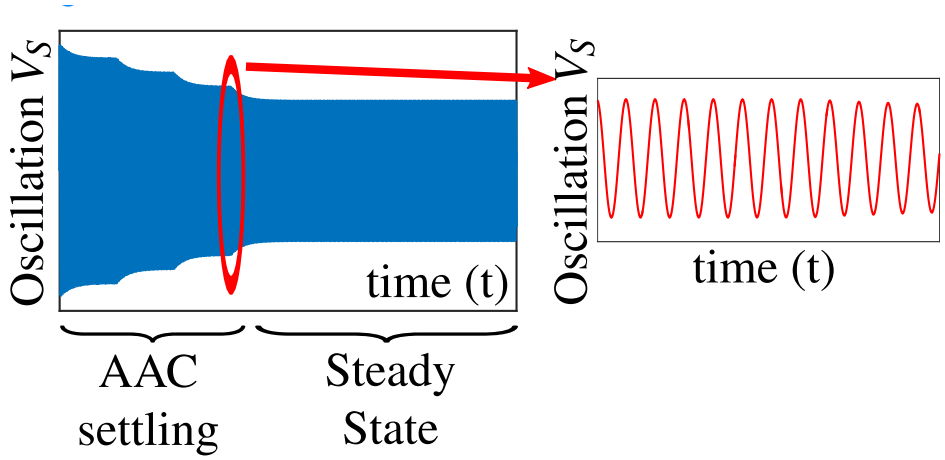

Figure 3.8: Typical operation waveforms for oscillator with AAC. After the voltage amplitude settles, the AAC can be temporarily shut down to save power.

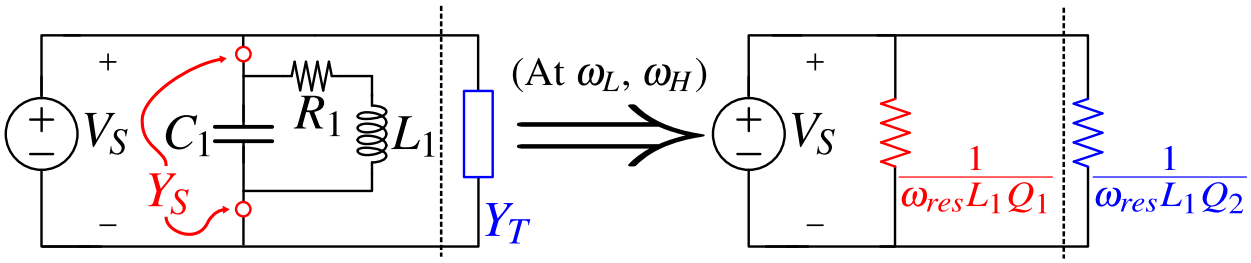

Figure 3.9: Equivalent circuit of oscillator driver with AAC indicates regulated voltage is delivered under change in coupling or load.

power consumption (Fig. 3.8). For example, when the system is used to charge a battery, since battery's input resistance changes slowly as compared with the AAC settling time, the AAC can remain off for most of the time and turn on every few seconds to adjust the load voltage.

The existence of AAC makes the oscillator driver appear as a constant-amplitude variable-frequency voltage source to drive the entire link. This is another way to understand how the system regulates output voltage (Fig. 3.9).

This is a robust wireless power system immune to coupling or load variations. Notably, the system requires no reverse control channel from the secondary side, but, by exploiting properties of magnetically-coupled resonators, *self-regulates* the power delivery.

3.4 Power Receiver Design

The full-wave rectifier (Fig. 3.10) is implemented with active diodes, built with NMOS (M_{N1} and M_{N2}) driven by comparators with added offsets (CMP_1 and CMP_2). During operation, when the differential voltage across L_2 gets larger than the DC voltage across the load, voltage of one side of the L_2 falls below ground level. Therefore, either M_{N1}-M_{P2} or M_{N2}-M_{P1} pair will conduct to deposit charge on C_L. To ensure the conduction starts and ends right at the zero-crossing considering that there will be delay in the comparators. Both CMP_1 and CMP_2 are implemented with programmable offsets. They start to operate slightly before the zero-crossing, so that the corresponding NMOS can be switched ON/OFF right at the

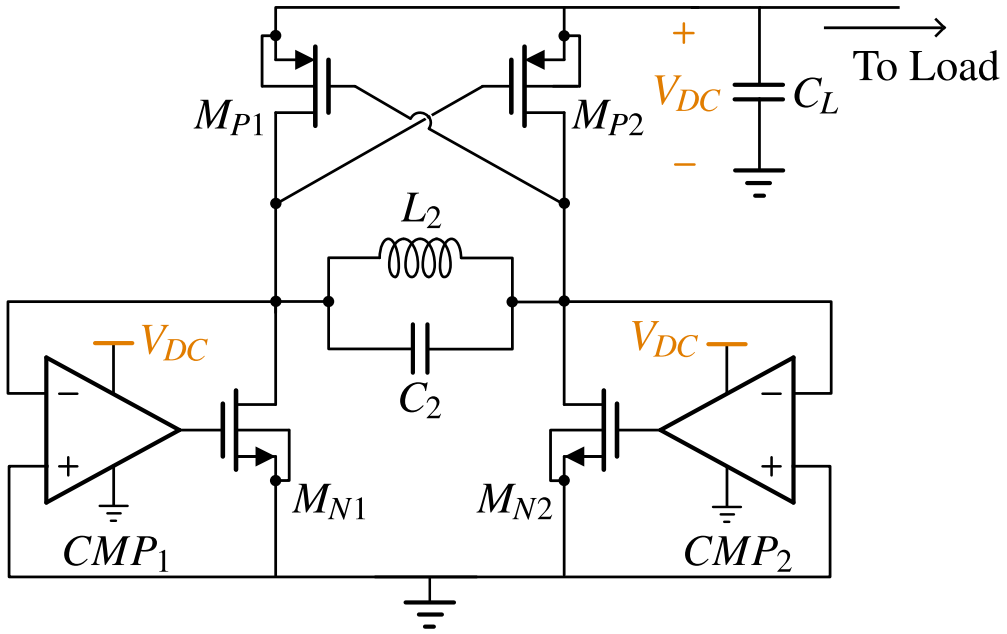

Figure 3.10: Schematic of the rectifier.

zero-crossing to prevent any reverse current flow. The substrates of all the PMOS, including M_{P1}, M_{P2}, and those in the comparators, are all connected to V_{DC} which has the highest potential over the receiver chip.

The rectifier is optional in some cases. For example, when the received power needs to be transmitted on wires through human body, it needs to be in the form of AC for safety consideration. Therefore, voltage rectification can be performed at the local terminals if needed. The delivered voltage will remain regulated under change in coupling or load in either case.

3.5 Trade-off Between Regulation Against Coupling Variations and Regulation Against Load Variations

The given system should deliver a constant V_L for a wide range of coupling k. Also, it is desired that the system can handle order-of-magnitude changes in the load R_L. However, for the system in Fig. 3.7, both of these goals cannot be met at the same time because of the

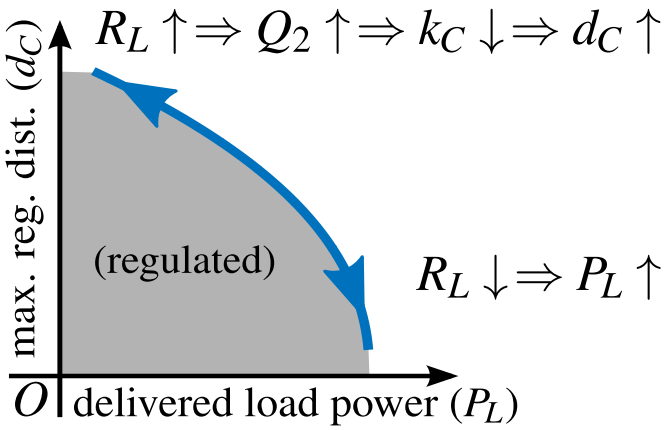

Figure 3.11: There exists a trade-off between maximum regulation distance and delivered load power.

trade-off illustrated in Fig. 3.11.

To handle a large variation in the coupling and thus extend the regulation distance (d_C) across which $k > k_C$, using (2.8)

$$d_C \uparrow \Rightarrow \; k_C \downarrow \Rightarrow \; Q_2 = \frac{1}{k_C} \uparrow . \tag{3.5}$$

Provided ω_0, L_2, and R_{L2} are fixed, according to (2.48) and (2.49), the only way to increase Q_2 is

$$R_L \uparrow \Rightarrow \; Q_{RL} = \frac{R_L}{\omega_0 L_2} \uparrow \Rightarrow \; Q_2 = (\frac{1}{Q_{L2}} + \frac{1}{Q_{RL}})^{-1} \uparrow . \tag{3.6}$$

But according to (2.44),

$$R_L \uparrow , \, |V_L| \text{ constant } \Rightarrow \; P_L \downarrow . \tag{3.7}$$

The total delivered power P_L diminishes.

When a higher power P_L is demanded, it means that the equivalent R_L must be smaller. But a small R_L shortens the maximum regulation distance (d_C):

$$P_L \uparrow \Rightarrow \; R_L \downarrow \Rightarrow \; Q_2 \downarrow \Rightarrow \; k_C = \frac{1}{Q_2} \uparrow \Rightarrow \; d_C \downarrow . \tag{3.8}$$

The system can only operate with the highest regulation distance while delivering the minimum power; when called to handle large variations in the load while maintaining regulation, it can do so over a very limited range of coil separation. This trade-off may become

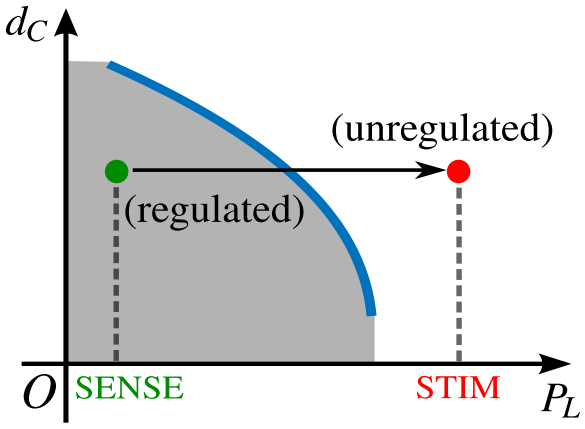

Figure 3.12: As system switches its operating mode, it is at the risk of departing regulated power delivery range.

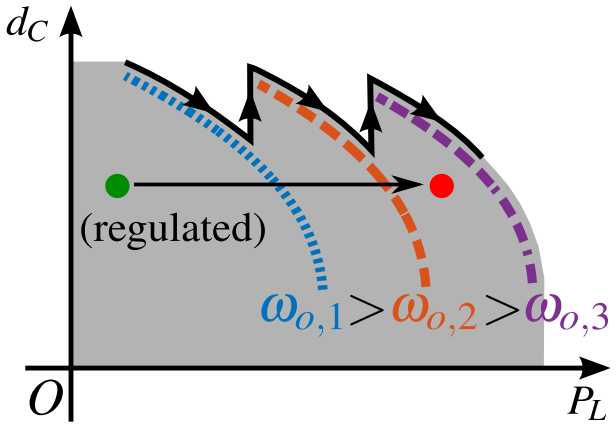

Figure 3.13: To overcome this trade-off, center frequency ω_0 can be programmed at different levels.

problematic in practical application related to this work. For example, consider the case that multiple stimulation engines in the implant are commanded to turn on thus, all of a sudden, the system demands much higher power. This can throw the system out of the regulation range (Fig. 3.12) and as a result the voltage at the implant, V_L, drops.

But these dependencies can be overcame by adjusting the center frequency ω_0. Provided the system stays within regulation range, the delivered load voltage V_L has a fixed amplitude. Therefore, when R_L drops, ω_0 is programmed to go down linearly with R_L (in discrete steps

for a practical realization). Then k_C remains unchanged:

$$R_L \downarrow, \omega_0 \downarrow \Rightarrow \; Q_2 \approx \frac{R_L}{\omega_0 L_2} \text{ constant } \Rightarrow \; k_C = \frac{1}{Q_2} \text{ constant.} \tag{3.9}$$

As a result, the regulation distance (d_C) stays almost the same (Fig. 3.13) with increased power delivery.

If now the implant switches back from high power demand to low power (i.e. R_L increases), the system will remain in the regulated operating range. But as given by (2.49) and (2.50),

$$R_L \uparrow, \omega_0 \text{ constant } \Rightarrow \; Q_{RL}, Q_2 \uparrow \Rightarrow \; \eta \downarrow, \tag{3.10}$$

that is, the system's total power transfer efficiency will drop. So although load voltage continues to self-regulate, power is being wasted. Therefore, for the sake of efficiency ω_0 should switch back to a higher frequency.

In general, ω_0 should roughly track changes in R_L, so that system maintains good regulation range and power transfer efficiency.

The four discrete center frequencies can be realized with eight switchable capacitors $S_1 - S_8$, four on each side (Fig. 3.14). Depending on the load, the system can operate at

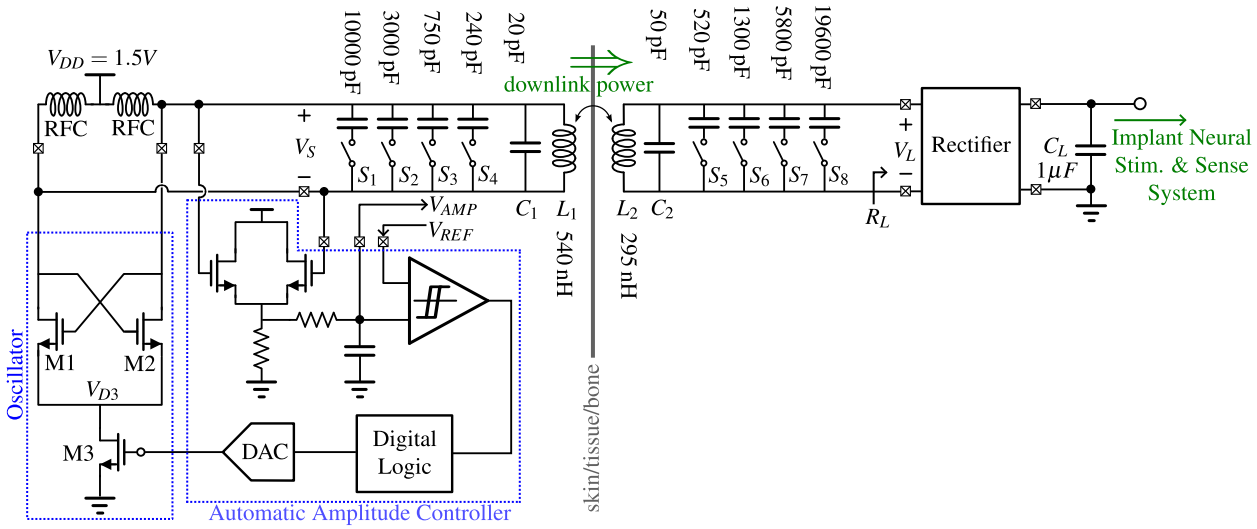

Figure 3.14: Full schematics of the wireless power transfer system. Eight switchable capacitors can help enlarge the regulation range.

one of 13.56 MHz, 6.78 MHz, 3.39 MHz, or 1.8 MHz. Roughly, they span a $8:4:2:1$ ratio which, as we will be shown later, extends the load variation range to $40\times$.

Each center frequency is tailored to a subrange of load power demand. It can be selected by looking up a stored table. Alternatively, it can be determined in real time. For each center frequency, the DAC in the AAC spans a range of tail currents.

$$I_{tail}(\omega_0) \in [I_{min}(\omega_0), I_{max}(\omega_0)]. \tag{3.11}$$

If, for example, R_L decreases greatly, the AAC loop responds by pushing the DAC to raise I_{tail}. But if ω_0 is too high the DAC will saturate at I_{max}. This indicates to the system to switch in a larger capacitance in the primary and secondary to lower ω_0.

3.6 Performance of the Design

The system was implemented using 180 nm CMOS. Coils are hand-wound using AWG 18 copper wires, and both have 3 cm diameters. The transmitting coil has 3 turns, and is measured to have $Q_{L1} = 175$ at 14 MHz; the receiving coil has 2 turns, with $Q_{L2} = 135$ at 14 MHz. The coils can be designed with the help of Terman's formula [34].

The performance of wireless power transfer was measured for four different center frequencies.

Figure 3.15 is the legend for all three subsequent figures.

Figure 3.16 plots the delivered load voltage vs. varying coil separation distance. Clearly, delivered load voltage is constant up until a critical distance determined by the critical coupling coefficient k_C, which is inverse of quality factor of the secondary side. The larger the quality factor is, the longer the regulation range gets.

Figure 3.17 plots the corresponding power transfer efficiency for those in Fig. 3.16. Here,

Figure 3.15: Legend for the subsequent figures: Fig. 3.16, Fig. 3.17, and Fig. 3.18.

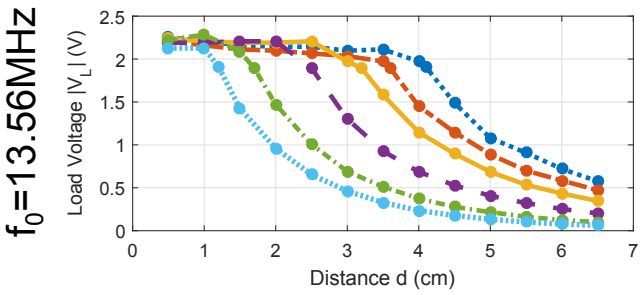

(a)

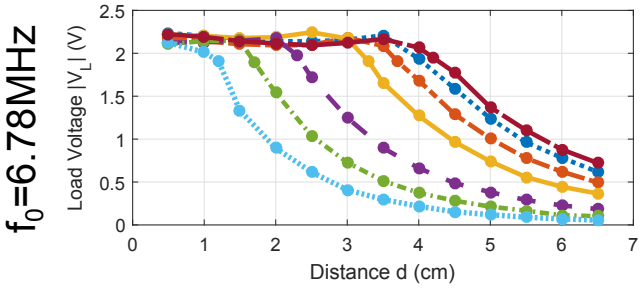

(b)

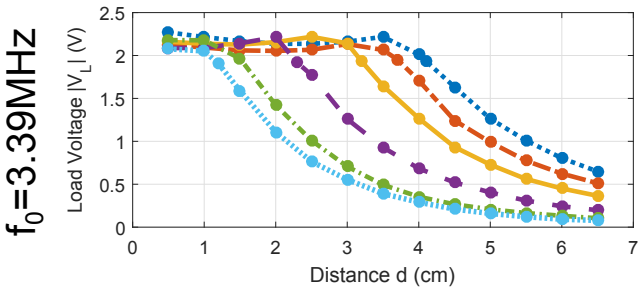

(c)

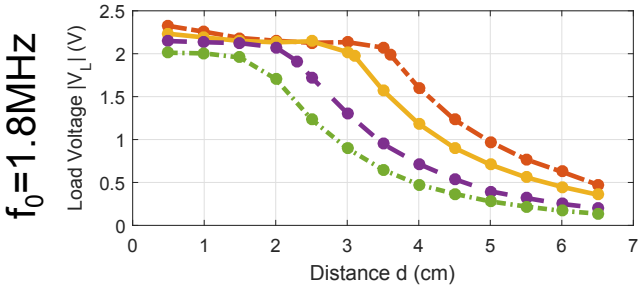

(d)

Figure 3.16: Delivered load voltage vs. distance for f_0 = (a) 13.56 MHz; (b) 6.67 MHz; (c) 3.39 MHz; (d) 1.8 MHz.

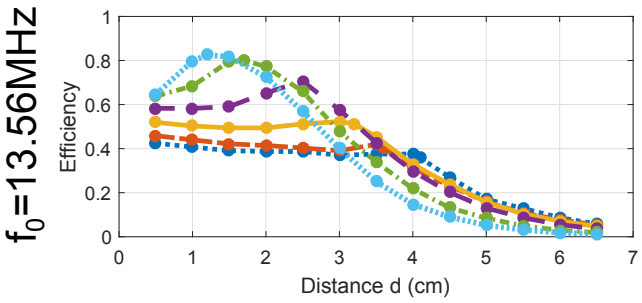

(a)

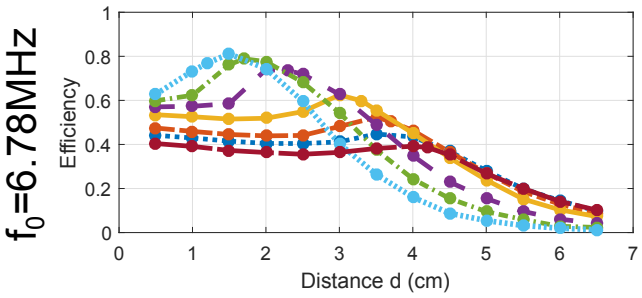

(b)

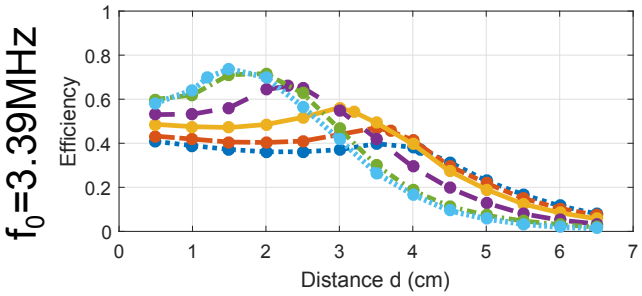

(c)

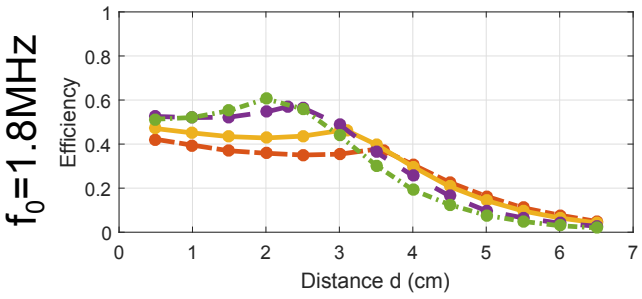

(d)

Figure 3.17: Power transfer efficiency vs. distance for f_0 = (a) 13.56 MHz; (b) 6.67 MHz; (c) 3.39 MHz; (d) 1.8 MHz.

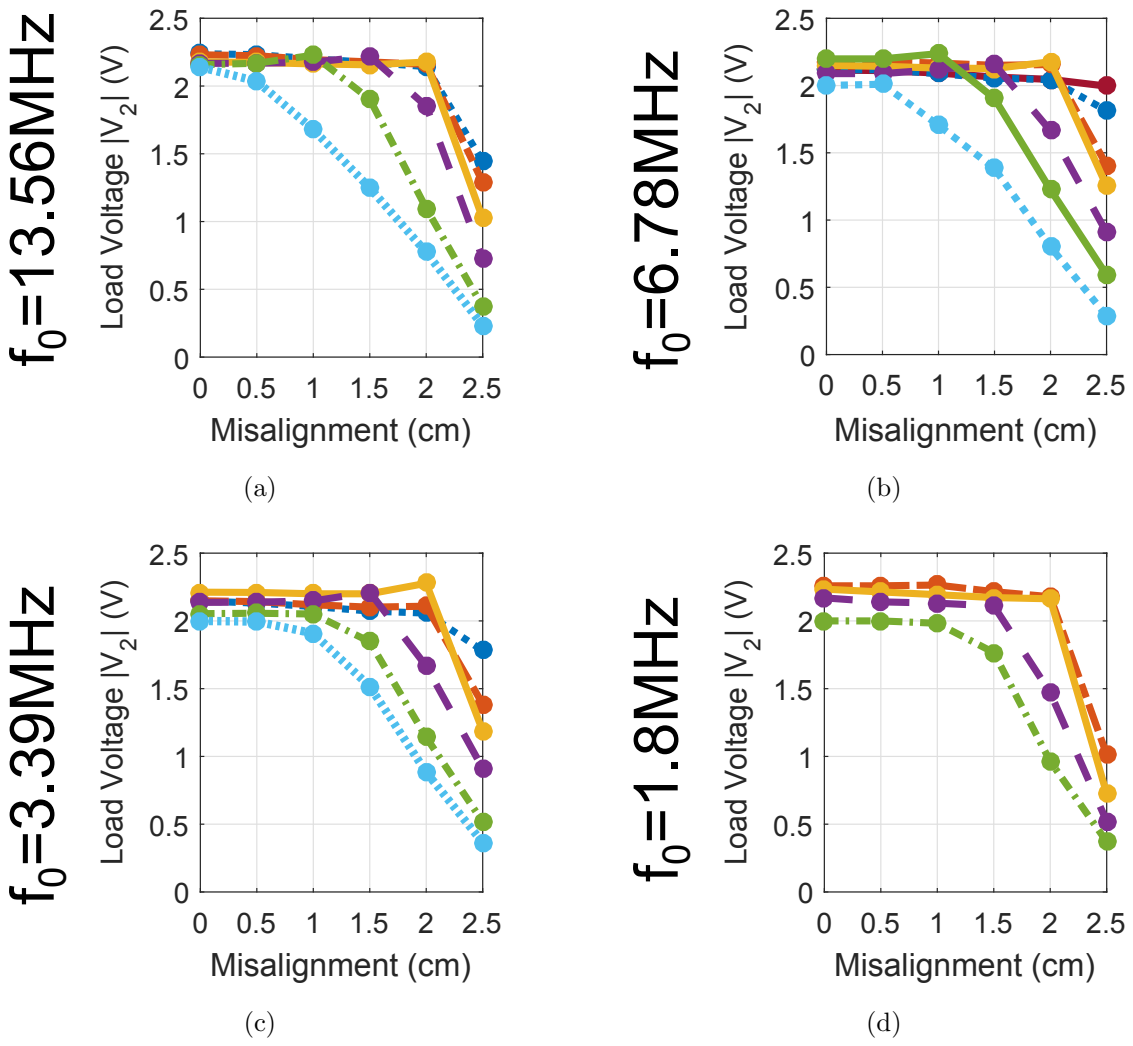

Figure 3.18: Delivered load voltage vs. axial misalignment for f_0 = (a) 13.56 MHz; (b) 6.67 MHz; (c) 3.39 MHz; (d) 1.8 MHz.

larger quality factor of the secondary side reduces the power transfer efficiency. The peak efficiency can reach more than 80%; the lowest efficiency remains above 35%.

Figure 3.18 plots the delivered load voltage vs. axial misalignment (spacing coils 1 cm apart and move one of them horizontally). The wireless power also demonstrates great robustness in handling coil misalignment.

To better visualize the wireless power operating range, delivered load voltage with respect to load resistance and coil separation distance is plotted in Fig. 3.19. It is clear that for

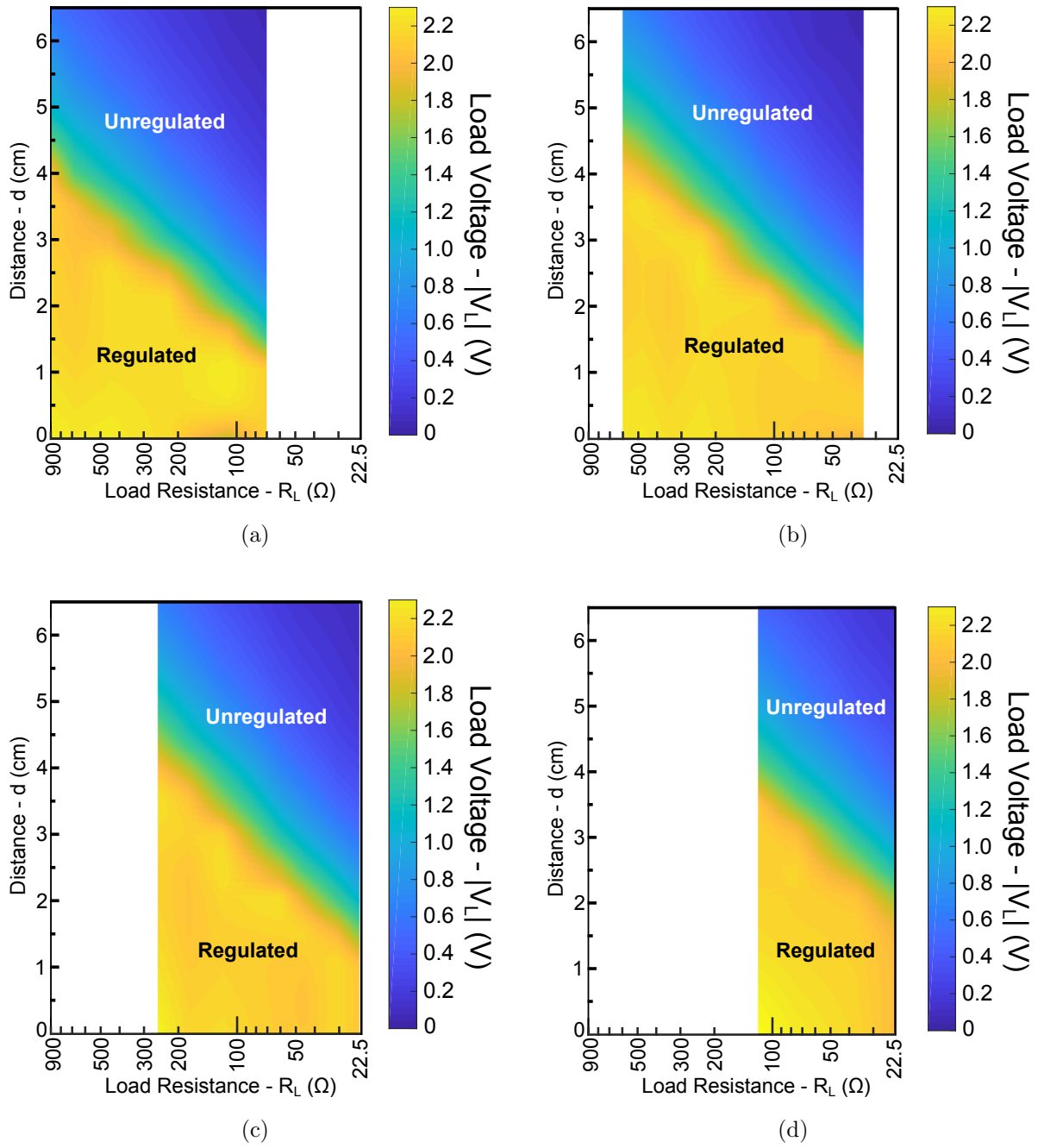

Figure 3.19: Delivered load voltage vs. coil separation distance and load resistance for f_0 = (a) 13.56 MHz; (b) 6.67 MHz; (c) 3.39 MHz; (d) 1.8 MHz.

heavier loads, the regulation distance shrinks as discussed before (Fig. 3.11). Each center frequency can cover a certain range of load resistance. When combining all of them together

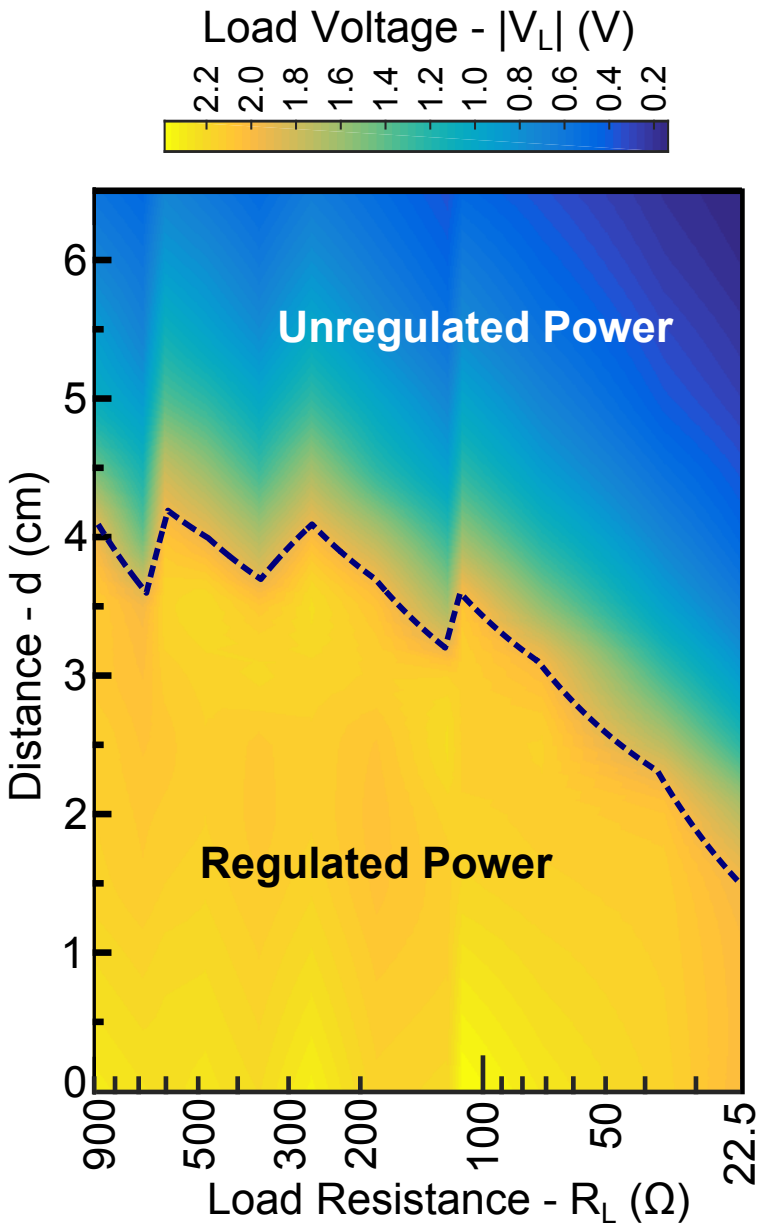

Figure 3.20: Delivered load voltage vs. coil separation and load resistance when the system can be programmed to operate at four different center frequencies. It has a much extended regulation range.

in a proper way, a much extended regulation range is achieved as shown in Fig. 3.20. Note that within the regulation range, the voltage is around 2∼2.3 V, and when it gets out of the regulation range, delivered load voltage gradually decays to zero as illustrated in Fig. 3.6.

To have a better sense of the range extension, the performance can be compared with

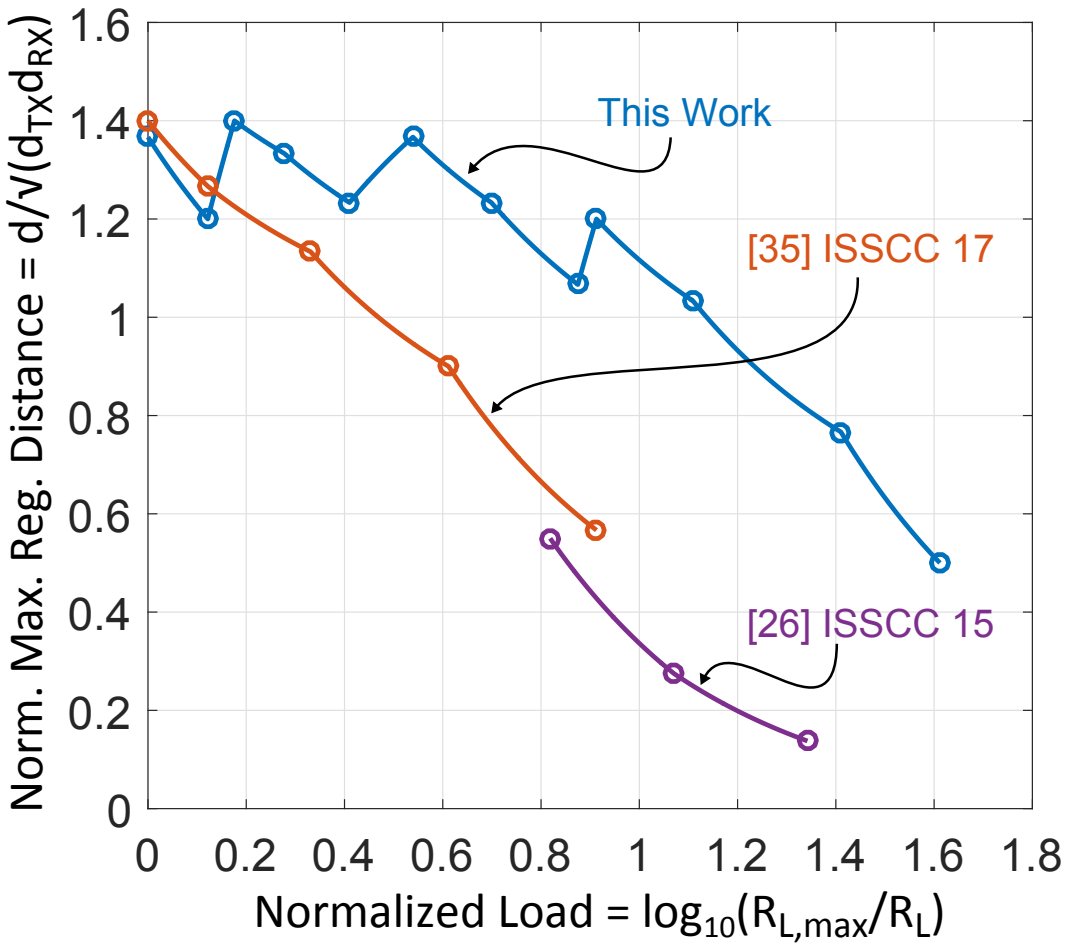

Figure 3.21: Normalized regulation ranges of different work. This work has a much larger normalized operating range compared with others.

other state-of-the-art work with proper normalization. For the distance, it can be normalized by dividing over the geometric mean of the coil diameters to account for the different sizes of coils [33]. For the load, it can be normalized to the minimum power delivery when efficiency is still above a reasonable value, 35%. In other words, normalized load is counting how many times of load variations can the system handle, and therefore, should be plotted on logarithmic scale. Clearly from Fig. 3.21, this work has a much extended range as compared with [35] and [26].

This is the design of a robust wireless power transfer system, capable of handling both coupling and load variations with extended range. In the next chapter, a reverse data link

on top of this forward power will be introduced. The simultaneous reverse data over the same pair of coils is made possible by the L-RSK modulation scheme.

CHAPTER 4

Load-Induced Resonance-Shift Keying (L-RSK)

4.1 Prior Arts

The traditional carrier-based modulation is ruled out for this application, because not only does this method require an extra pair of coils or antenna, but also, this method is power-hungry due to the power-consuming carrier-generation circuits.

Load-Shift Keying (LSK), sometimes referred to as "backscattering" although in the near-field it is mere transformer action, switches a resistor at implant to set the oscillation to different amplitude levels, and this "amplitude-shifting" can be sensed by the external piece for demodulation. It does not need any extra coil; also, it burns very little power. LSK was optimized by [36][37] and applied to biomedical systems [38, 39, 40]. However, LSK relies on the difference in amplitude, which means that no stable power flow can be

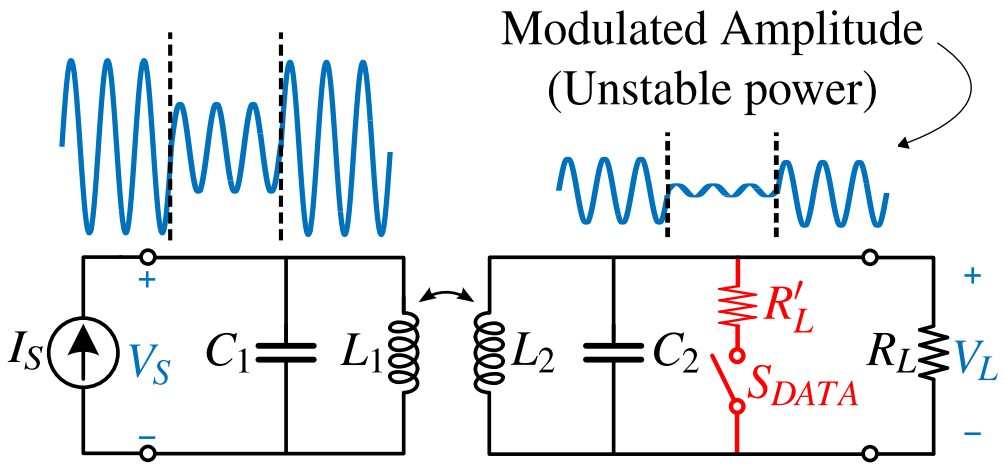

Figure 4.1: Load-Shift Keying (LSK) modulates the amplitude of oscillation: the delivered power will fluctuate with the reverse data.

supported at the same time (Fig. 4.1).

Ultra-Wide-Band radio (UWB) can consume very little power because there is no need for carrier-generation and, instead, data is carried by "pulses". But there are two problems with this method. First, for coupled-resonators with high quality factors, which is the case for good wireless power systems, the communication channel is band-limited. This means that every time a pulse is sent, there will be long-time ringing when it's received. The inter-symbol interference makes the demodulation almost impossible. [41] solved this problem of ringing by sending a "suppression pulse" in addition to the initial pulse with proper timing, so that the ringing by the suppression pulse can cancel that by the initial pulse (Fig. 4.2).

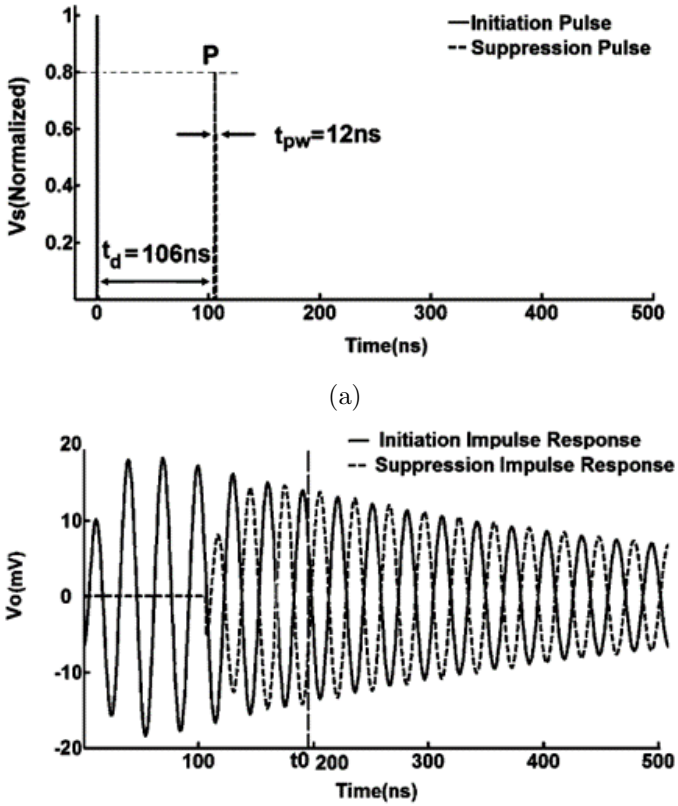

(a)

(b)

Figure 4.2: Pulse-Harmonic Modulation [41]: (a) A second pulse, the suppression pulse, is sent at a proper delay after the initial pulse. (b) As a result, the ringing of the second pulse can cancel that of the first one.

Even if this problem was solved, UWB still faces the problem that data transmission may be jammed by a strong tone carrying wireless power. [42] demonstrates simultaneous forward data using an extra pair of coils. But techniques for reverse data transmission are missing. Moreover, UWB radios typically require an extra pair of coils or antenna dedicated to the data communication.

Cyclic on-off-keying (COOK) [43] has demonstrated simultaneous forward power and reverse data. To transmit bits, the LC tank at the secondary side can be shorted at different instances of a bit period. The change in amplitude at the primary side is detected for data demodulation Fig. 4.3. The shortcoming of COOK is that the delivered wireless power is unregulated and not robust against change in coils separation, their misalignment, or

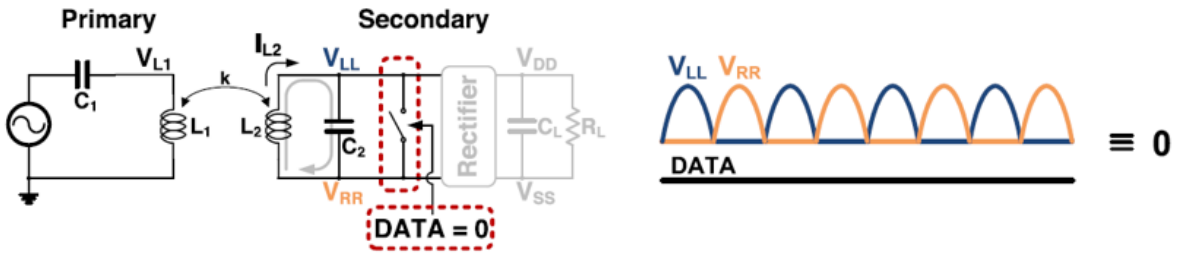

(a)

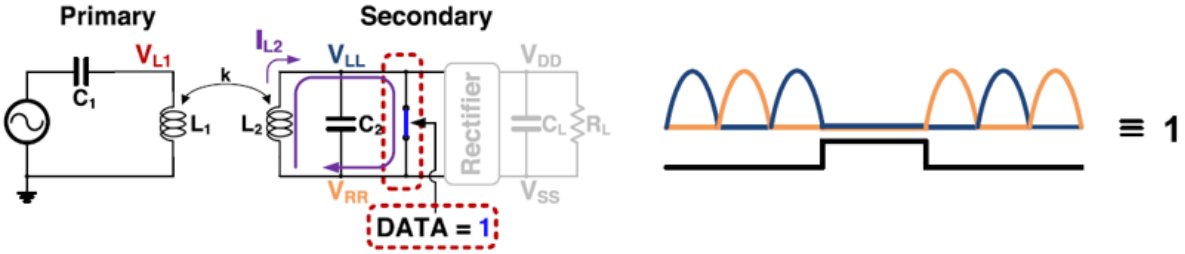

(b)

Figure 4.3: Cyclic On-Off Keying (COOK) [43]: (a) When data bit is zero, switch on secondary side remains open for the entire bit period. (b) When data bit is one, switch on secondary side is closed for short amount of time within that bit period, so that power delivery is still largely continous. Data is demodulated at the primary side by sensing the slight amplitude difference at V_{L1} due to different switching activities.

variations in load currents.

What's desired is reverse data communication that can be on simultaneously with the regulated wireless power, preferably over only a single pair of coils only. It should support high-rate data ($\sim$1 Mb/s for the brain implant discussed in Chapter 1), and should burn minimum power for data modulation at the implant side. This can only be done with a novel data modulation scheme: Load-Induced Resonance-Shift Keying (L-RSK). Before introducing L-RSK, let's take a look at the mode-selection of a free-running oscillator when driving coupled resonators.

4.2 Theories behind the Selection of Oscillation Mode

It was shown previously that when the coupling is strong enough ($k > k_C$), the system can oscillate at three frequencies (ω_0, ω_L, and ω_H) which satisfy the Barkhausen criterion. But in practice the system will always select one of these three oscillatory modes. The selection of the operating mode is not random. To analyze this, let's take a look at the system's transimpedance gain.

Fig. 4.4 plots the transimpedance gain from source I_S to load V_L in the circuit of Fig. 2.25(a). Depending on the coupling k, there are three different cases:

1. When coils are far apart, $k < k_C$ (under-coupled). The system only has one resonant frequency at ω_0 where $\angle(V_S/I_S) = 0$.

2. As coils come together, k increases. When $k = k_C$, the system is at critical coupling. There is still one resonant frequency ω_0 where the transimpedance gain reaches its maximum.

3. As coils are brought even closer, $k > k_C$ (over-coupled). Now in addition to the original resonant frequency ω_0, there are two resonant frequencies that split around ω_0. They are ω_L and ω_H as given by (2.9). At either frequency, the equivalent circuit looks like Fig. 2.25(c) and the transimpedance gain is at a peak.

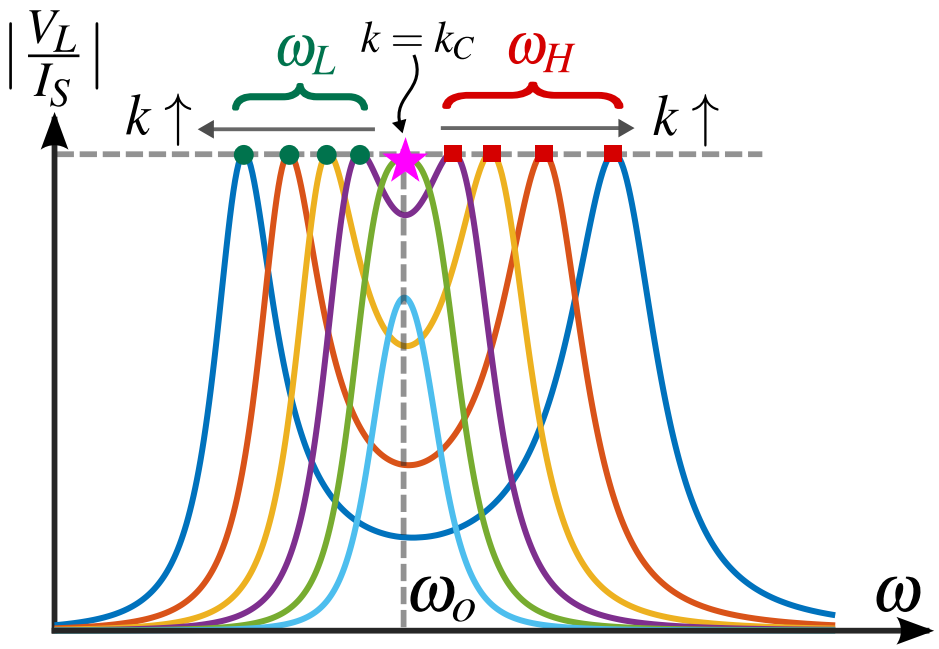

Figure 4.4: The transimpedance gain plot for different k values, illustrating the under-coupled, critical-coupling, and over-coupled scenarios.

All of these are based on the equal-resonance assumption in (2.1), but in practice, there will always be some mis-tuning in the resonant frequencies of the two standalone LC tanks. The mis-tuning can result from the asymmetry due to practical implementation, or it can be introduced deliberately.

A small mis-tuning tilts the transimpedance frequency response, as shown in Fig. 4.5(a). The transimpedance gain at ω_H is slightly higher than that at ω_L, and gain at ω_0 is much lower. Let's focus on the resonance at ω_L and at ω_H. At startup, oscillation will be stimulated at both frequencies; in theory, steady-state oscillation can be a superoposition of more than one non-harmonic frequency. However, because of a slightly larger gain in the oscillator loop, oscillation at ω_H will grow faster than that at ω_L and push the differential pair into gain compression. As [44] explains, the mode that grows faster progressively lowers the effective oscillator loop gain for the slower growing mode at ω_L until it is squelched completely. Similarly, if the system is mis-tuned in the contrary sense, the transimpedance gain will be tilted the other way (Fig. 4.5(b)) so in steady state, oscillation at ω_L will prevail. In either

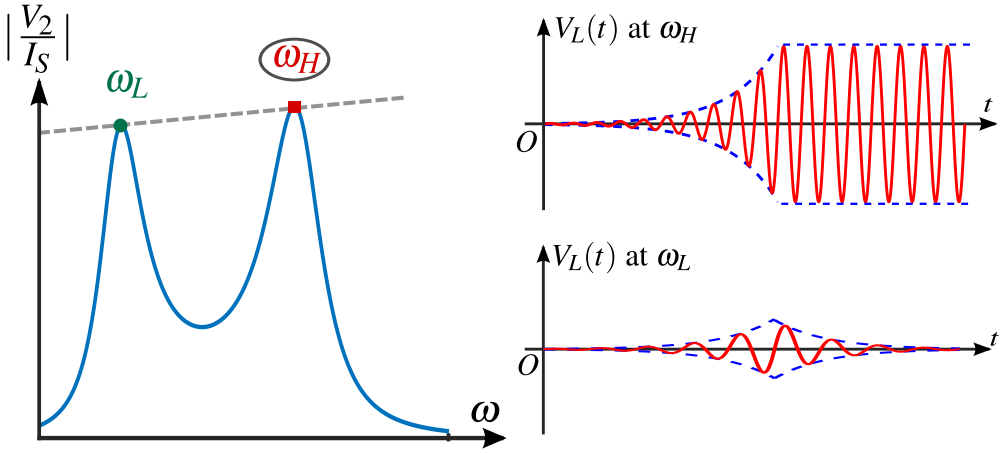

(a)

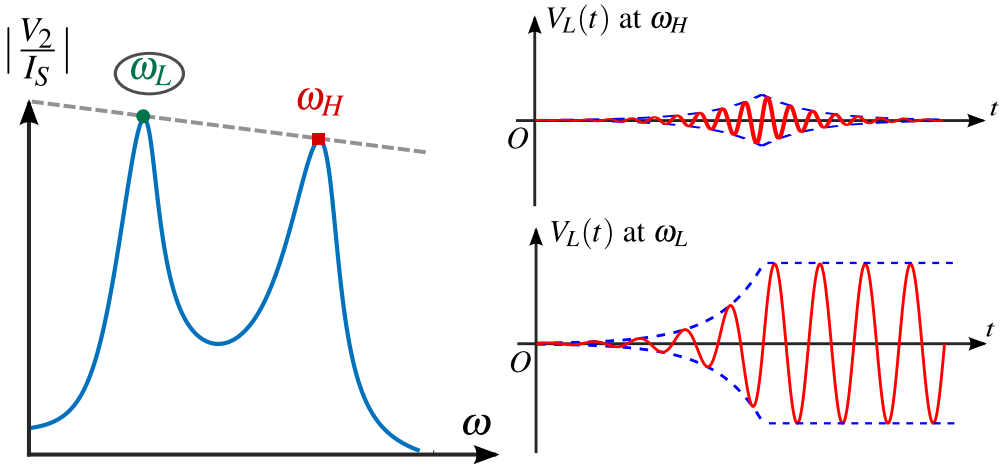

(b)

Figure 4.5: (a) With mistuning, if the original transimpedance gain of Fig. 4.4 is tilted this way, then the oscillation at ω_H can eventually dominate in the steady state. (b) Similarly, if the system is mistuned in the reverse direction, oscillation at ω_L prevails in the steady state.

case, since the transimpedance gain at ω_0 is much smaller than the other two frequencies, this will always be squelched. Besides, given the opposite curvature of the transimpedance frequency response here, even if oscillation at ω_0 were to somehow spring up, it would be unstable under perturbations.

As shown in Fig. 4.6, for a fixed mis-tuning, all curves for $k > k_C$ will be tilted towards the same direction. Therefore, the frequency of steady-state oscillation is guaranteed at one

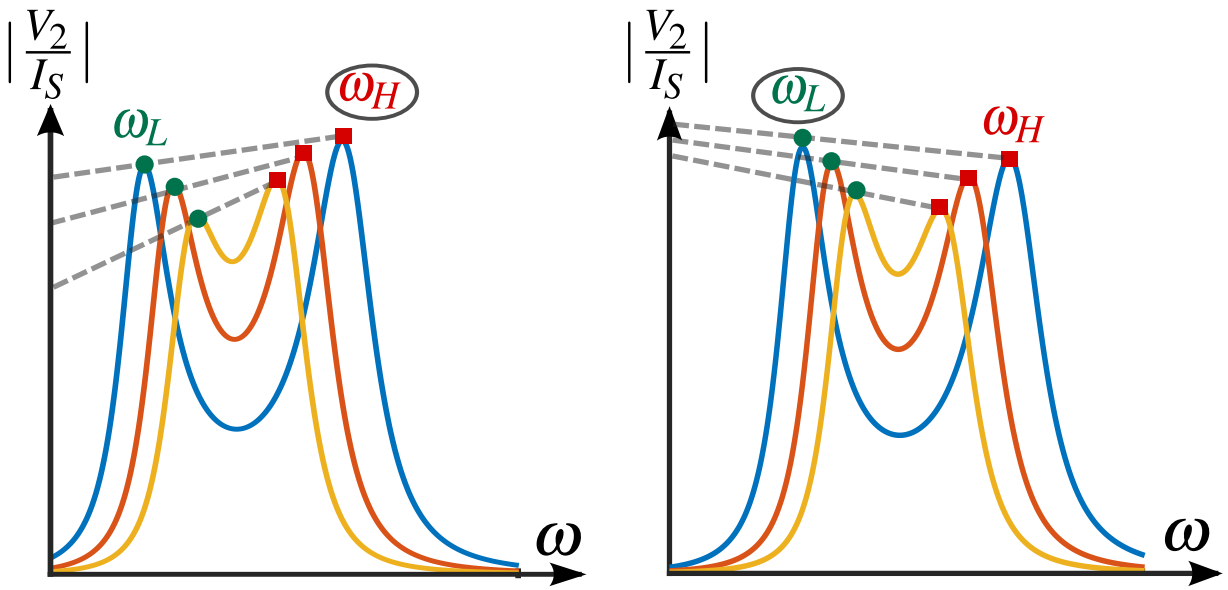

(a) (b)

Figure 4.6: Both (a) and (b) indicate that for a certain mis-tuning, all curves for $k > k_C$ are tilted towards the same direction. This consistency lays the foundation for our proposed new data modulation scheme.

of $\omega_{L,H}$ for coil separation up to d_C unless the mis-tuning is reversed. A way to transmit data is through deliberate mis-tuning, so that oscillation can be initiated at either of $\omega_{L,H}$.

Among the many ways to create the mis-tuning as mentioned previously, the easiest one is to switch in/out a small capacitor ΔC_2.

To understand the mechanism intuitively, consider the equivalent circuit in Fig. 4.7. Different from the actual realized system, we use series coupled resonators for ease of intuitive illustration, and as shown in Fig. 2.25, parallel coupled resonators have similar conclusions. When ΔC_2 is switched in, $C_2 \to C_2 + \Delta C_2$. The original resonant frequency of the secondary LC-tank when uncoupled becomes slightly lower than that of the primary LC-tank. This is as if $C_1 \to C_1 - \Delta C_1$, or equivalently, a large αC_1 is inserted in series. Similarly, if ΔC_2 is switched out, it's equivalent to a $-\alpha C_1$ in series with C_1 (Fig. 4.7 (a)).

The circuit at the dashed line can be broken into into two parts and analyzed separately. As shown in Fig. 4.7(b), in the left part of the circuit, depending on whether ΔC_2 is switched

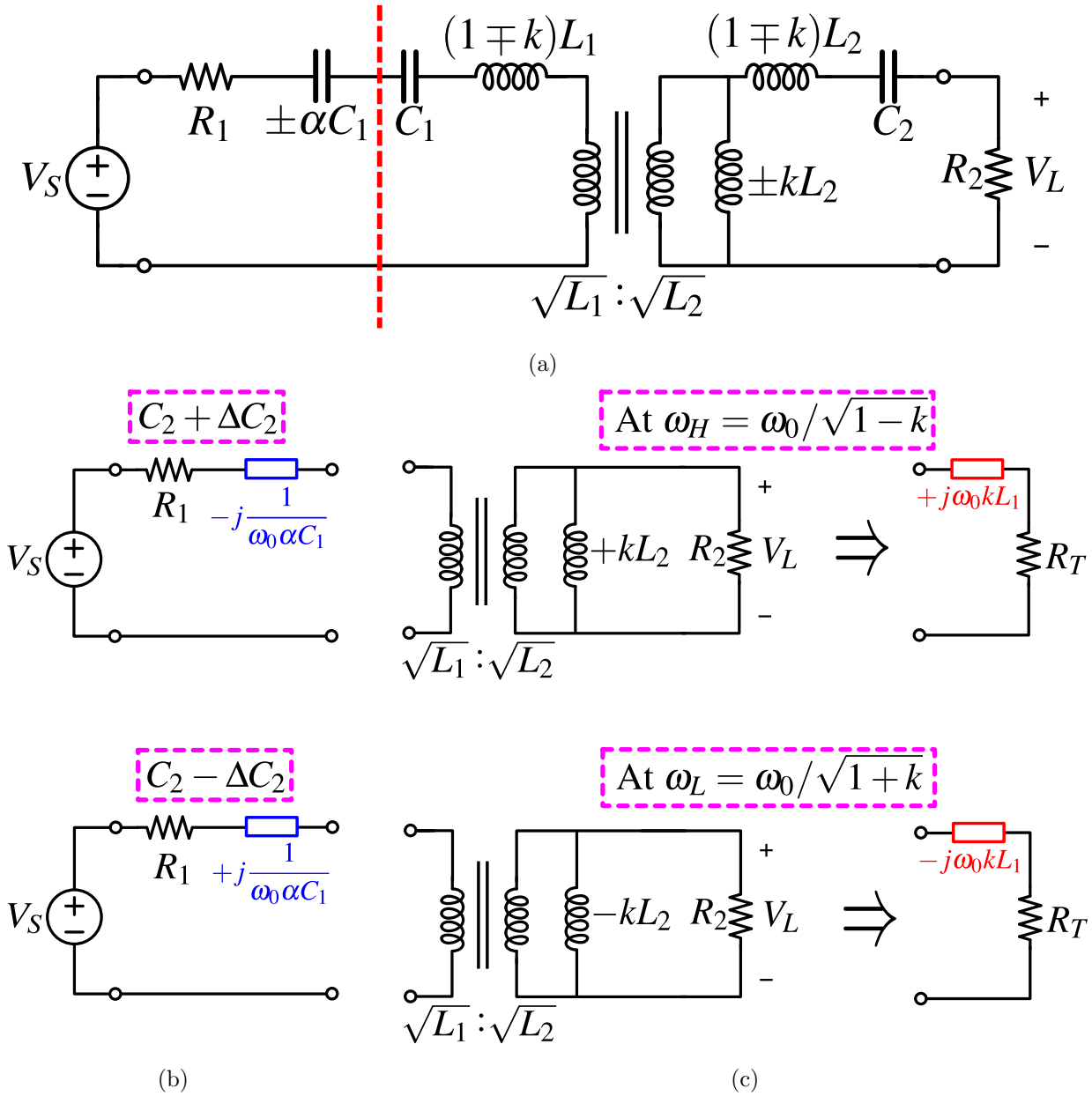

Figure 4.7: (a) The circuit for when a ΔC_1 is added or subtracted to C_1 (equivalent to when a ΔC_2 is subtracted or added to C_2). (b) The equivalent reactance for the left part to the dividing red dashed line in (a) for both the $+\Delta C_2$ and $-\Delta C_2$ cases. (c) The equivalent reactance for the right part for when the system is driven at ω_H or ω_L.

in or out, there appears a positive or negative capacitance $\pm\alpha C_1$, with a negative or positive reactance. Figure 4.7(c) indicates that in the right part of the circuit, depending on whether

the system operates at ω_H or ω_L, there would appear to be a positive or negative inductance in parallel $\pm kL_2$, but independent of frequency, C_1 and $\sqrt{1 \mp k} \cdot L_1$ resonate; C_2 and $\sqrt{1 \mp k} \cdot L_2$ also resonate. When seeing from the left side of the transformer and after performing a parallel-to-series transformation, at ω_H, the right part appears to have a positive reactance, and at ω_L it has a negative reactance.

k is on the order of ~ 0.1, and since $\Delta C_2 \ll C_2$, we can assume $\alpha \sim 10$. Then, both $1/(\omega_0 \alpha C_1)$ from left and $\omega_0 k L_1$ are of the same order. Now, when ΔC_2 is switched in $(C_2 + \Delta C_2)$, the reactances can almost cancel at ω_2 but reinforce each other at ω_L. This means that at ω_H, the oscillator will see a purely resistive system, composed of R_1 and R_T, but at ω_L, the oscillator will see $(R_1 + R_T)$ plus an additional reactance, which raises attenuation to the output. In practice, the oscillation will deviate from $\omega_{L,H}$ so that the input admittance can have exactly zero phase, but it still has higher gain at $\sim \omega_H$ than at $\sim \omega_L$ (equivalently, its dual for parallel coupled resonators shown in Fig. 4.5(a)). Similarly, when ΔC_2 is switched out, the reactances can cancel at $\sim \omega_L$ and oscillation at $\sim \omega_L$ can

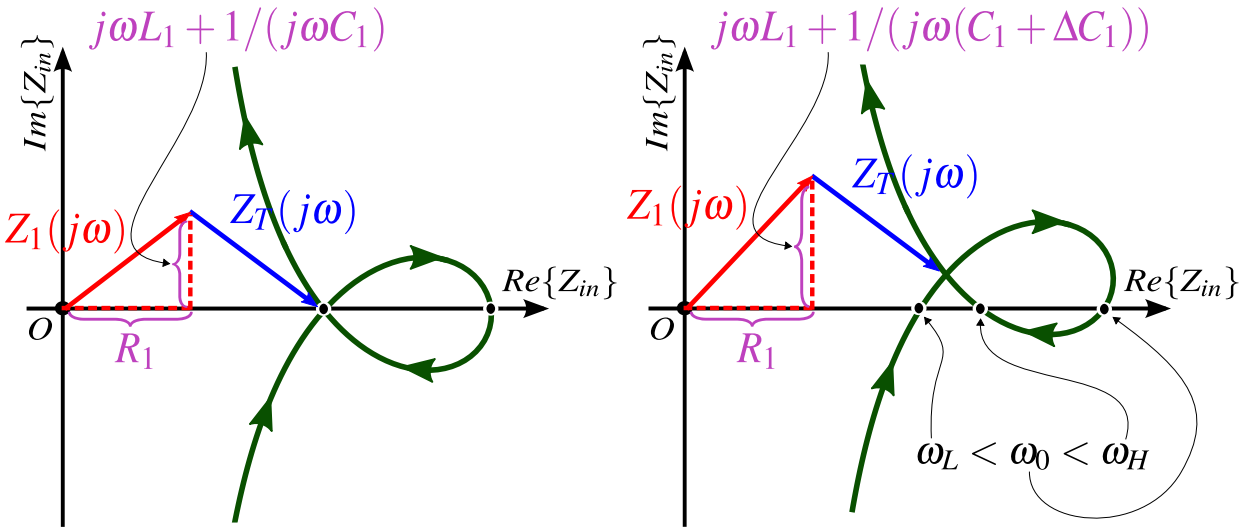

Figure 4.8: Impedance loci plots. (a) shows that with perfect symmetry, resistance at ω_L or ω_H are equal to each other. (b) shows that a slight asymmetry due to ΔC_1 can vertically shift the entire impedance locus, resulting in non-equal resistance for Z_{in} at ω_L or ω_H.

prevail in this case (dual shown in Fig. 4.5(b)).

A different perspective to understand this would be to look at the impedance loci that is first introduced in Chapter 2. In Fig. 2.17 and the accompanying explanations, it was proven that a change in R_1 only results in a horizontal shift in impedance loci without disturbing other parts. That leads to the subsequent proof that Theory II is simply a special case of Theory I and both are tightly linked together.

Now, rather than focus on the horizontal shift, let's think in the orthogonal way.

In Fig. 4.8(a), it shows that with perfect symmetry, the input impedance becomes purely resistive at three frequencies: ω_L, ω_0, and ω_H, as discussed before. The resistance value at either ω_L or ω_H is the same.

Now, assume there is a slight mis-tuning caused by an extra ΔC_1 added to C_1, which causes $1/\sqrt{L_1C_1} < 1/\sqrt{L_2C_2}$ (equivalent to holding C_1 constant and subtract a ΔC_2 from C_2). As shown in Fig. 4.8(b), with everything else staying the same, only the imaginary part of $Z_1(j\omega)$ is affected, and in this case, it becomes longer so that the impedance loci is equivalently shifted up. Therefore, the source sees a lower resistance at ω_L as compared with that at ω_H. Similarly, if a ΔC_1 is subtracted from C_1 (again, equivalent to adding a ΔC_2 to C_2), the opposite case happens: impedance loci will be shifted down so that resistance at

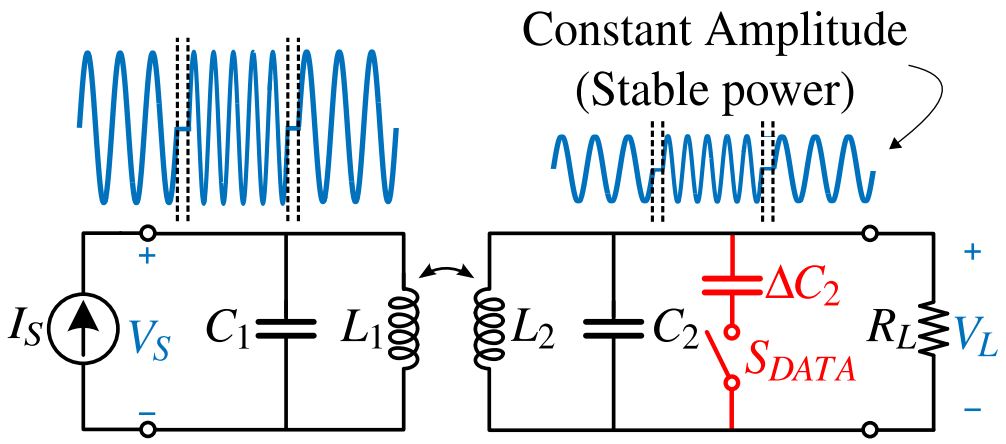

Figure 4.9: Load-Induced Resonance-Shift Keying (L-RSK) modulates frequency and preserves constant amplitude.

ω_H becomes the smallest one.

4.3 Load-Induced Resonance-Shift Keying (L-RSK)

It was discussed before that the commonly used Load-Shift Keying (LSK) is not feasible here (Fig. 4.1), because the amplitude is not stable. What's needed is a *constant-envelope* modulation (Fig. 4.9). By exploiting a unique feature of the system that has been described previously, a new data modulation: Load-Induced Resonance-Shift Keying (L-RSK) will be introduced in this section.

To modulate the frequency, the system adds/removes a $\Delta C_2 \approx 0.05 C_2$ at the secondary side, forcing oscillation at one of the resonant frequencies, ω_H or ω_L, based on the bit to be transmitted (Fig. 4.10). This is called "Load-Induced Resonance-Shift Keying" (L-RSK).

At the beginning of each bit period, the existing oscillation is quenched quickly (within one cycle) with critical damping resistors $R_{DAMP,TX}$ and $R_{DAMP,RX}$. Then, depending on the data bit, S_{DATA} turns ON or OFF. The critical damping resistors are released, and the oscillator starts up at the selected frequency. Data is transmitted by shifting a constant amplitude power carrier between the two frequencies $\omega_{L,H}$ so that wireless power is delivered to the implant smoothly and continuously. This modulation is a form of binary frequency-

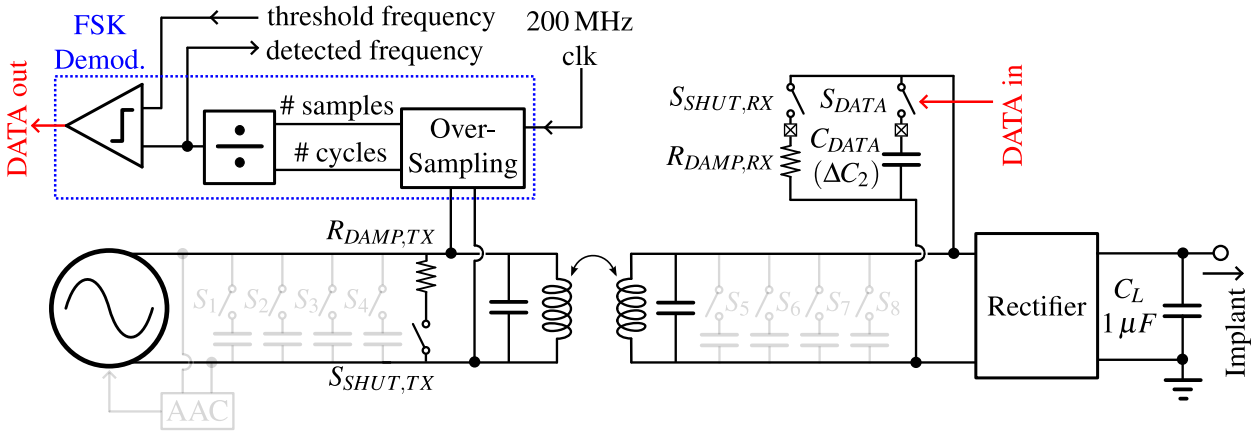

Figure 4.10: The circuits for reverse data communication on top of the existing wireless power transfer circuits.

shift keying (FSK).

In each bit period, an all-digital FSK demodulator senses the oscillation from the primary side, over-samples it using a clock of up to 200 MHz, and then divides the total number of samples by the total number of cycles to compute an estimate of the oscillation frequency. The estimated frequency is compared with a threshold value (ideally ω_0 around which ω_L and ω_H split) to demodulate whether bit '0' or '1' is sent.

In practice, the split frequencies $\omega_{L,H}$ do not branch symmetrically around the center ω_0 (Fig. 4.11). Instead, the threshold frequency itself changes with distance. This is not just because $\omega_0/\sqrt{1-k}$ and $\omega_0/\sqrt{1+k}$ are neither algebraically nor geometrically symmetric around ω_0, but also because the parasitic capacitance contributed by on-chip components may vary. Therefore, for successful demodulation, before data bits are transmitted, a preamble of 010101... is sent. The FSK demodulator can detect the actual frequencies corresponding to the two bits, and use their average value as the optimal demodulating threshold. The load capacitor $C_L = 1\,\mu$F at the output of rectifier can ensure an almost constant voltage

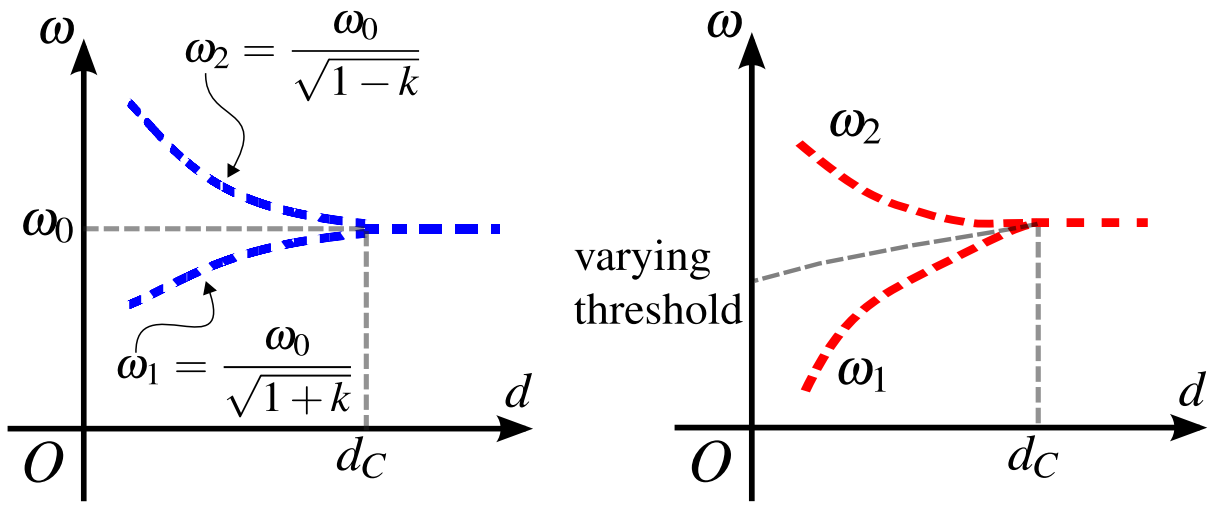

Figure 4.11: (a) Theoretically, ω_0 may be used as the threshold frequency for demodulation. (b) During actual operation, the optimal demodulation threshold may vary as a function of distance.

supply to the implant, with ¡1 mV droop during the oscillation quenching.

In practice, it is difficult to build a digital arithmetic divider. Instead, a multiplier is implemented that takes the product of a threshold value and the number of cycles, and compares this with the number of samples. This effectively performs a division.

To summarize the advantages of this modulation:

1. It switches a *tiny* ΔC_2 ($\sim 5\%$ of C_2) to create a slight mis-tuning. This ensures that the power delivery at either ω_L or ω_H doesn't differ very much. Therefore, *regulated* power that is immune to both distance and load variations can still be delivered *simultaneously* with reverse data flow.

2. Although the mis-tuning is tiny, the difference between the two frequencies is easily distinguishable especially when the coupling is strong. This makes the data demodulation easy.

3. The total power required for data modulation is that of driving the FET switches.

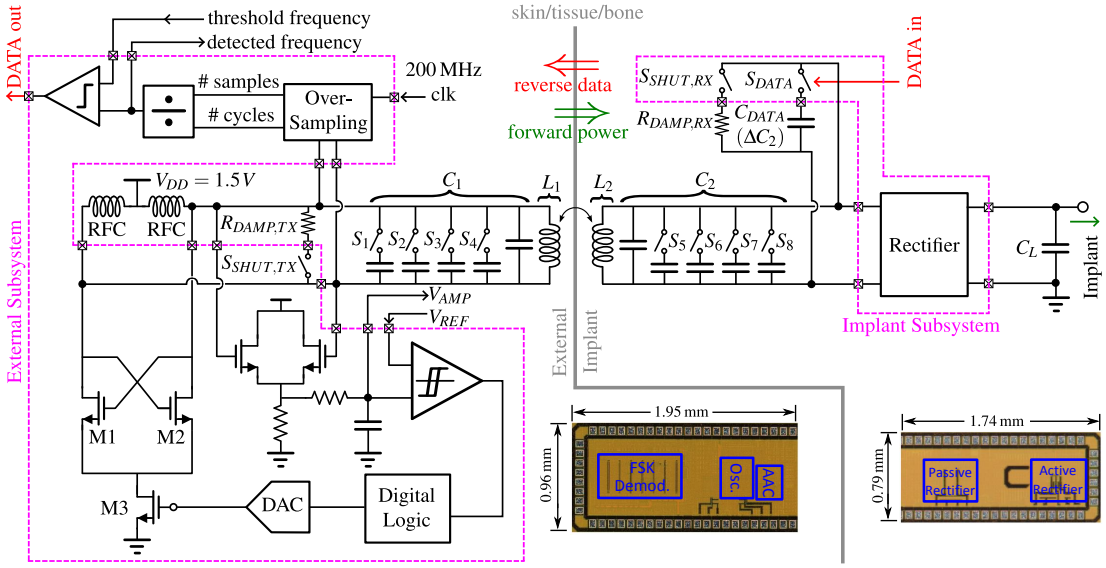

Figure 4.12: The full schematic of the entire system, associated with the corresponding die photos.

4.4 System Implementation

Figure 4.12 shows the full schematics of the system comprising both wireless power and wireless data circuits. The system is integrated on two separate chips using 180 nm CMOS. The external subsystem that consists of the wireless power transmitter and data demodulator is implemented on one chip, occupying 1.95×0.96 mm; the implant subsystem composed of wireless power receiver and data modulator is implemented on another one of 1.74×0.79 mm.

When mounting the chip on printed circuit boards (PCB), it is very important to be aware that unwanted oscillation is possible, and to take appropriate precautions. As shown in Fig. 4.13, in addition to the off-chip capacitors C_1 and coil inductor L_1 on the primary side, the bond pads and large FETs M1,M2 all contribute parasitic capacitance C_{par}, and the bond wires and PCB traces contribute parasitic inductance L_{par}. Normally, these parasitics have no influence other than shifting the original resonant frequency $\omega_0 = 1/\sqrt{L_1 C_1}$ by a little bit. However, when at the start of data communication, oscillation is first quenched with the damping resistor $R_{DAMP,TX}$ that, in effect, shorts C_1 and L_1, the resonator C_{par} and L_{par} can induce oscillation at

$$\omega_{unwanted} = \frac{1}{\sqrt{L_{par} C_{par}}}. \tag{4.1}$$

Since L_{par} is 1∼10 nH and C_{par} is 1∼10 pF, $\omega_{unwanted}$ can be $\gg \omega_0$, sometimes close to 1 GHz. When $S_{SHUT,TX}$ is released, C_1 presents its effective series resistance (R_{C1}) at $\omega_{unwanted}$ and this high frequency oscillation can start up and persist indefinitely, irrespective of switching.

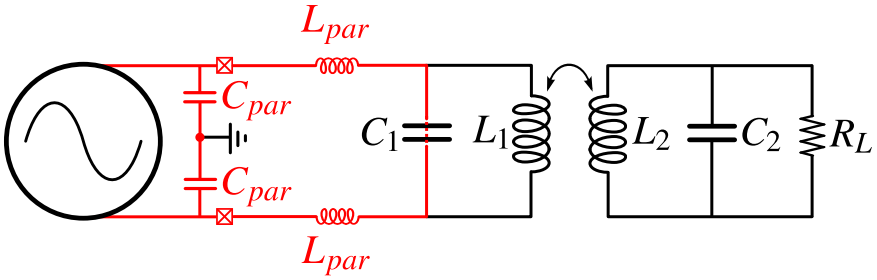

Figure 4.13: An equivalent circuit illustrating the unwanted oscillation mode formed by parasitic capacitance and parasitic inductance.

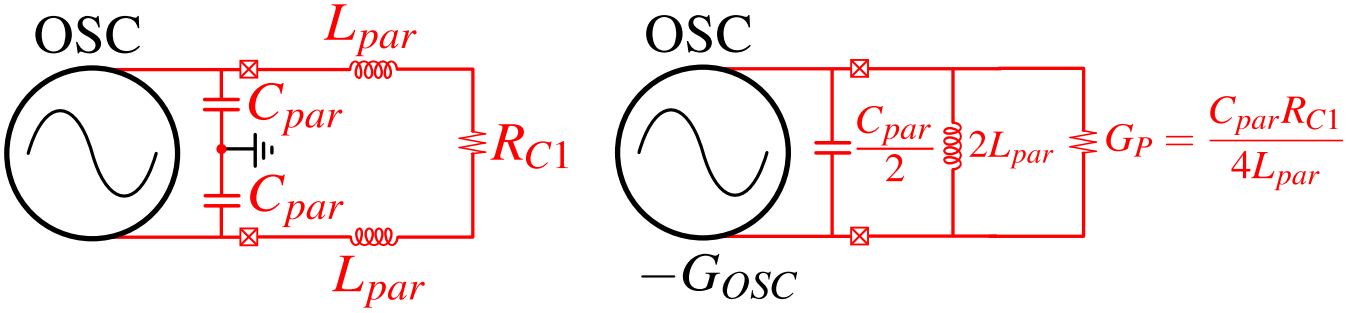

(a) (b)

Figure 4.14: (a) At high frequency ($\omega_{unwanted}$), C_1 acts as a effective series resistance R_{C1}. (b) After performing a series-to-parallel transformation of L_{par} and R_{C1}, there now exists a parallel conductance G_P that is inverse proportional to L_{par}. The smaller L_{par} gets, the larger G_P can be. When $G_P > G_{OSC}$, the oscillator loses the ability to ever start up at $\omega_{unwanted}$.

It squelches all the intended oscillation modes, disabling the system entirely.

This can be avoided by using very short PCB traces and bond wires, lowering L_{par} to <1 nH. The quality factor for the parasitic tank $Q_{par} = 2\sqrt{L_{par}/C_{par}}/R_{C1}$, is now lowered, presenting effectively a large shunt conductance (G_P) across the oscillator driver. When this conductance is large enough ($G_P > G_{OSC}$), it cannot be overcome by the fixed negative conductance of the cross-coupled differential pair and oscillation at $\omega_{unwanted}$ is suppressed.

Figure 4.15 shows the actual implemented system (chips + PCBs).

4.5 Measured Performance

Figure 4.16 shows the actual measured waveforms of the system operating at around 13.56 MHz and transmitting reverse data at 1 Mb/s. The single-ended oscillator output voltage indicates that the oscillation experiences short-time quenching within each bit period. The rectifier output voltage remains a constant value at around 2.2 V, simultaneously with the reverse data flow regardless of what bit is sent.

Figure 4.17 shows measured waveforms when the system operates at around 30 MHz

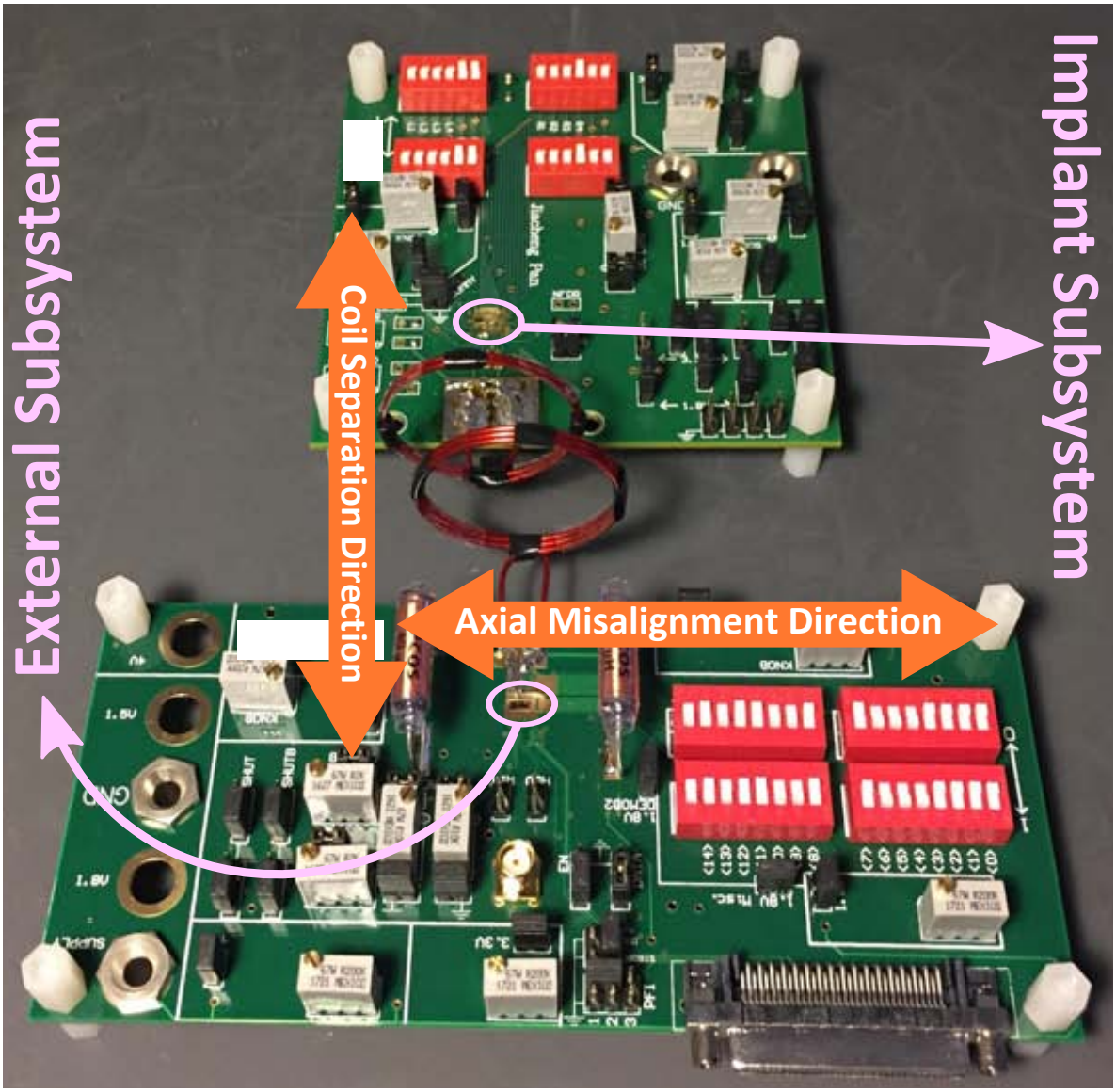

Figure 4.15: A photo of the test-bench, showing the chips, PCBs, and coils. The coil separation direction and axial misalignment direction shown on the graph correspond to the previous measurements of wireless power performance in Chapter 3.

center frequency and transmits reverse data at 4 Mb/s, largely beyond what was required by the brain implant mentioned in Chapter 1. The differential oscillation waveform clearly shows that the oscillation quenching time is around 10% of each bit period. Data is successfully demodulated by sensing the frequency difference (here, the two frequencies are 27 MHz and 31 MHz), while at the same time, rectifier output voltage remains largely constant and

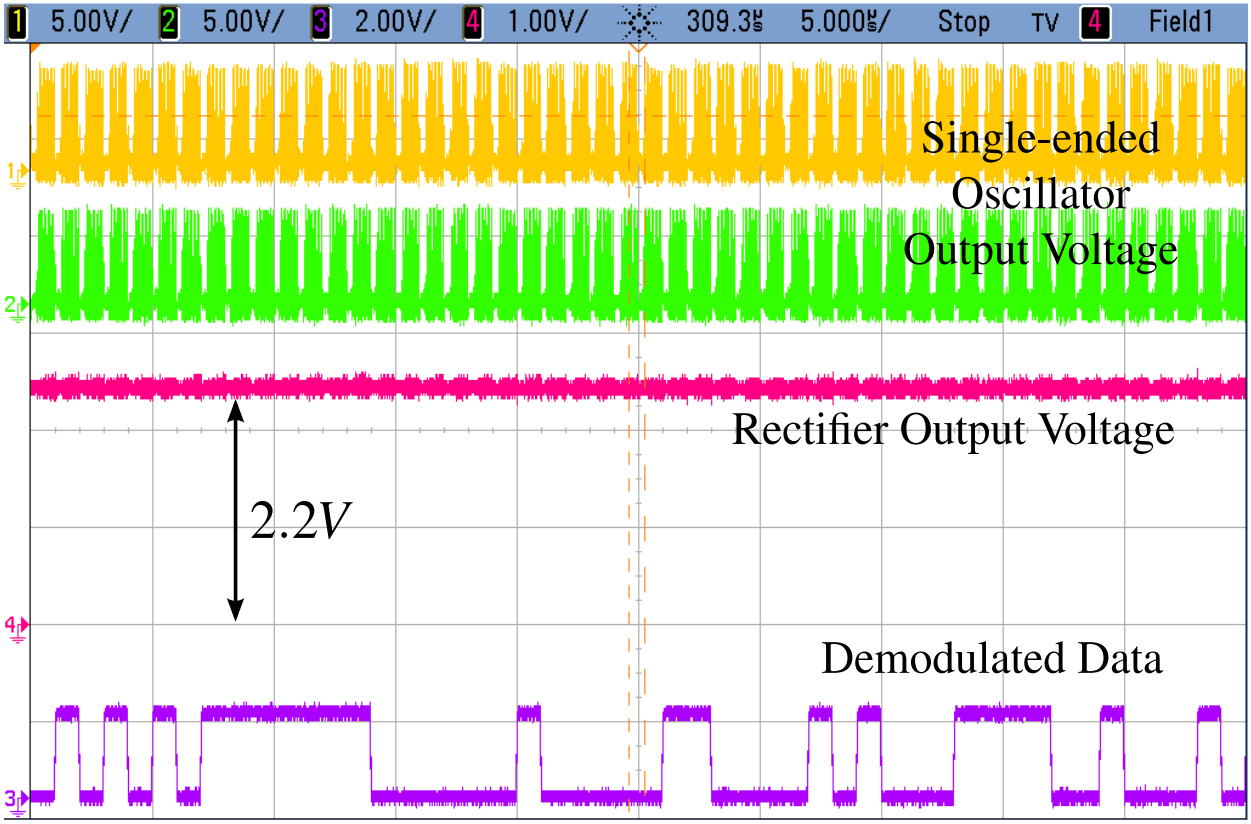

Figure 4.16: Measured waveforms when system operates at around 13 MHz. Reverse data is transmitteda at 1Mb/s, what's required by the brain implant of this work (Chapter 1). The supply to the implant which is the rectifier output voltage shown in the figure remains a constant value at 2.2 V simultaneously with the data flow.

regulated.

Figure 4.18 shows measured waveforms when the system operates at around 30 MHz center frequency and transmits reverse data at 5 Mb/s, the extreme case for the data communication of this system. This can only happen at a very limited coil separation (∼0.8 cm, roughly the average thickness of the human skull), whereas the other two cases, as will be shown later, can span a large coil separation range.

For the wireless data bit error rate testing, pseudo-random binary sequence PRBS-7 was used. Measurements indicate that the system can support reliable data communication up to 2 cm at 1 Mb/s using 13.56 MHz center frequency, and at 4 Mb/s using around 30 MHz

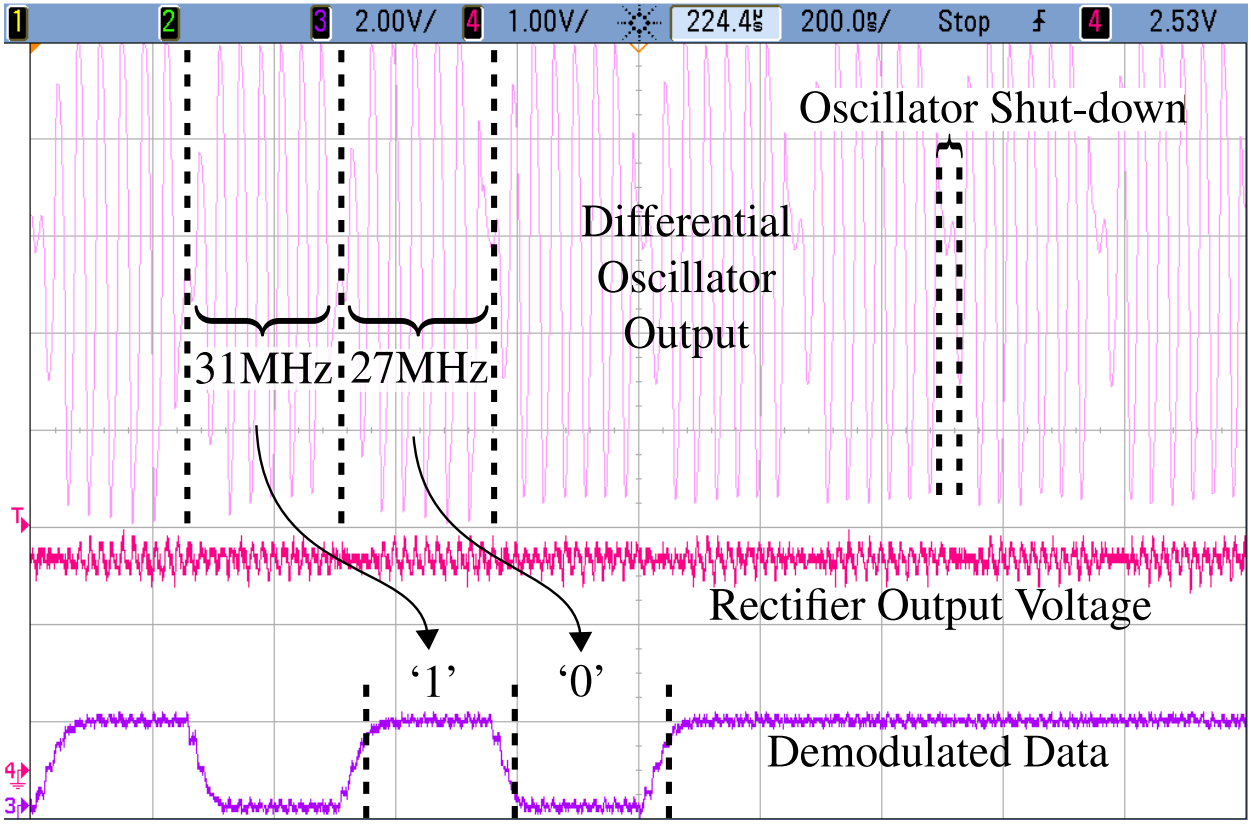

Figure 4.17: Measured waveforms when system operates at around 30 MHz. Reverse data is transmitted at 4Mb/s. Oscillation is quenched for ∼10% of each bit period. For this measurement, oscillator selects between 31 MHz and 27 MHz to send data bit '1' or '0'. Again, supply to the implant remains constant simultaneously with the reverse data flow.

center frequency (Fig. 4.19). The all-digital FSK demodulator, when working at 200 MHz, consumes 6.8 mW.

During operation, the free-running oscillator self-tunes its frequency to adapt to change in distance. This can run afoul of FCC rules. FCC §15.209 specifies that for unlicensed transmission in the frequency range 1.705 MHz − 30.0 MHz, the radiation measured at 30 meters away should stay below 30 µV/m. The measurement was set up in antenna chamber using a dipole antenna of 1.35 m length with receiver. Measurement (Fig. 4.20) shows that in the worst case, at 13.56 MHz, system's radiation will be below the FCC limit.

In Table I, this system's performance is compared with that of other state-of-the-art

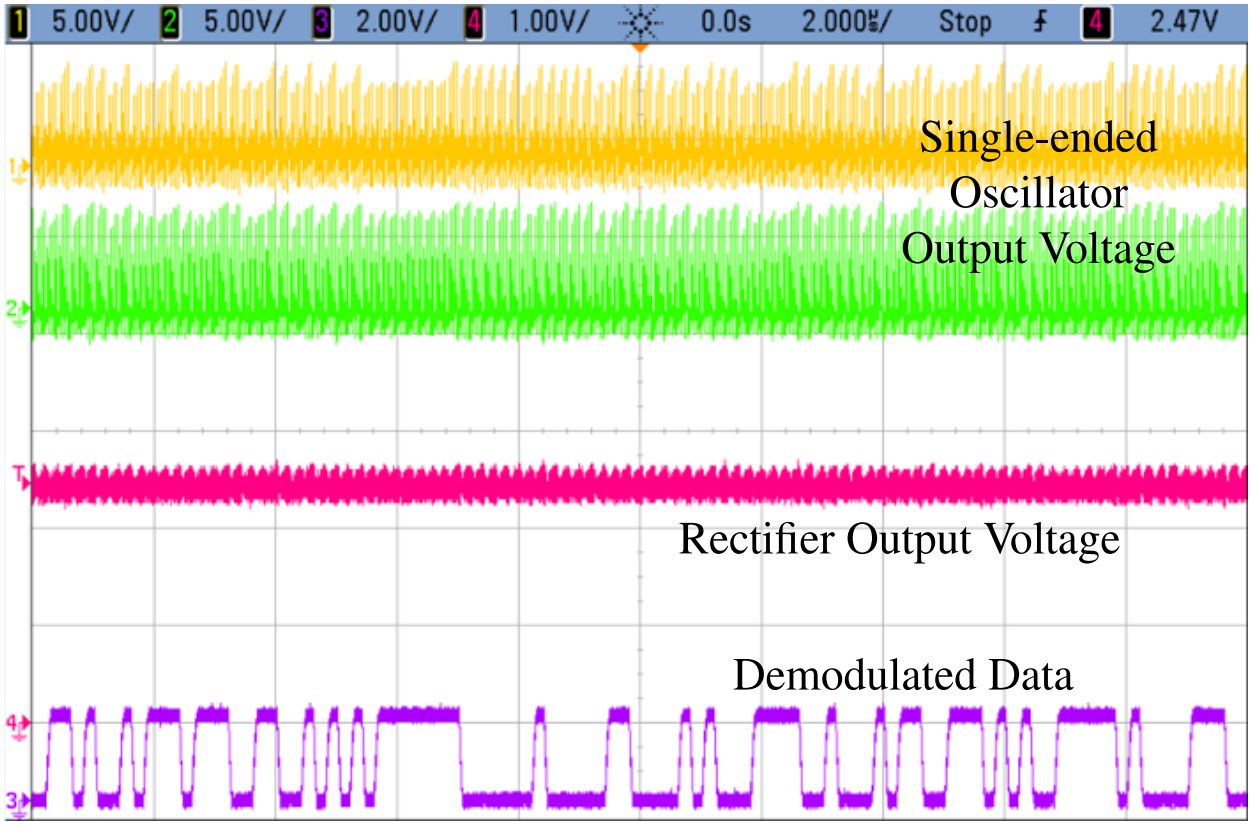

Figure 4.18: Measured waveforms when system operates at around 30 MHz. Reverse data is transmitted at 5Mb/s.

systems. To the left of this work in the table are wireless power systems with no data link. Compared with them, this system has the largest maximum normalized regulation distance and handles the biggest load variations. It also has the best peak efficiency. To the right of this work are systems of dedicated data links, with unregulated wireless power or no wireless power at all. This system achieves comparable performance in terms of data rate and bit error rate. It burns at most 0.395 mW for data modulation. This modulator's dissipation is larger than [37], for example, because to handle power signals, the data switches in this system use I/O devices with 350 nm channel length. The width of the FETs involved in the switches must be scaled to critically damp a power carrier. Compared with others which use 65 nm or 40 nm technology, this largely increases modulation power because the total power required for driving a switch $\propto C \cdot V^2$ where $C \propto W \cdot L$. However, compared with the

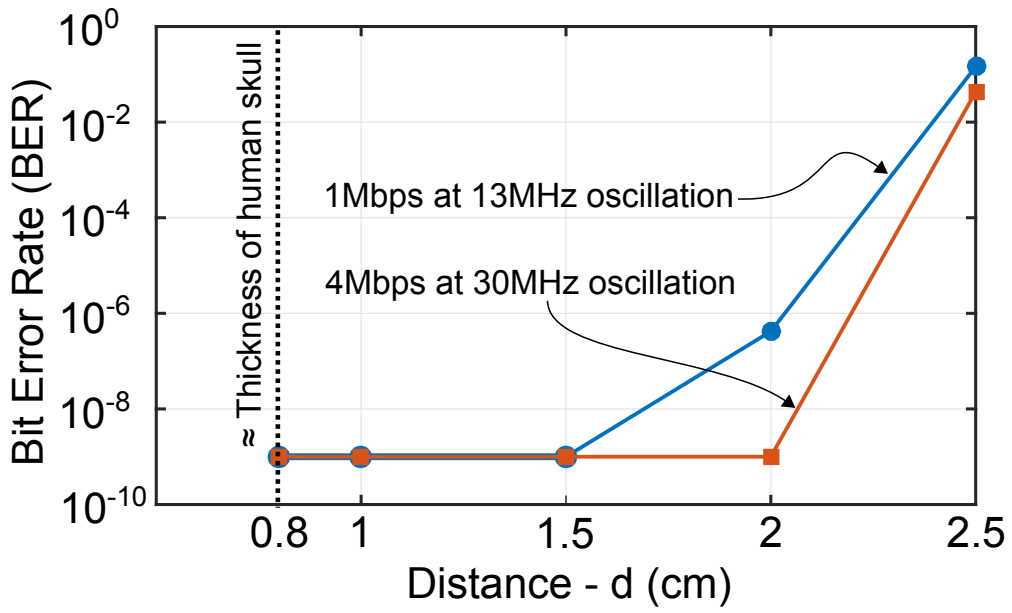

Figure 4.19: Measured bit error rate for different distances starting at 0.8 cm, roughly the thickness of human skull.

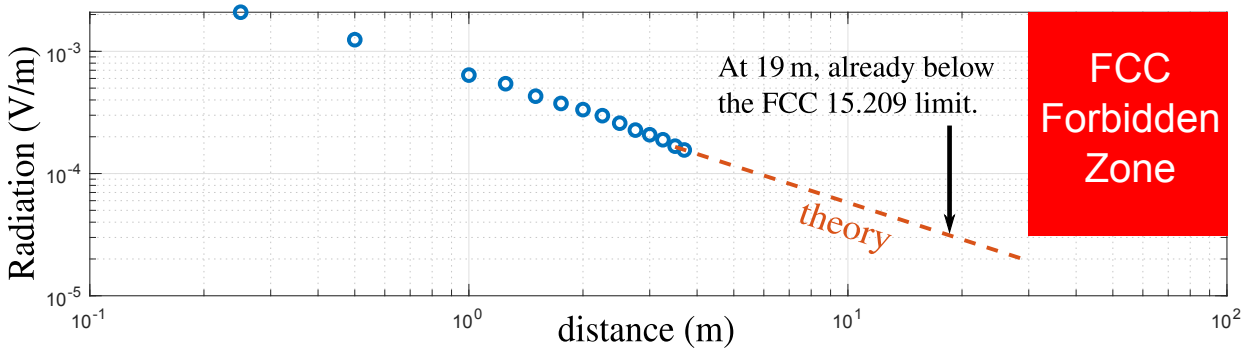

Figure 4.20: Measured radiation strength at different distances showing that our system complies with the FCC §15.209 regulation.

total power that is delivered to the implant's load, the power consumed to modulate data is negligible.

This is a self-regulating wireless power delivery system for brain implants that exploits some unique physical properties of magnetically coupled resonators. An intuitively clear design-oriented analysis has led to the first practical 100 mW delivery system that self-regulates load voltage across distances up to 4.2 cm using coils with diameter of 3 cm. It also

Table 4.1: Performance Comparison

Reference	[29]	[26]	[21]	[35]	This work	[43]	[40]	[38]	[39]	[37]
Max. load var.¶	4.4×	22×	9×	9×	40×	Unregulated Wireless Power				No Wireless Power
Norm. max. load var.	0.57	0.55	0.23	1.4	1.4					
Max. reg. dist.¶ (cm)	3.4	1.2	0.6	4.2	4.2					
Efficiency	53%	62.4%	70.6%	73.7%	80.1%					
Power (mW)	1450	234	49.4	20	93.8	11.5	15	-	0.8	
Coil Diam. TX/RX (cm)	9/4	5/0.95	3.44/2	3/3	3/3	6.5/4.2	3/2	-/1.35	1.5/0.65	3/3
Simult. reg. power & data	No	No	No	No	Yes	No	No	No	No	No
Number of pair of coils	1	1	1	1	1	1	1	2	2	1
Technology (nm)	350	350	65	180	180	65	180	180	65	40
Modulation	No Wireless Data				L-RSK	COOK	LSK	LSK	LSK	LSK
Data rate (Mb/s)					5	6.78	2	2	1	4
Bit error rate					4.2×10^{-7}	1×10^{-7}	4.8×10^{-4}	1×10^{-3}	1.7×10^{-7}	5×10^{-8}
Data TX power (mW)					0.395	0.064	-	-	-	0.0004

¶ Maximum range under a reasonable efficiency ($> 35\%$).

regulates against load resistance changes of 40×.

An innovative method to transmit data in the reverse channel has been devised, that exploits mode selection in oscillators as a form of wideband FSK on the power carrier. Rates up to 5 Mb/s have been achieved over the same two coils that carry power. There is no discernible ripple on the received power as data is sent. This is enabled by the newly proposed data modulation: Load-Induced Resonance-Shift Keying (L-RSK).

Besides a robust wireless power and data system for biomedical implants, it is also of great interest to see if the same idea can be applied to other applications. Wireless charging for consumer electronics seems to be a good and tangible candidate that is close to commercialization. In the next chapter, it will be shown that the design methodology on wireless

power is robust enough to be scaled up to cover Watt-level applications.

CHAPTER 5

A General Design Methodology for Wireless Power: Scaling it up to Watt-Level Applications

5.1 Prior Arts

For wireless charging portable electronics, there have been many researches targeting a robust wireless charging system. With some of the techniques already discussed in section 1 of Chapter 3, there are a few that are worth mentioning as they target different aspects of the application: [45] discussed a battery-charger IC that can be used by multiple different wireless power transfer standards, including Qi, PMA, and A4WP. It is targeting wearable applications. [46] proposed a wireless power system that allows bidirectional charging, aiming at applications such as charging between smartphones, etc.

This work aims at a robust wireless charging system that can provide power to portable electronics, even in a dynamic environment where the distance or alignment between the chargable device and charging transmitter is not fixed and may vary frequently. After the discussion of design methodology in the next section, the robustness of the methodology will be illustrated using an example design that scales the original mW-level power for biomedical implants to Watt-level power for portable electronics.

5.2 General Design Methodology

The design of a wireless power transfer system often focuses on three aspects: the delivered load power (P_L), the maximum operating distance (d_C), and the power transfer efficiency

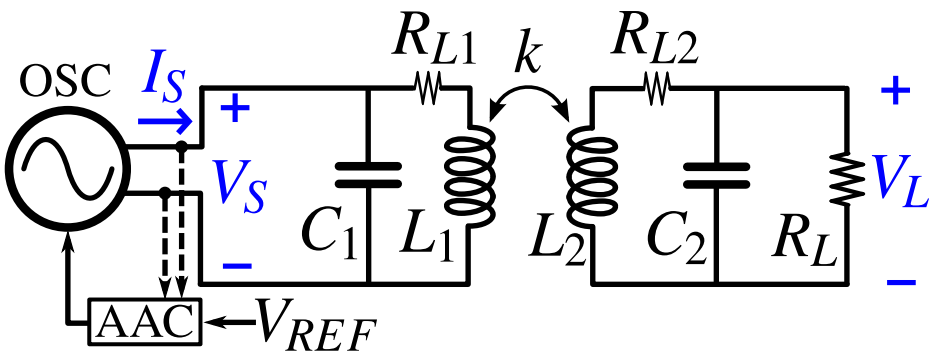

Figure 5.1: Simplified schematics for the wireless power system in Chapter 3, with parallel LC coupled resonators as the link.

(η). Now, the various trade-offs among the three quantities will be discussed to guide on how to make design choices. The system of parallel LC coupled resonators discussed previously (Fig. 5.1) will be used as an example.

- The maximum operating distance d_C is related to the minimum operating coupling k_C, determined by

$$\boxed{k_C = \frac{1}{Q_2} = \frac{\omega_0 L_2}{R_L}.} \tag{5.1}$$

  The smaller the critical coupling coefficient k_C is, the larger the d_C is.

- The delivered load power $P_L = (V_L)^2/(2R_L)$. Since (2.46) holds for when the system operates within the maximum distance ($k > k_C$). P_L can be rewritten as:

$$\boxed{P_L = \frac{L_2}{L_1}\frac{V_S^2}{2R_L}.} \tag{5.2}$$

- During the wireless power transfer, it suffers from loss in three stages: the loss in power conversion of the source driver, the loss in the coupled resonators link, and the loss incurred at the power receiver. Therefore, the total power transfer efficiency is:

$$\boxed{\eta = \eta_{TX} \times \eta_{link} \times \eta_{RX} = \eta_{TX} \times \frac{Q_1}{Q_1 + Q_2} \times \eta_{RX}.} \tag{5.3}$$

  Q_1 is the quality factor of transmitter coil, Q_2 is the loaded quality factor of the receiver coil given by $Q_2 \approx R_2/(\omega_0 L_2)$, assuming R_L's influence dominates over the

self-resistance of the secondary coil. η_{TX} accounts for the loss of power during DC-AC conversion at the driver and η_{RX} accounts for the power loss in secondary coil, and in power reception circuits.

With the help of these key equations, a detailed example will be used to illustrate the trade-offs and design strategies.

5.3 Example: Scaling up from milli-Watt to Watt

The system described in Chapter 3 targets a biomedical implant and supplies up to $<$ 100 mW power. Consider a new system that targets portable electronics, such as smart phones which requires $>$ 5 W to be delivered to the load. With the big structure shown in Fig. 5.1, a typical receiver for such systems follows a structure shown in Fig. 5.2 (in Fig. 5.1 it's lumped as R_L). A rectifier first converts the received AC V_L into a DC value, followed by a DC-DC converter which then regulates the voltage to be 5 V so that it could be used by the battery charging circuits. If the battery charger operates at 5 W, its equivalent input resistance is 5 V/1 A = 5 Ω. The resistance looking at the input port of DC-DC converter will be scaled by n^2. Since the rectifier is connected to a parallel LC resonator, and assume the rectified output DC voltage is equal to the magnitude of input AC voltage. The following

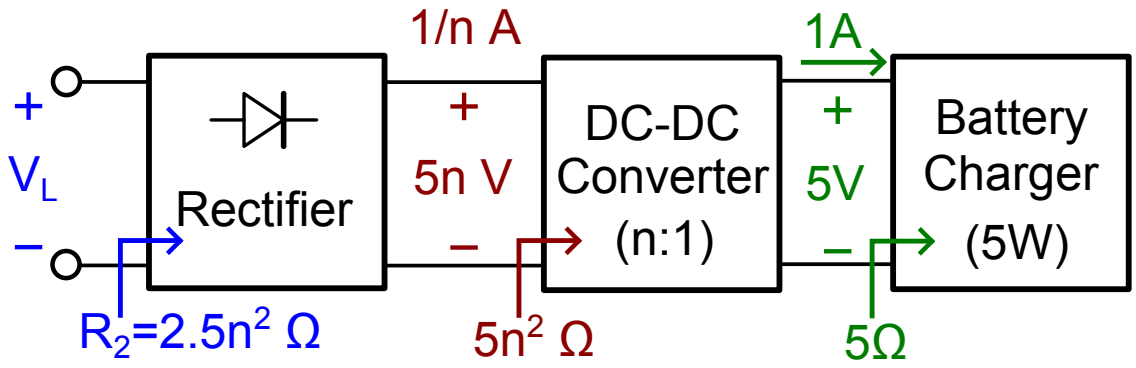

Figure 5.2: The receiver circuits for Watt-level applications are usually composed of a rectifier, a DC-DC converter, and a battery charger.

relation holds:

$$\frac{\cancel{|V_{AC}|^2}}{2R_{in,rec}} = \frac{\cancel{V_{DC}^2}}{R_{out,rec}} \quad \Rightarrow \quad R_{in,rec} = \frac{R_{out,rec}}{2}. \tag{5.4}$$

Therefore, $R_2 = 2.5n^2\,\Omega$. Note that this doesn't take into account of power loss in the entire conversion process. If the total efficiency is η_{CONV}, then the equivalent input resistance at the rectifier should be scaled accordingly $= \eta_{CONV} \cdot R_2$.

For ease of analysis, assume $\eta_{CONV} \approx 1$. We start by setting $n = 1$ for the DC-DC converter.

1. For symmetry consideration, suppose $L_1 = L_2$, then (5.2) indicates that $V_S = 5V$.

2. A rule of thumb equation for approximating the coupling coefficient between two circular coils is the Roz and Fuentes' formula [47]

$$k \approx \frac{r_{TX}^2 r_{RX}^2}{\sqrt{r_{TX} r_{RX}} \cdot (\sqrt{d^2 + r_{TX}^2})^3}, \text{ for } r_{TX} > r_{RX}, \tag{5.5}$$

   where r_{TX} and r_{RX} refers to the radius of the transmitting and receiving coils, and d is the distance inbetween.

   A reasonable dimension would be $\sim 3cm$ radii for both the coils. Plugging them into (5.5), it indicates that to transfer power at a decent distance ($\sim 5cm$), it requires the system to work up to $k \approx 0.136$. Therefore, $k_C = 0.1$ is chosen to allow for some margin.

3. With $k_C = 0.1$ and $R_2 = 2.5\Omega$, (5.1) shows that $\omega_0 L_2$ should be $0.25\,\Omega$.

4. A commonly used standard for wireless power of consumer electronics is the Qi standard, which requires the operating frequency to be $110 \sim 205kHz$ for low-power ($< 5W$) applications, and $80 \sim 300kHz$ for medium-power products. Therefore, $\omega_0 = 150kHz$ is selected to be the center frequency.

5. This results in a $L_2 \approx 265nH$. With $6cm$ diameter, even a 1-turn coil will have higher inductance than this. Moreover, the coil's quality factor will be low if there is not enough number of turns. This means that a significantly increased L_2 is required.

6. From (5.1), since ω_0's range is fixed due to the Qi standard, to tolerate a higher L_2 without affecting operating distance, R_2 should be increased, too. From (5.2), to maintain the same delivered power with an increased R_2, V_S should increase accordingly. As a result, n of the DC-DC converter can be set to 4, so that R_2 increases by $16\times$ to $40\,\Omega$ now. V_S should also be scaled by $4\times$ to $20\,\mathrm{V}$.

7. L_2 can also go up by $16\times$ to $\sim 4\,\mu\mathrm{H}$. L_1 can use the same value. Now both the distance (5.1) and power (5.2) requirements can be satisfied with real-life coils. The next step is to optimize the coil design so that the efficiency in (5.3) can be as high as possible.

8. If in the coil design, optimal L_2 deviates from the value calculated in step (7), then go back to step (1) to fine-tune the value of n and repeat this process.

The design can follow the above listed steps. Additional iterations can be added to successively approach the optimal design.

Note that for this example, the selection of ω_0 is limited to a certain range, primarily due to the range limits from wireless power standards. Now, let's look at applications where ω_0's value is free to choose, and how to optimize the design for such systems.

For most biomedical implants, they require a delivered power on the order of a few mW or tens of mW. In that case, the frequency of operation does not necessarily need to conform to any existing regulations, for the reason that with mW power level, the radiation complies with FCC §15.209 out-of-band radiation emission limits over almost all frequencies below $30MHz$.

Based on the three equations of distance ((5.1)), load power ((5.2)), and efficiency ((5.3)), the following relation with respect to R_2 can be summarized:

$$R_2 \uparrow \quad \Rightarrow \quad \begin{cases} k_C = \dfrac{1}{Q_2} = \dfrac{\omega_0 L_2}{R_2} \downarrow \Rightarrow \ d_C \uparrow ; \\ P_L = \dfrac{L_2}{L_1}\dfrac{V_S^2}{2R_2} \downarrow ; \\ Q_2 = \dfrac{R_2}{\omega_0 L_2} \uparrow \Rightarrow \ \eta \propto \dfrac{Q_1}{Q_1 + Q_2} \downarrow . \end{cases} \tag{5.6}$$

This indicates that the delivered power and efficiency trades off with the maximum operating range. In practice, for a system with center frequency ω_0, when the delivered load power drops because of increases in R_2, the max. operating range will expand, but the efficiency drops. If the max. range d_C expands beyond what's needed, then to improve the power transfer efficiency, the center frequency ω_0 can be set to a higher value, so that:

$$\omega_0 \uparrow \Rightarrow \; Q_2 = \frac{R_2}{\omega_0 L_2} \downarrow \quad \Rightarrow \quad \begin{cases} k_C = \dfrac{1}{Q_2} \uparrow \Rightarrow \; d_C \downarrow ; \\ \eta \propto \dfrac{Q_1}{Q_1 + Q_2} \uparrow . \end{cases} \tag{5.7}$$

Increasing ω_0 as R_2 rises, or vice versa, compensates the changes in max. range and efficiency. However, if change in ω_0 is too large, the coils may need to be redesigned so that their quality factors can be optimized at the new frequency of operations.

Note that these generalized trade-offs are tightly connected with the conclusions shown previously in the fifth section of Chapter 3.

5.4 System Design

Guided by the procedures shown in the previous section, a new wireless charging system was implemented on PCBs (Fig. 5.3). It was implemented with components listed in Table II.

Table 5.1: System Parameters

Parameter	Notes
Diodes	SL02-GS08CT-ND
RFC	M8878-ND
$M1$ and $M2$	SI4178DY-T1-GE3CT-ND NMOD
$M3$	BCW66KHE6327HTSA1CT-ND BJT

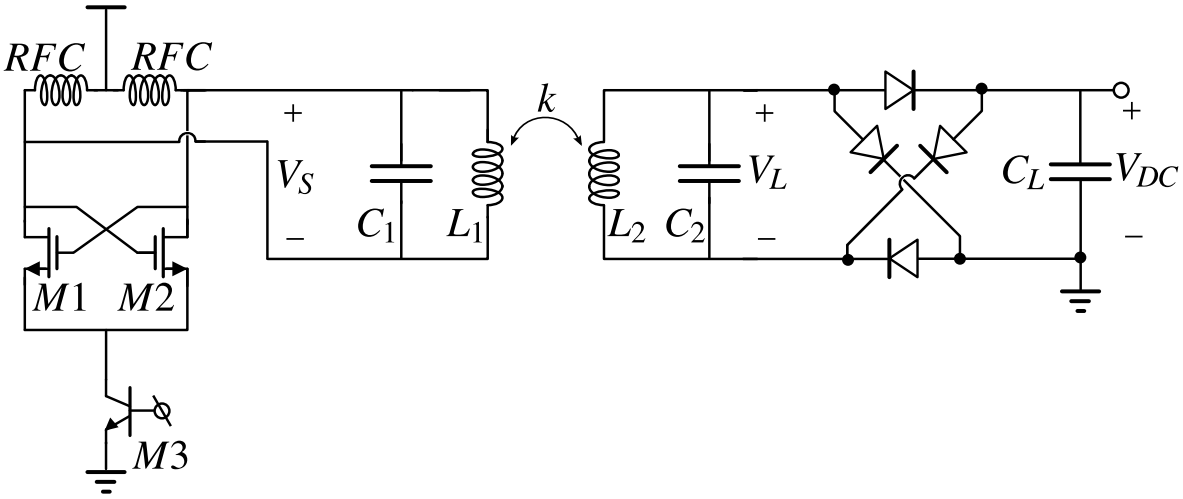

Figure 5.3: The actual implemented wireless charging system that, as will be shown, can provide more than 10 W of power, regulated against changes in devices' separation.

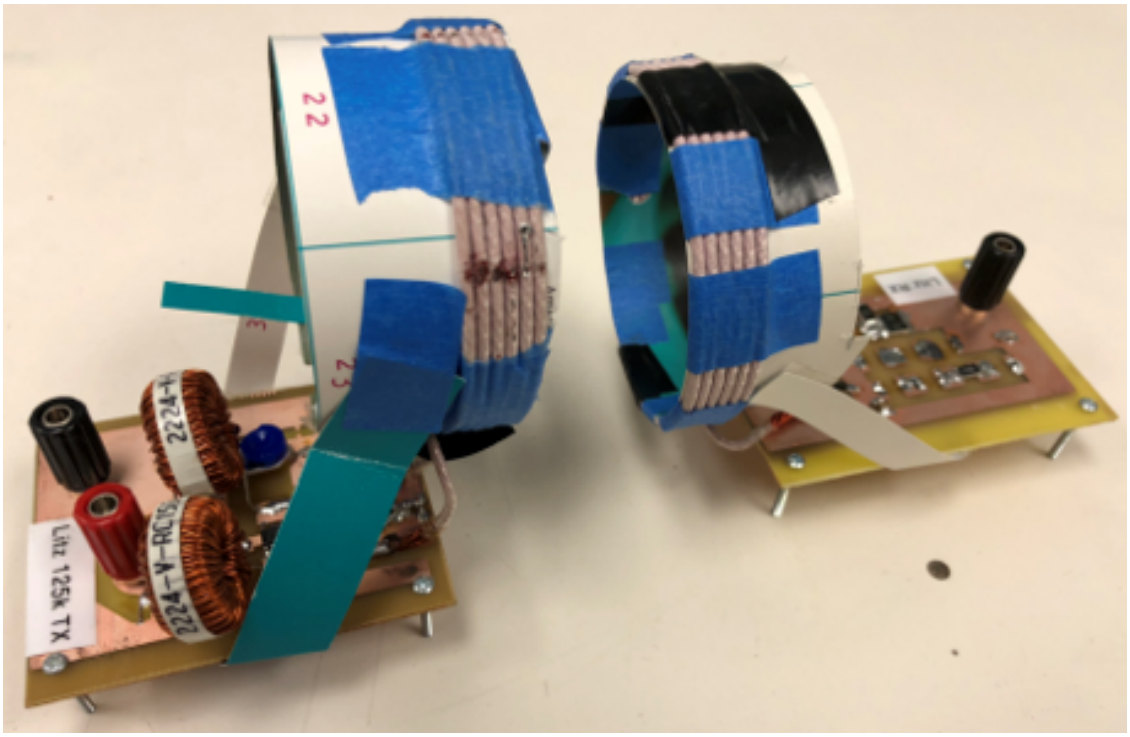

Figure 5.4: Version 1 of the tested systems. Coils are hand-wound (6 turns) using Litz wires with 6.8 cm diameters.

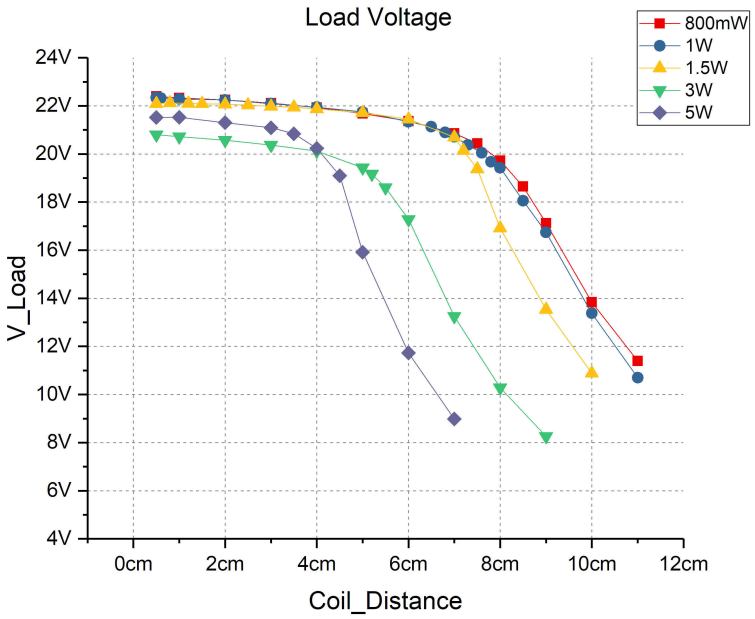

Figure 5.5: Measured delivered voltage vs. distance for version 1.

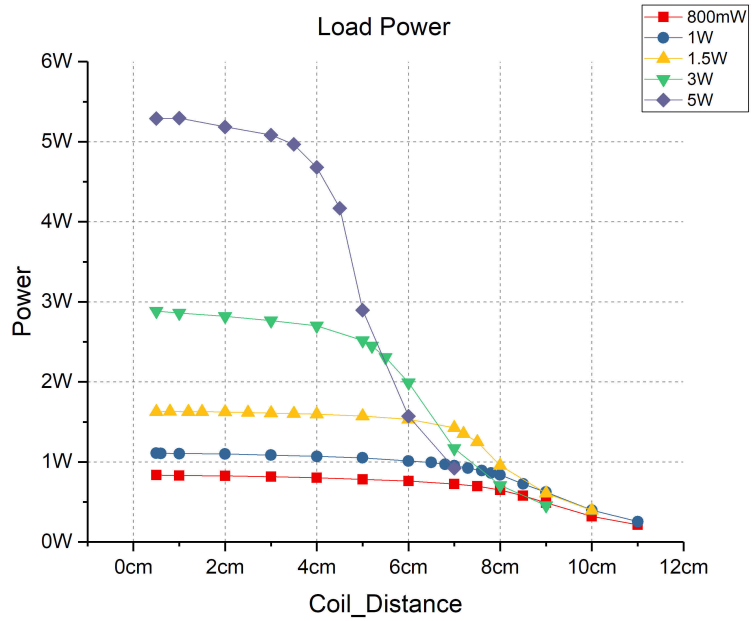

Figure 5.6: Measured delivered load power vs. distance for version 1.

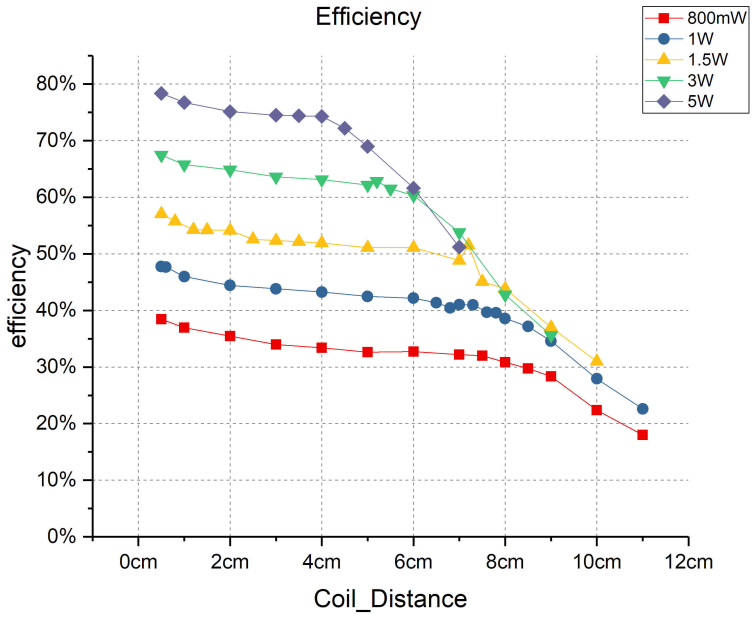

Figure 5.7: Measured power transfer efficiency vs. distance for version 1.

5.5 Measurements

Two versions of the system were tested. The difference between them is the coils. For version 1, coils were hand-wound using Litz-wires at 6 turns with 6.8 cm diameters (Fig. 5.4). The inductance are measured to be $4220nH$ and quality factors $\approx$ 100 at 100 kHz. Figure 5.5 shows that the measured load voltage remains constant up until a certain distance dictated by the critical coupling coefficient. As explained previously, the higher the load power, the shorter the regulation distance is. Similarly, Fig. 5.6 shows that delivered load power also remains constant within regulation range. When delivering $\sim$800 mW, it's able to span $\sim$8 cm; when delivering 5 W, its regulation range is around 4 cm. Figure 5.7 indicates that the efficiency is proportional to the power level, as discussed before. In the extreme case when coils are almost touching, it's able to deliver 11.4 W total power, at $\sim$85% efficiency.

For version 2, coils are the standard TDK WT-505060-8K2-LT coils with ferrite. They are of $4.3cm$ diameters. The inductance and quality factor at 100 kHz are $4950nH$ and 97 respectively. Similarly, Fig. 5.9, Fig. 5.10, and Fig. 5.11 show the delivered load voltage, load

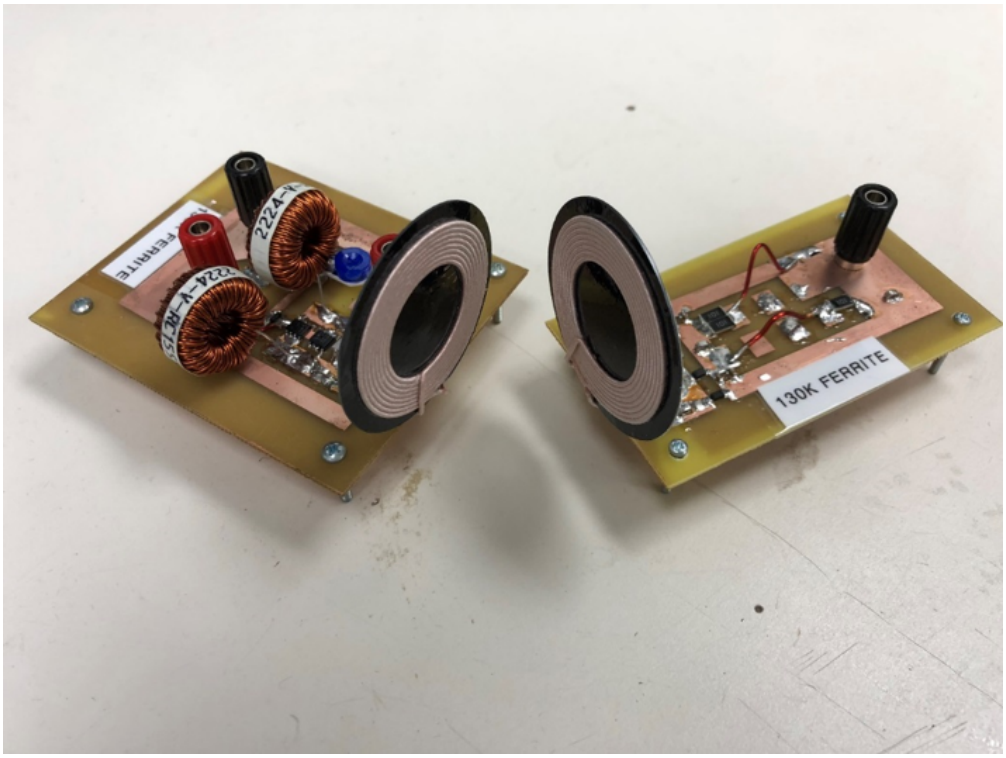

Figure 5.8: Version 2 of the tested systems.

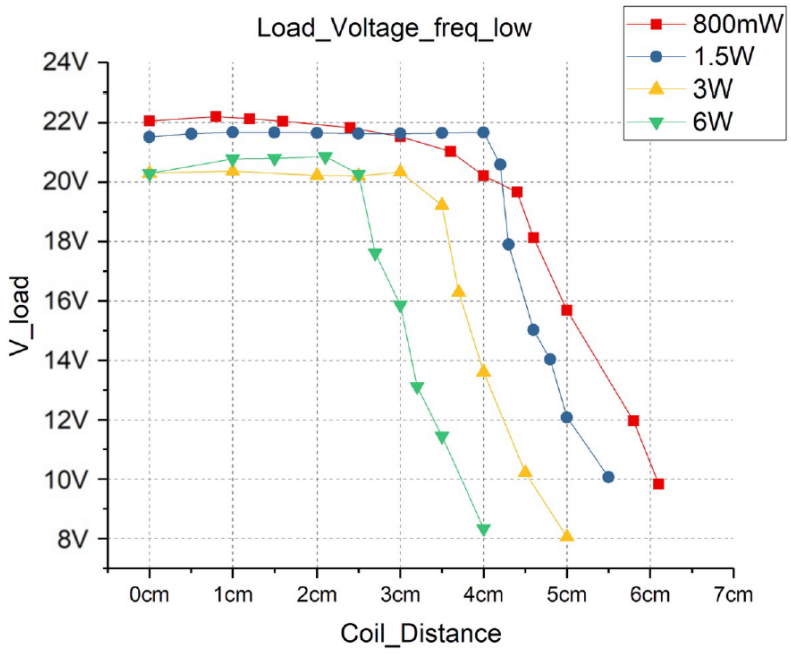

Figure 5.9: Measured delivered voltage vs. distance for version 2.

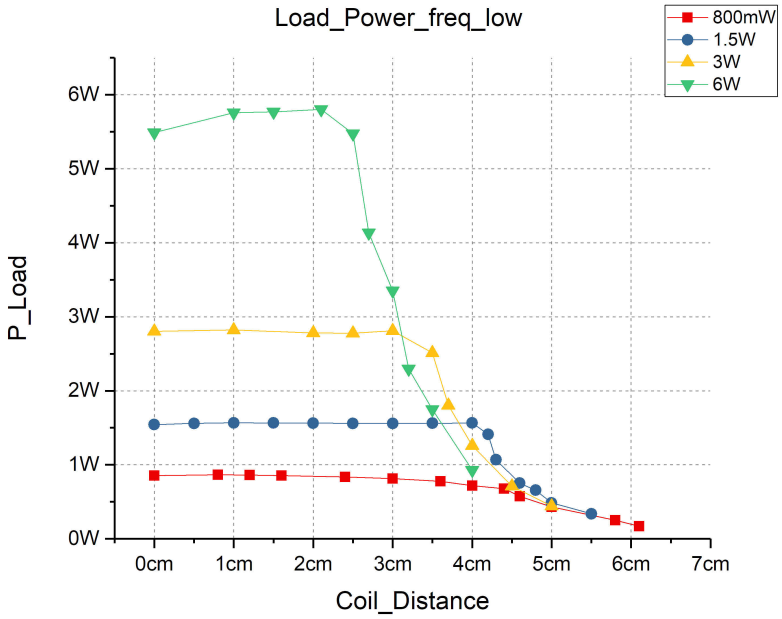

Figure 5.10: Measured delivered load power vs. distance for version 2.

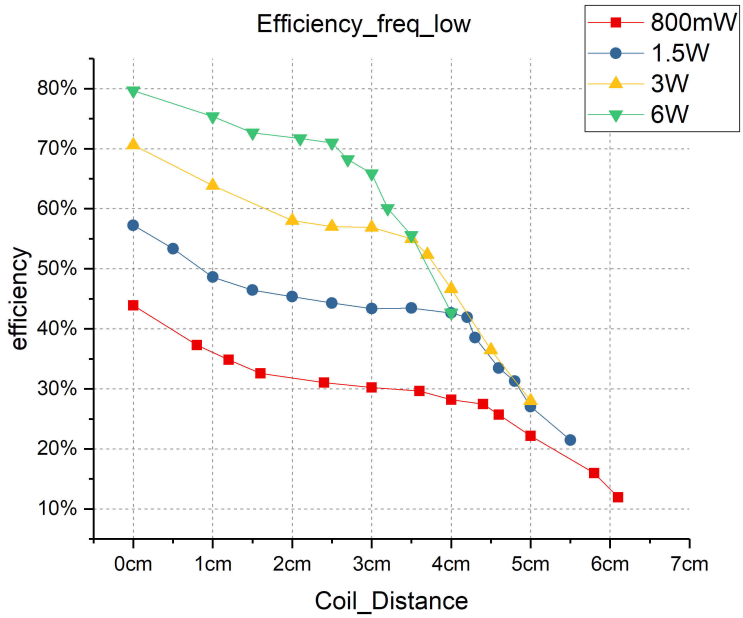

Figure 5.11: Measured power transfer efficiency vs. distance for version 2.

power, and power transfer efficiency vs. coil separation distance. Since coils are smaller, the regulation ranges for same power levels are smaller as compared with version 1. When coils are almost touching, it can deliver up to 11.2 W power with ∼85% peak efficiency.

CHAPTER 6

Second Harmonics in LC Oscillators

6.1 Motivations

In Chapter 3, the design of a good oscillator driver that can achieve high power-conversion efficiency was discussed. The importantce of the RF-chokes was briefly explained, but with many details and derivations omitted there. In this chapter, they will be explained in details. This is done by studying the second/even harmonics (which, as will be shown later, relate to the common-mode operations) in the LC oscilltors, which might not be studied as well as that for the differential-mode of operation for LC oscillators.

Notably, the operations of LC oscillators have been researched by [48]. Time-domain based methods were used, which unavoidably, involve many tedious equations. This work would like to go a different way, and analyze the operations of oscillators in frequency domain. As will be shown in the next section, by performing a frequency-domain based analysis on the harmonics, especially even harmonics, of LC oscillators, it offers a different perspective complementary to the time-domain views in [48], just like the phasor-based analysis on phase noise in [49] to methods of impulse-sensitivity functions in [50].

Moreover, by extending the given analysis, the third section will show that a deeper understanding of even harmonics can lead to a good explanation on the principles of flicker-noise up-conversion.

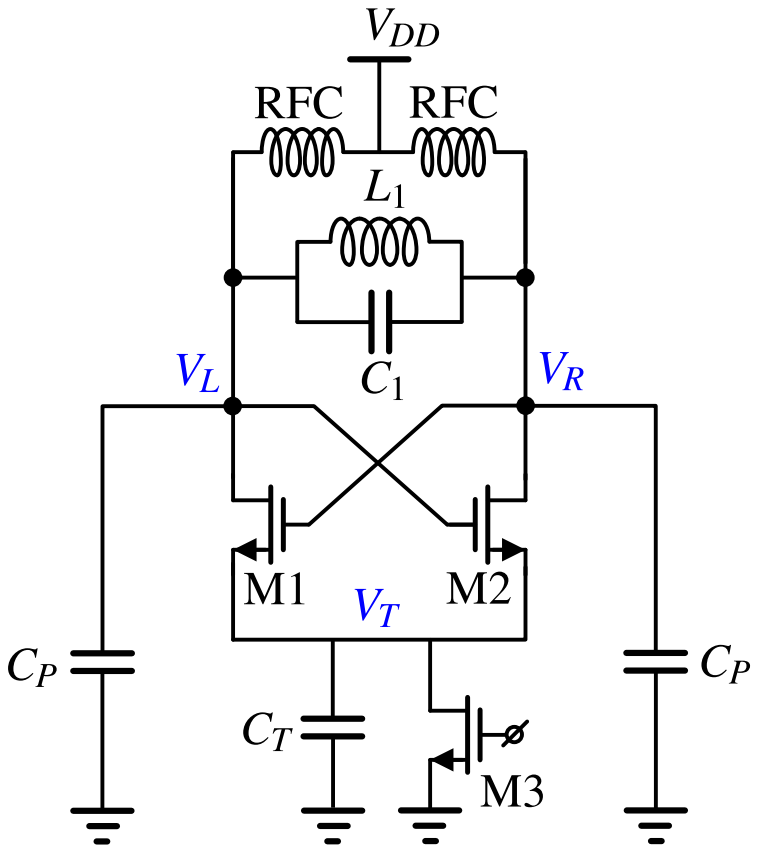

Figure 6.1: Equivalent circuit for the oscillator driver introduced in Chapter 3.

6.2 Second Harmonics for LC Oscillators with Perfect Symmetry and Improving Oscillator's Power Conversion Efficiency

Figure 6.1 shows the implemented oscillator driver for wireless power in Chapter 3. The two C_P are the parasitic capacitors for FETs M1 and M2; C_T is the parasitic capacitor for the tail current FET M3. This circuit is assumed to be fully symmetric for now. Let's start with a quick recapitulation of the differential-mode of operations before stepping into the common-mode analysis.

In steady state, M3 works as the tail DC current source provided that V_T always stays above V_{DSAT} to ensure M3 in saturation at all times. The two RF-chokes, due to their big inductances, act as constant DC current sources, each carrying half ($I_B/2$) of the bias current flowing through M3 (I_B). M1 and M2, due to their big widths, act almost like two

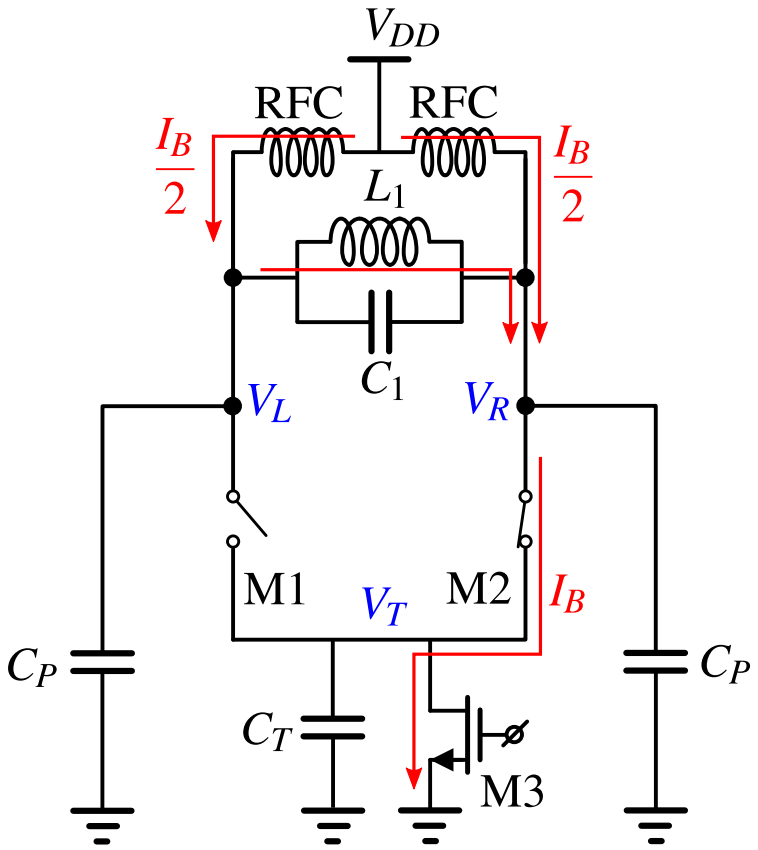

Figure 6.2: Circuit capturing the differential mode of operation for the oscillator driver in Fig. 6.1.

switches, steering the bias current to the left for half a cycle and to the right for the other half. Therefore, differential-wise, the LC tank involving mainly L_1 and C_1 and others such as C_P, RFC, etc. is driven by a current, notated as I_{diff} in Fig. 6.3(a), commutating between $\pm I_B/2$.

I_{diff}'s fundamental frequency is the center frequency of the LC tank. Therefore, almost all other harmonics of I_{diff} will be rejected by the high-Q tank; only the fundamental component will be retained. This means that the resulting oscillation voltage across the tank, $V_L - V_R$, will be a sinusoidal waveform with the same period as I_{diff} (Fig. 6.3(b)):

$$V_L - V_R = A \cdot cos(2\pi f_0 \cdot t), \tag{6.1}$$

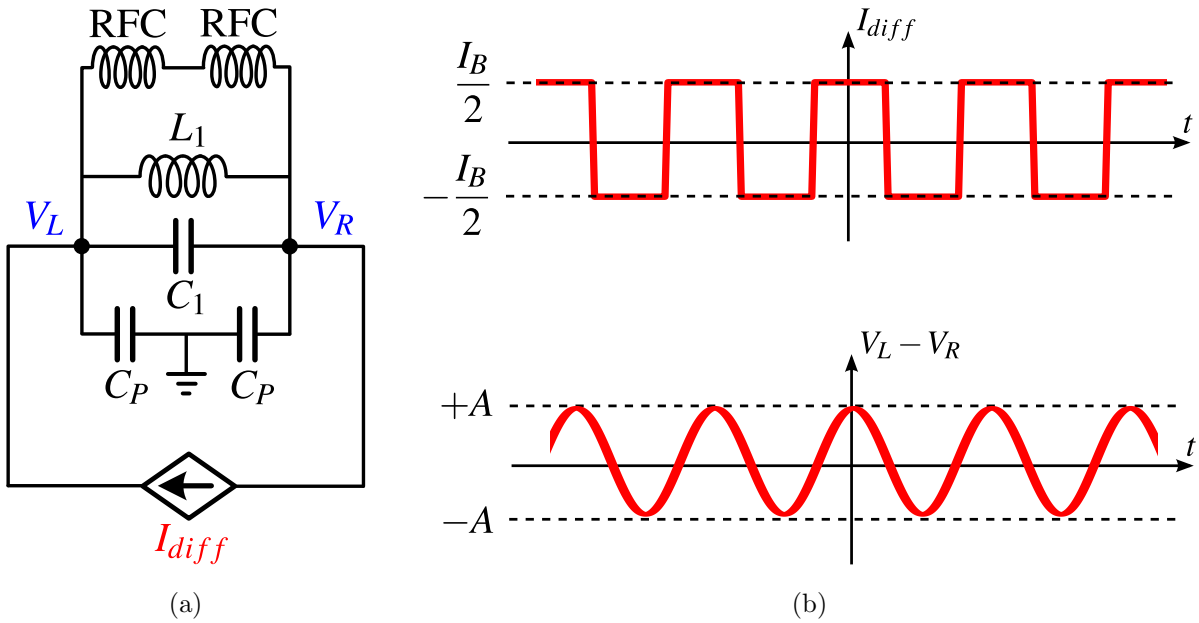

Figure 6.3: (a) The equivalent circuit for differential-mode oscillation in Fig. 6.2. (b) The commutating current source I_{diff}, when driving a high-Q system, results in a sinusoidal oscillation voltage across it.

and

$$2\pi f_0 = \frac{1}{\sqrt{(L1 \,||\, 2L_{RFC})(C1 + C_P/2)}}. \tag{6.2}$$

Its amplitude A is proportional to the driving strength I_B and the quality factor of the LC tank.

That is the differential mode of operation. Next, let's take a look at the common-mode operation of the same circuit.

Common-mode-wise, the circuit is divided in two parts symmetric around the middle dashed line, and all connections crossing the line are open-circuited. C_T is broken into two $C_T/2$ for the purpose of making the whole thing symmetric. Since the two parts are the same, one of them can be analyzed and the conclusion will also apply to the other one. Since DC analysis was done in previous paragraphs, let's focus on AC components. The currents through RF-choke and through C_P will merge together before entering the drain of switching

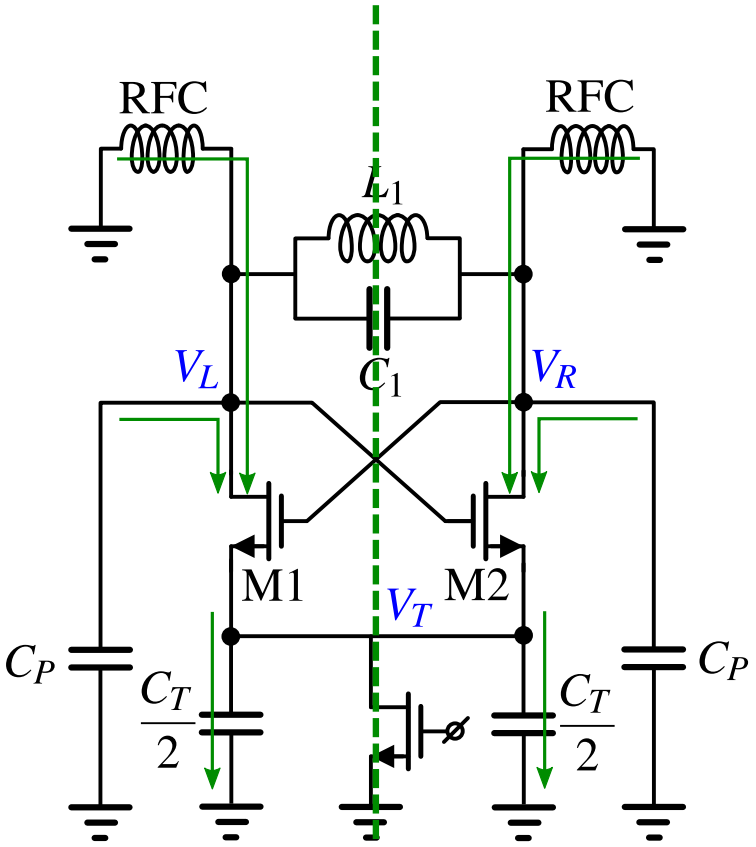

Figure 6.4: Circuit capturing the common mode of operation for the oscillator driver in Fig. 6.1.

FET, M1 or M2, and the total current will go through $C_T/2$, assuming the tail current FET carries no AC because it stays in saturation at all times.

Moreover, by symmetry, V_R is V_L shifted by half a cycle in time domain. Then in frequency domain, V_R is V_L with all odd harmonics inverted, and even harmonics remaining unchanged. Therefore, when taking the subtraction of them, even harmonics all get cancelled, but odd harmonics will all be reinforced. However, (6.1) states that their subtraction only has one component at f_0 given in (6.2). This means that for both V_L and V_R, their even harmonics (including DC components) are still to be determined, but they only have odd harmonics at the fundamental frequency f_0.

Also, since only the even harmonics of V_L and V_R are the same, then the common-mode operations only refer to the even harmonics (including DC components). As a result, if only

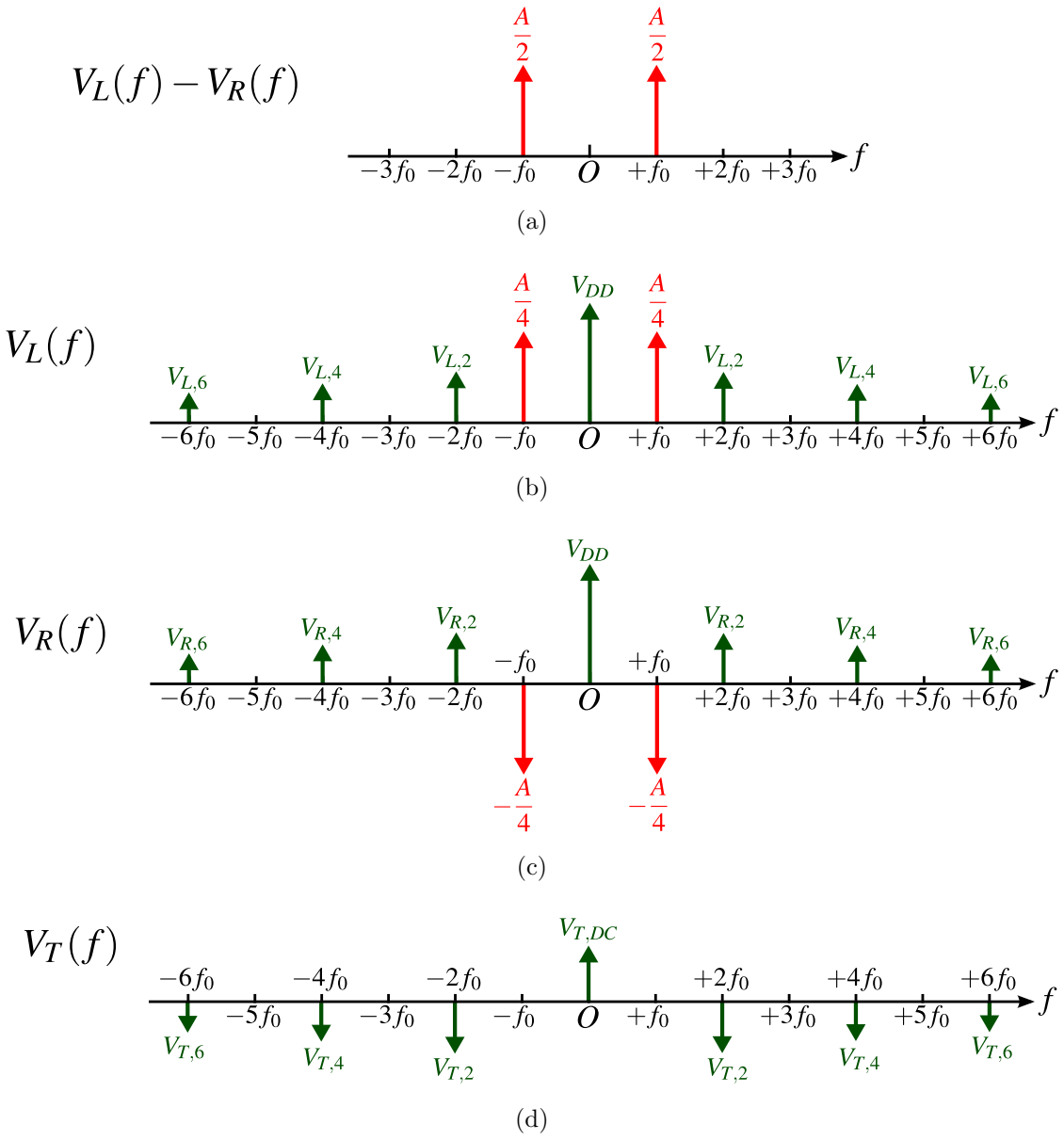

Figure 6.5: The frequency domain components for (a) $V_L - V_R$, (b) V_L, (c) V_R, and (d) V_T.

looking at the second harmonics for ease of analysis and ignore all others (4th, 6th, etc.), the following equation holds:

$$V_{T,2} = -V_{R,2} \cdot \frac{2(sC_P + \frac{1}{sL_{RFC}})}{sC_T} \approx -2\frac{C_P}{C_T} \cdot V_{R,2}, \text{ if } L_{RFC} \uparrow\uparrow , \tag{6.3}$$

by Kirchhoff's Current Law (KCL) analysis.

Plotting the components in frequency domain, it is shown as Fig. 6.5. To achieve the

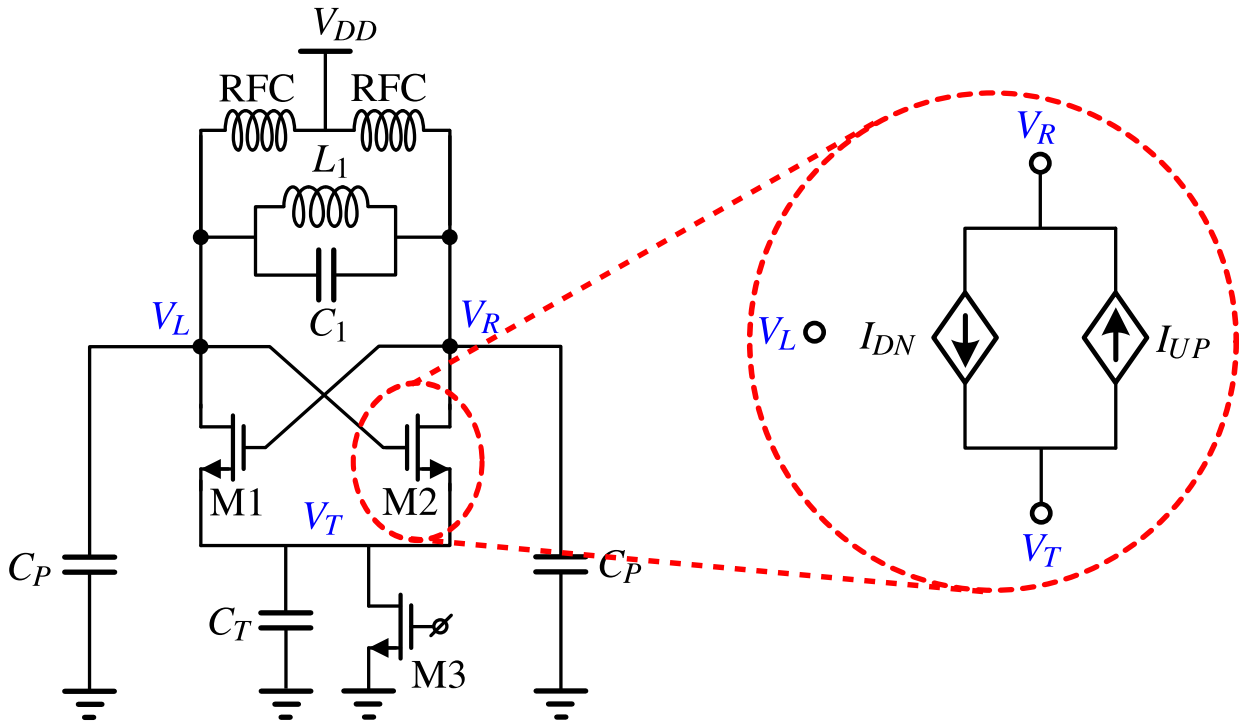

Figure 6.6: The switching FET, M1 or M2, is the key to link currents and voltages together and, thus, to calculate the magnitudes of the even harmonics.

differential oscillation voltage as in Fig. 6.5(a), V_L and V_R must like like Fig. 6.5(b) and Fig. 6.5(c). Also, based on the relation in (6.3), given that V_R looks like Fig. 6.5(c), V_T should be Fig. 6.5(d).

Now, the magnitude of even harmonics still remain to be determined. The key lies in the switching FET, M1 or M2. This is because both odd and even harmonics merge and go through the switching FET; also, FETs are voltage-controlled current sources (Fig. 6.6). Take M2 as an example, its gate-, source-, and drain-voltage are V_L, V_T, and V_R. As shown in Fig. 6.6, they control two current sources I_{DN} and I_{UP}. I_{DN} is controlled by gate and source:

$$I_{DN} = \begin{cases} 0 & \text{if } V_L - V_{th} - V_T < 0 \ ; \\ \dfrac{\beta(V_L - V_{th} - V_T)^2}{2} & \text{else.} \end{cases} \tag{6.4}$$

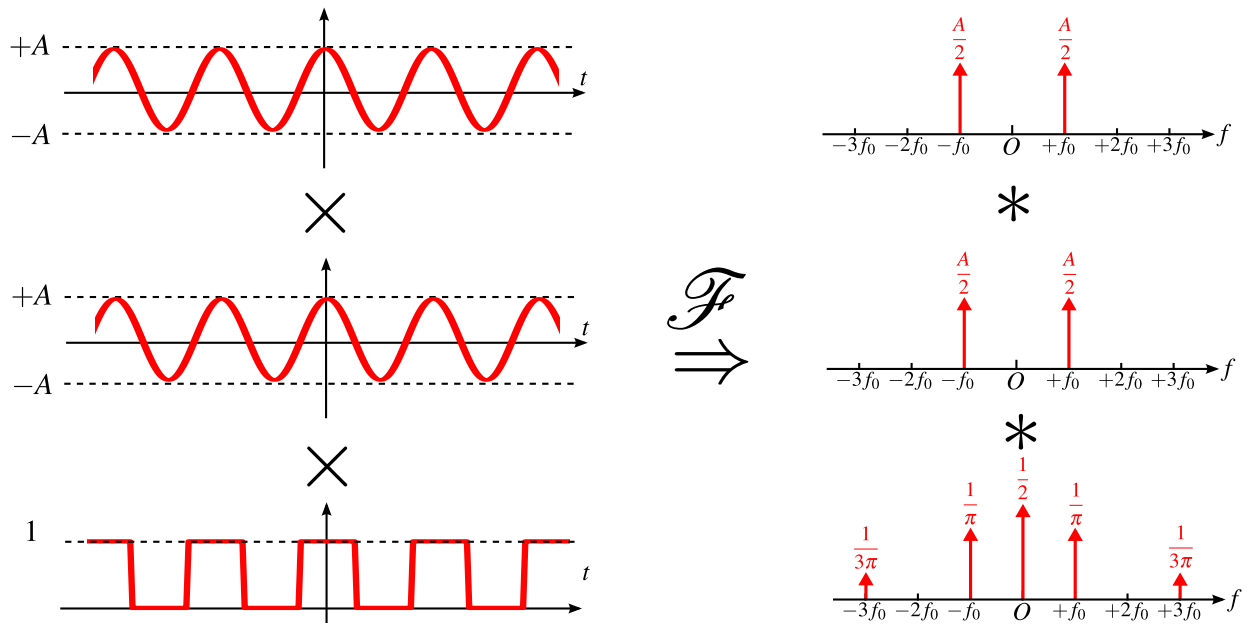

Figure 6.7: The time domain and frequency domain representations for $I_{UP}/(\beta/2)$ when assuming $V_{th} \to 0$.

I_{UP} is controlled by gate and drain:

$$I_{UP} = \begin{cases} 0 & \text{if } V_L - V_{th} - V_R < 0 \ ; \\ \dfrac{\beta(V_L - V_{th} - V_R)^2}{2} & \text{else.} \end{cases} \tag{6.5}$$

V_{th} is the threshold voltage for M1 or M2.

Without loss of generality, let's focus on the second harmonic only. The following relation holds, due to KCL:

$$I_{DN,2} - I_{UP,2} = V_{T,2} \cdot s\frac{C_T}{2} \approx V_{R,2} \cdot sC_P. \tag{6.6}$$

Now, assume that $V_{th} \to 0$, then I_{UP} becomes a sinusoidal waveform that is first squared, and then half-wave rectified, which is essentially the result of the multiplication of two sine-waves and one square wave as shown in Fig. 6.7. In frequency domain, it becomes convolution of three parts which will gives

$$I_{UP,2} = \frac{\beta}{2} \times \frac{A^2}{8}. \tag{6.7}$$

Comparing the magnitude of $I_{UP,2}$ with that of $V_{R,2} \cdot sC_P$,

$$|I_{UP,2}| = \frac{\beta}{2} \times \frac{A^2}{8}, \text{ where } \beta = \mu \cdot C'_{ox} \cdot \frac{W_{M2}}{L_{M2}}, \tag{6.8}$$

and

$$|V_{R,2} \cdot j\omega C_P| = V_{R,2} \cdot \omega C_P, \text{ where } C_P \approx C'_{ox} \cdot W_{M2} \cdot L_{M2}. \tag{6.9}$$

The ratio of $|I_{UP,2}|$ over $|V_{R,2} \cdot \omega C_P|$ is then, roughly on the same order of $\beta/(\omega C_P)$ in this work, and

$$\frac{\beta}{\omega C_P} \approx \frac{\mu}{{L_{M2}}^2 \cdot 2\pi f_0} \gg 1 \tag{6.10}$$

for this work. As a result, specifically for this work, (6.6) becomes

$$I_{DN,2} \approx I_{UP,2}. \tag{6.11}$$

The derivaton of $I_{DN,2}$ follows almost the same procedures as that of $I_{UP,2}$ and uses the same principle that multiplication in time domain is equivalent to convolution in frequency domain. $V_L(f)$ and $V_T(f)$ are given in Fig. 6.7 already; it can be shown that

$$I_{DN,2} \approx \frac{\beta}{2}\left[\frac{A^2}{16} + 2(V_{DD} - V_{T,DC}) \cdot (1 + 2\frac{C_P}{C_T}) \cdot V_{L,2}\right]. \tag{6.12}$$

Combining (6.7), (6.12), and (6.11), the following conclusion is drawn:

$$\boxed{V_{L,2} = V_{R,2} = \frac{A^2}{32(V_{DD} - V_{T,DC})(1 + 2\frac{C_P}{C_T})}.} \tag{6.13}$$

One other important equation to guide designs is (6.3), which will be re-written here to emphasize its importance:

$$\boxed{V_{T,2} = -V_{R,2} \cdot \frac{2(sC_P + \frac{1}{sL_{RFC}})}{sC_T}.} \tag{6.14}$$

Now, with (6.14), it becomes clear that to reduce the fluctuations at V_T, which are equivalently the magnitudes of even harmonics, besides using a large RF-choke, the FETs should also be sized properly so that $C_T \gg C_P$. In that case, $V_{T,2}$ becomes negligible, indicating

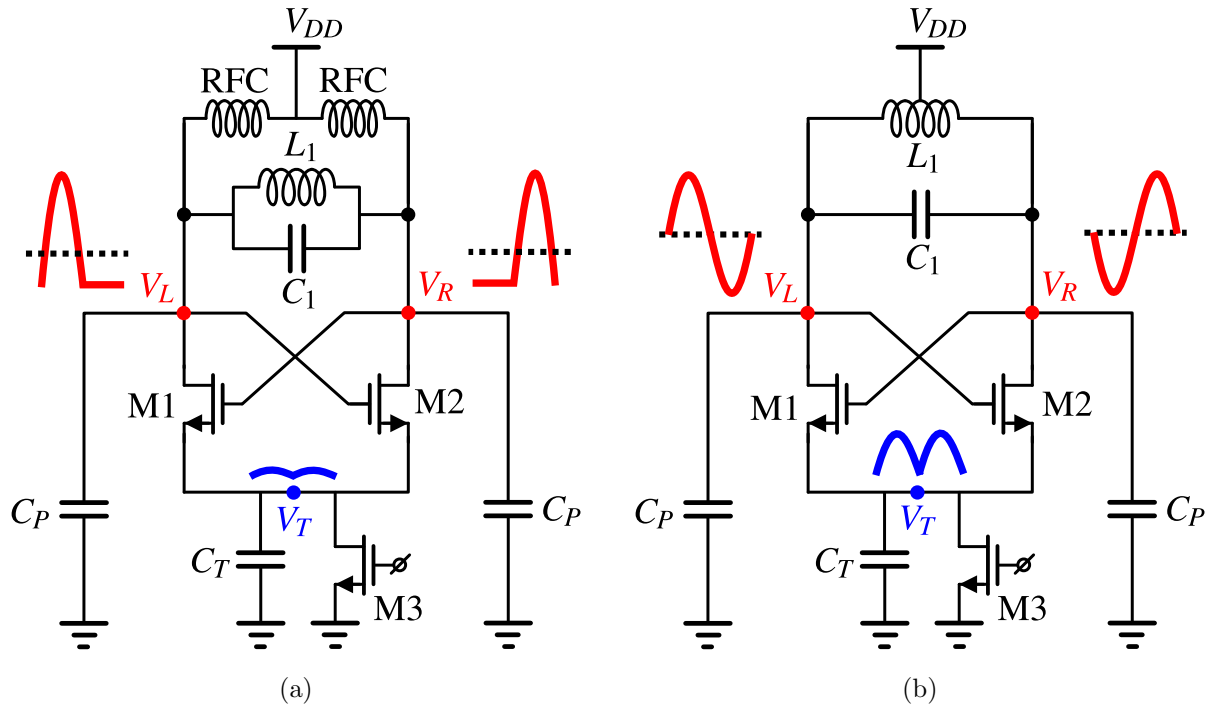

Figure 6.8: (a) With big RF-chokes and proper sizings of FETs, the V_T can have very little fluctuations; V_L and V_R have big even harmonics that make them look like class-D type of oscillations. (b) Without RF-chokes, the oscillation is more like traditional class-B type for this current-mode oscillator.

that V_T is almost DC-only, which is desired for better power-conversion efficiency for the design described in Chapter 3. The actual operating waveforms will look like Fig. 6.8(a), where there is huge even harmonics at V_L and V_R, but barely any fluctuation at V_T. The waveforms at V_L and V_R are almost like those for a class-D oscillator, indicating almost 100% power conversion efficiency at the switching FETs.

However, if RF-chokes were not used, things are changed completely. The L_{RFC} in (6.14) becomes $L_1/2$, and its reactance at f_0 is equal to that of C_1. But since C_1 is much larger than C_P in this work, then $L_1/2$'s reactance is much smaller than C_P's or C_T's reactances at f_0. Plugging this new relation in (6.14), it can be predicted that there are huge fluctuations at V_T but very weak even harmonics at V_L and V_R. The oscillation waveforms now look very much like the ones for class-B oscillators (Fig. 6.8(b)) described in many works such as [48].

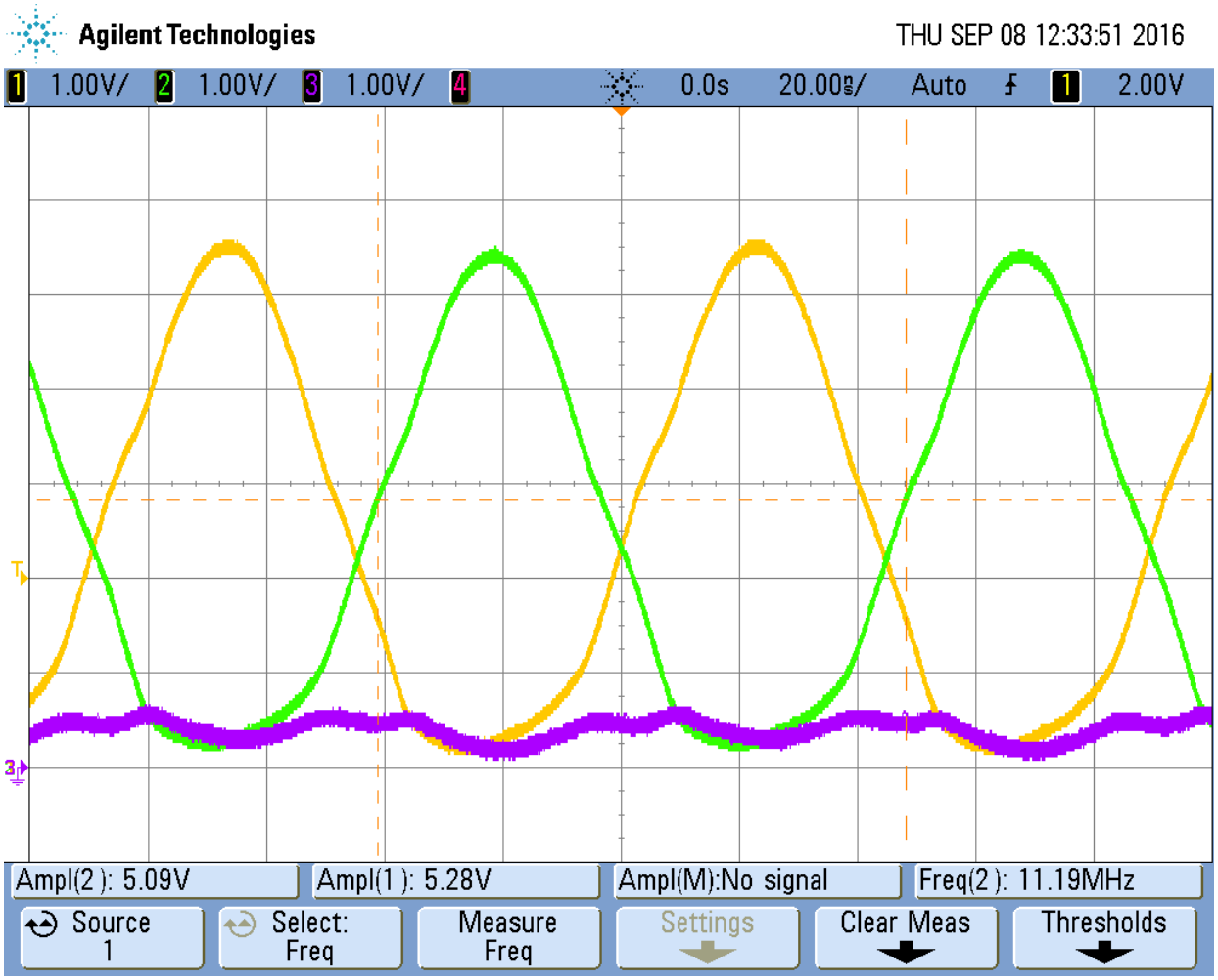

Figure 6.9: Measured waveforms for the oscillator driver in [35]. The yellow and green waveforms correspond to V_L and V_R, and the purple waveform is V_T.

There will be poor power-conversion efficiency and this oscillator is not suitable to work as drivers for wireless power systems.

The measurements for the system described in [35] (Fig. 6.9) indicate that by following the design advice above, indeed the fluctuations at the drain of tail current source can be minimized to improve the power-conversion efficiency of the oscillator driver.

6.3 Second Harmonics for Systems with Mismatch in Threshold Voltages and Flicker Noise Up-conversion

In the previous section, derivations were based on the assumption that the oscillator driver is fully symmetric. However, there will always be asymmetry in the circuit. In this section, it will be shown that mismatches in the threshold voltages of the switching FETs can result in a shift in the oscillation frequency. This can lead to the explanation of the principles of flicker-noise up-conversion.

Figure 6.10 shows almost the same equivalent circuit for oscillator driver discussed previously, but with mismatches in threshold voltages. Without loss of generality, let's assume

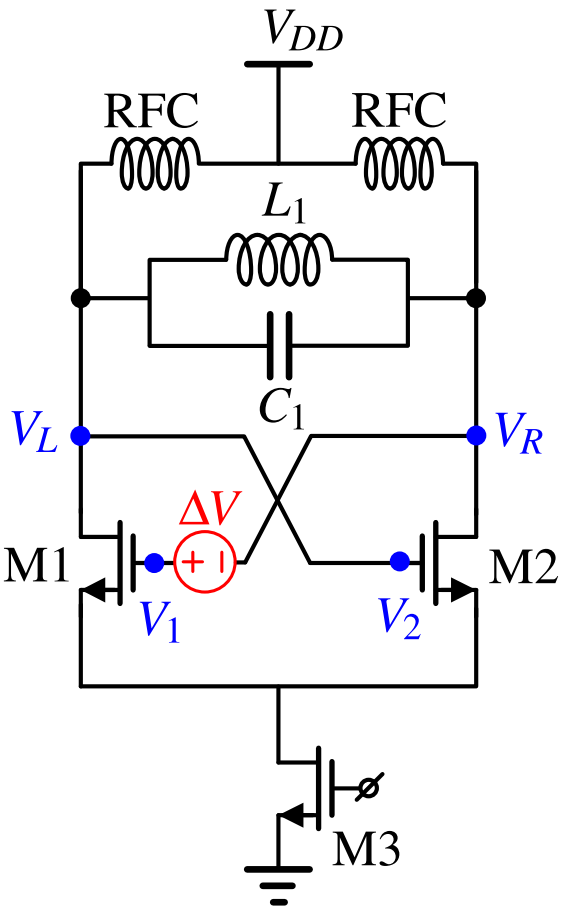

Figure 6.10: The equivalent circuit for oscillator driver with mismatches in threshold voltages of M1 and M2.

that M1's threshold voltage is reduced by ΔV. Now, for any given differential voltage $(V_L - V_R)$, the differential voltage right at the gate of switching FETs is

$$V_1 - V_2 = V_R + \Delta V - V_L = (V_R - V_L) + \Delta V. \tag{6.15}$$

Since M1 and M2 are identical, then by symmetry, current steering direction changes at the moment of zero-crossings of $(V_1 - V_2)$.

Assume that $(V_R - V_L)$ is sinusoidal as discussed before, then $(V_1 - V_2)$ is the same sinusoid, shifted vertically by ΔV. Since $(V_1 - V_2)$ is no longer symmetric around the horizontal axis,

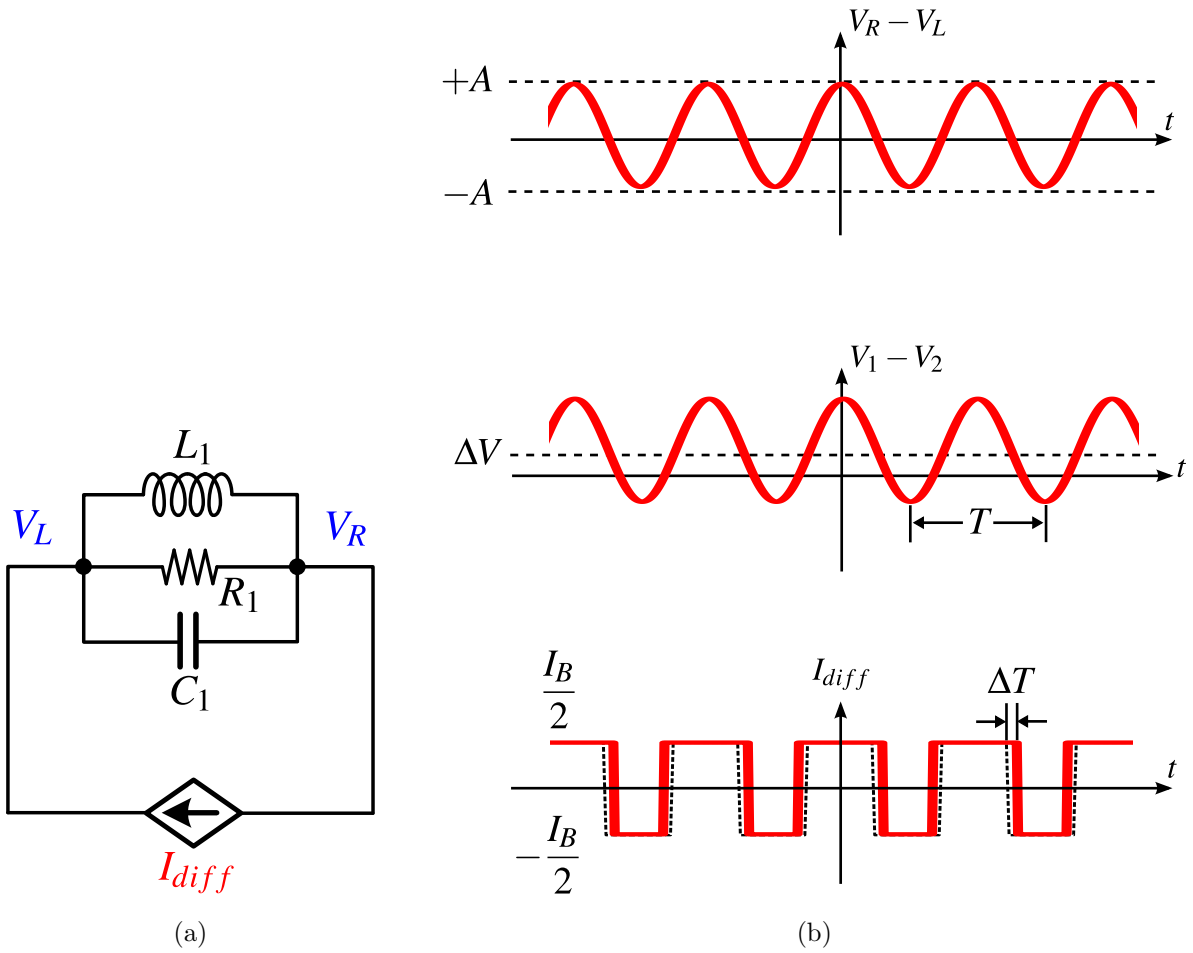

Figure 6.11: (a) Differential-wise, the circuit in Fig. 6.10 becomes a I_{diff} driving an LC tank. (b) $(V_1 - V_2)$ is the original $(V_R - V_L)$ shifted vertically by ΔV, resulting in a non-50% duty-cycle I_{diff} in which ΔT is related to ΔV.

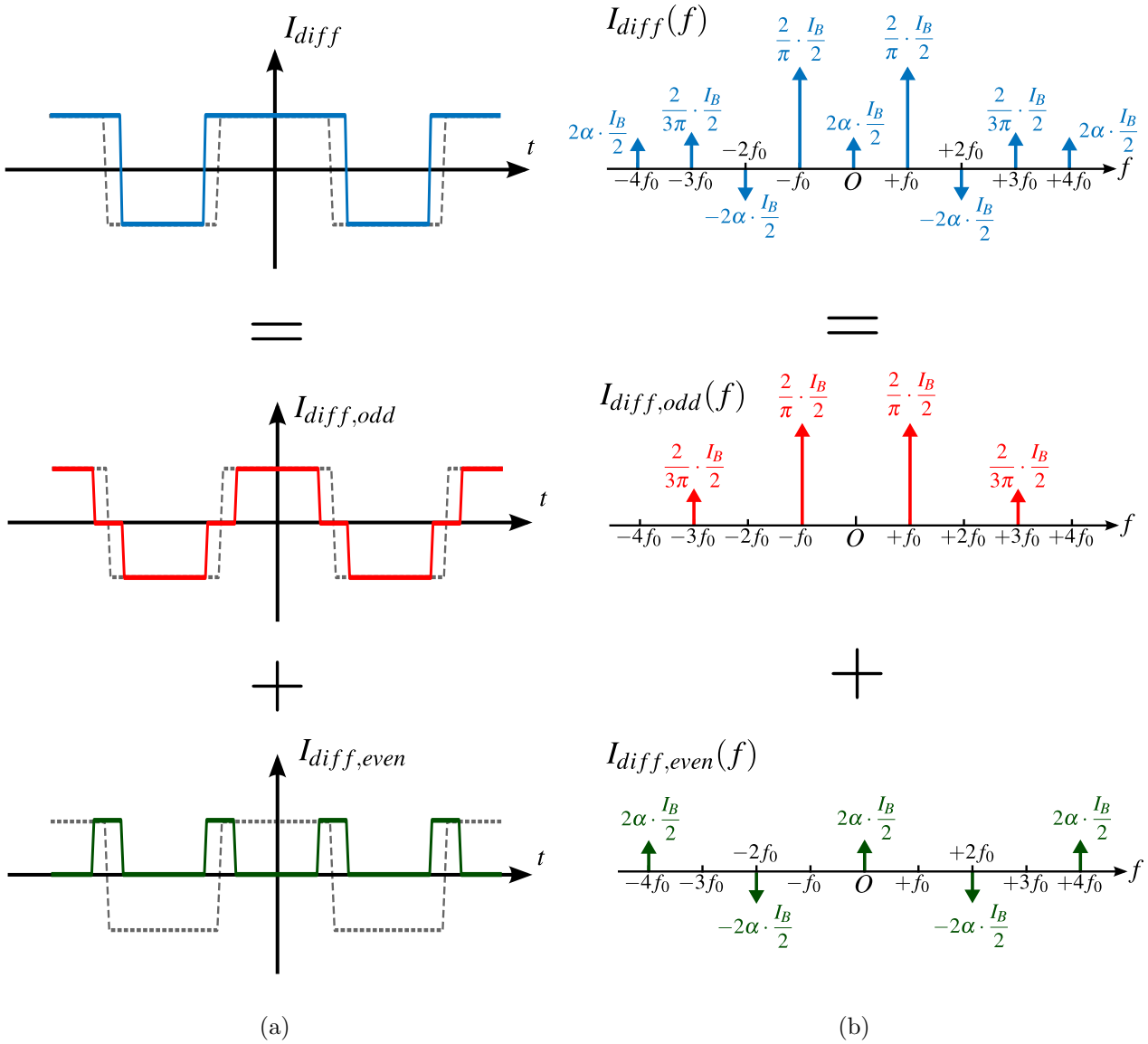

Figure 6.12: (a) Time-domain representations of I_{diff}. (b) The frequency-domain representations of I_{diff}.

the differential current driving the tank (Fig. 6.11(a)) will no longer have 50% duty-cycle (Fig. 6.11(b)). Notation-wise:

$$\text{duty cycle } = 50\% + \alpha; \tag{6.16}$$

$$\alpha = \frac{2\Delta T}{T}, \tag{6.17}$$

where the definitions for T and ΔT are depicted in Fig. 6.11(b). The new differential driving

current I_{diff} is composed of both even and odd harmonics (Fig. 6.12). Assume that α is small, then its odd components look much like those for a square wave. The even harmonics of I_{diff} are proportional to α.

So far, the current I_{diff} has been calculated from the waveforms of differential voltage $(V_R - V_L)$ and the threshold voltage mismatch ΔV. To complete the loop, it should also be possible to derive the differential voltages based on the current I_{diff}.

There are two important equalities to be met. First, the I_{diff} is the stimulus and $(V_R - V_L)$ is the response to the stimulus driving the LC tank (Fig. 6.13):

$$I_{diff}(j\omega) \cdot Z_1(j\omega) = -(V_R - V_L)(j\omega). \tag{6.18}$$

As shown in Fig. 6.13, the tank's impedance $Z_1(j\omega) = j\omega L_1 \,||\, 1/(j\omega C_1) \,||\, R_1$ has the plotted

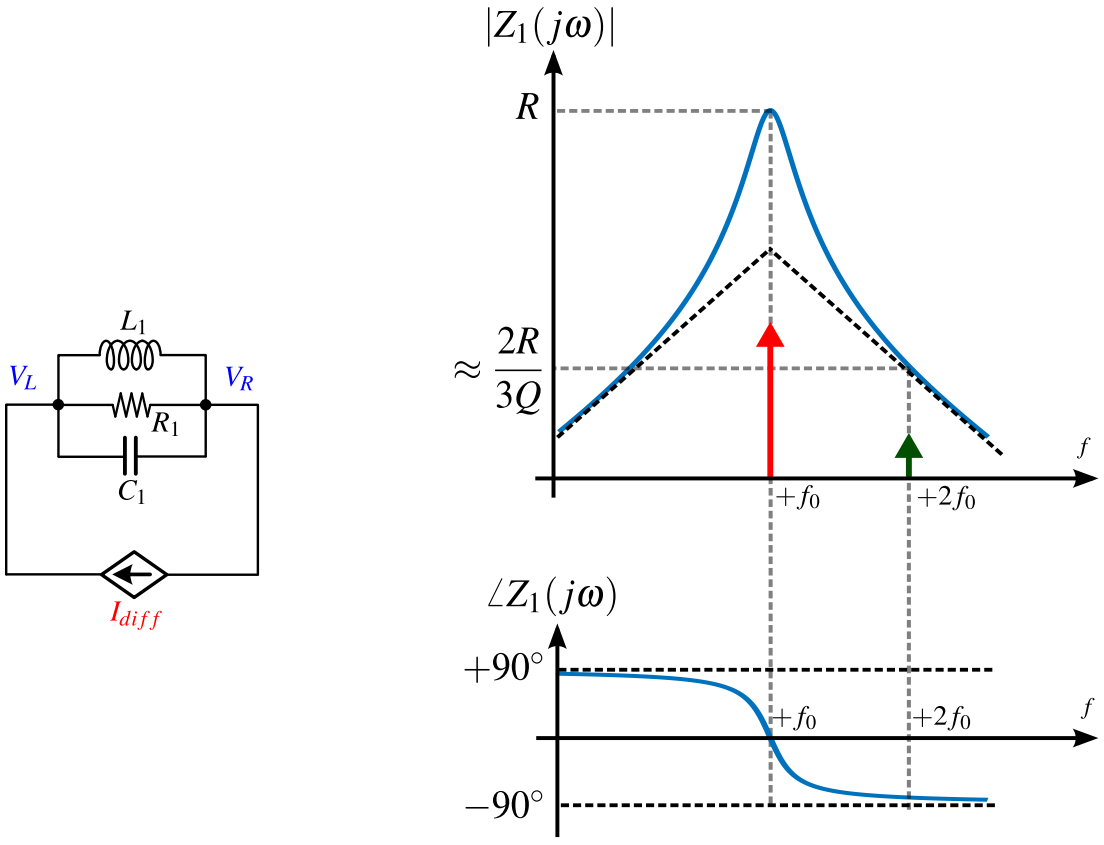

Figure 6.13: The frequency response of the tank's impedance $Z_1(j\omega)$ is plotted. The differential voltage $(V_R - V_L)$ should be the result of the stimulus I_{diff} driving the tank.

magnitude and phase vs. frequency. The DC component of I_{diff} sees a zero gain and is thus ignored. The fundamental and second harmonic are plotted; the other harmonics are ignored for ease of analysis. It is clear that the fundamental component is amplified by R and has no phase shift; the second harmonic sees a smaller gain and an almost $-90°$ phase shift.

The second equality is:

$$I_{diff}(t)\text{'s zero-crossings} = (V_1(t) - V_2(t))\text{'s zero-crossings}, \tag{6.19}$$

as stated before. This is because $(V_1 - V_2)$ is the control signal for the current-steering switches M1 and M2. Therefore, following the frequench response in Fig. 6.13, $(V_1 - V_2)$ in time domain should look like Fig. 6.14. This V_{diff} should have the same zero-crossings as those for I_{diff} shown in Fig. 6.12, which is symmetric around the vertical axis. However,

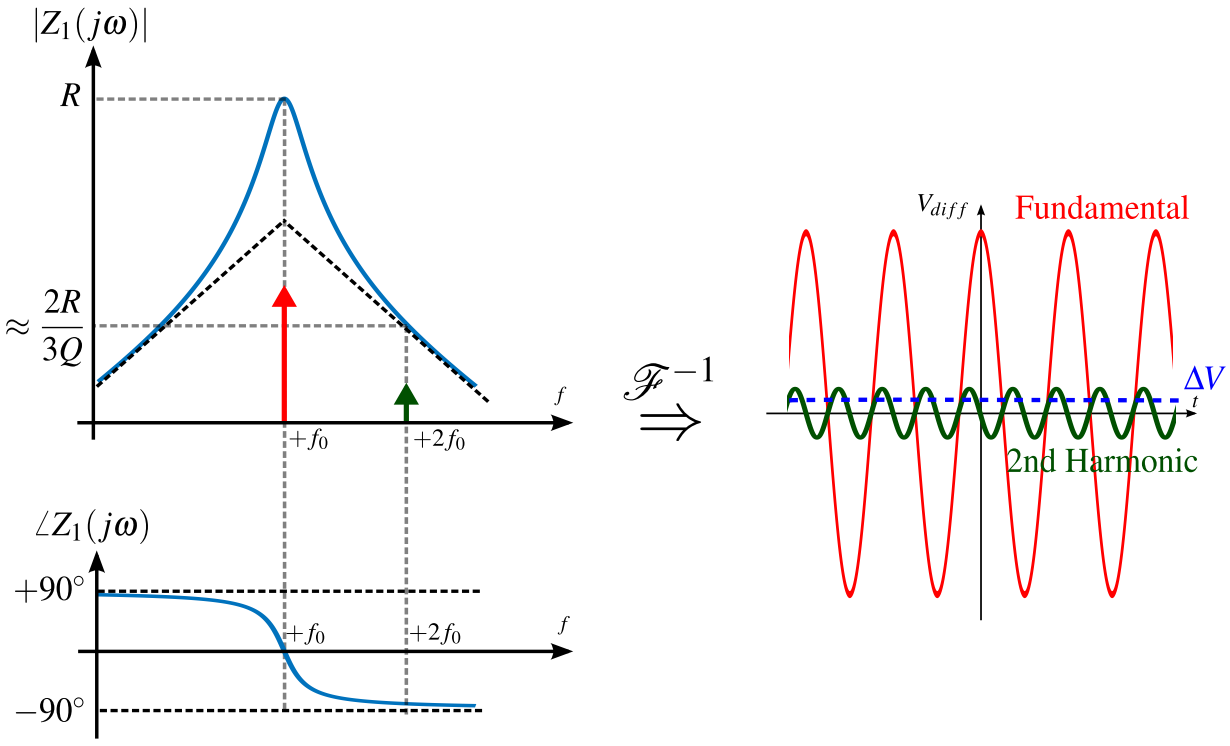

Figure 6.14: When the current stimulus drives the tank Z_1, it has a time-domain waveform as shown above. $V_1 - V_2$ is the summation of three waveforms: fundamental, second harmonic, and a DC component ΔV.

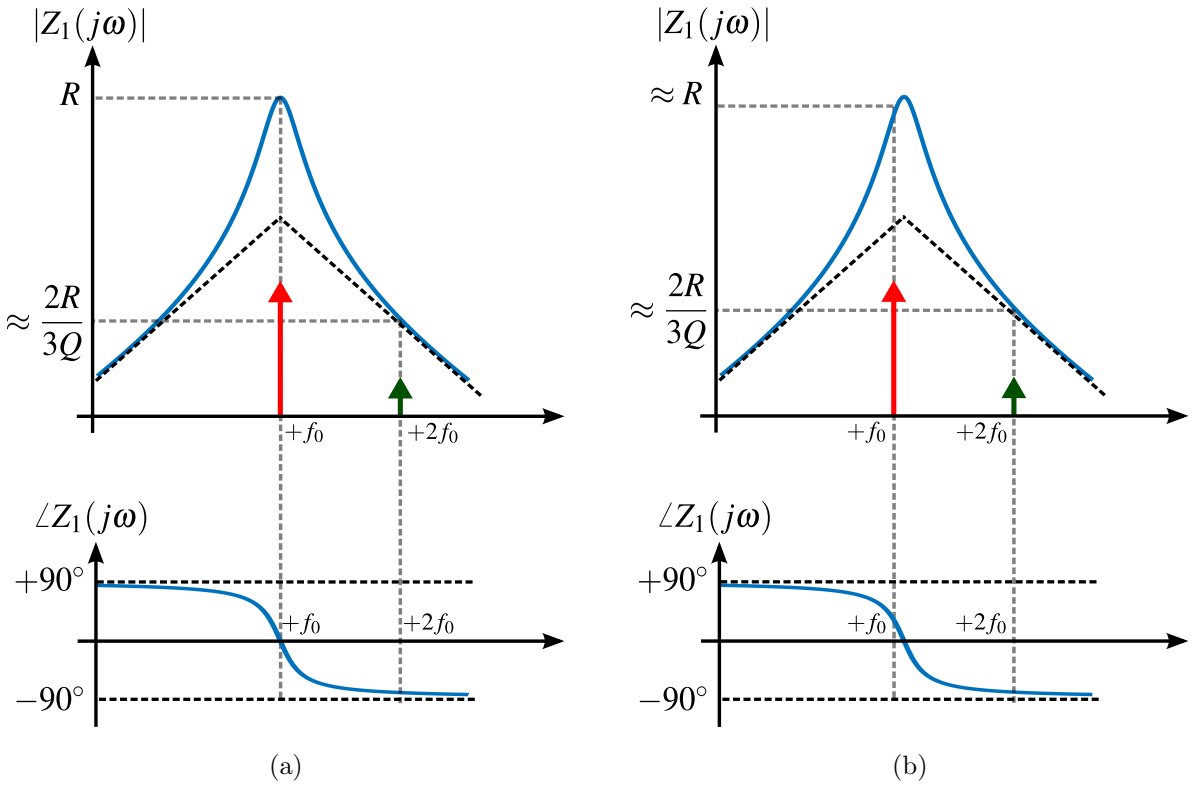

(a) (b)

Figure 6.15: (a) Originally, it was assumed that the fundamental frequency of I_{diff} is equal to the center frequency of the LC tank. However, if that is the case, then the two equations mentioned above cannot be satisfied simultaneously (b) To fix that problem, the I_{diff}, in terms of the frequency-domain components, should be shifted to the left by a certain amount.

the existance of $-90°$ shifted second harmonic (which is a inverse sine function) breaks the symmetry!

To fix this contradiction and make the two equalities above hold simultaneously, it has to be the case that the fundamental component of I_{diff} is not at the center frequency of the Z_1 tank. In other words, the frequency components of I_{diff} are shifted by some Δf (Fig. 6.15). As a result of this, they will still see a roughly unchanged gain, and second harmonic will still experience a $-90°$ phase shift. Nevertheless, the fundamental component will see some non-zero phase shift.

Let's now calculate how much this shift needs to be. Suppose the fundamental component

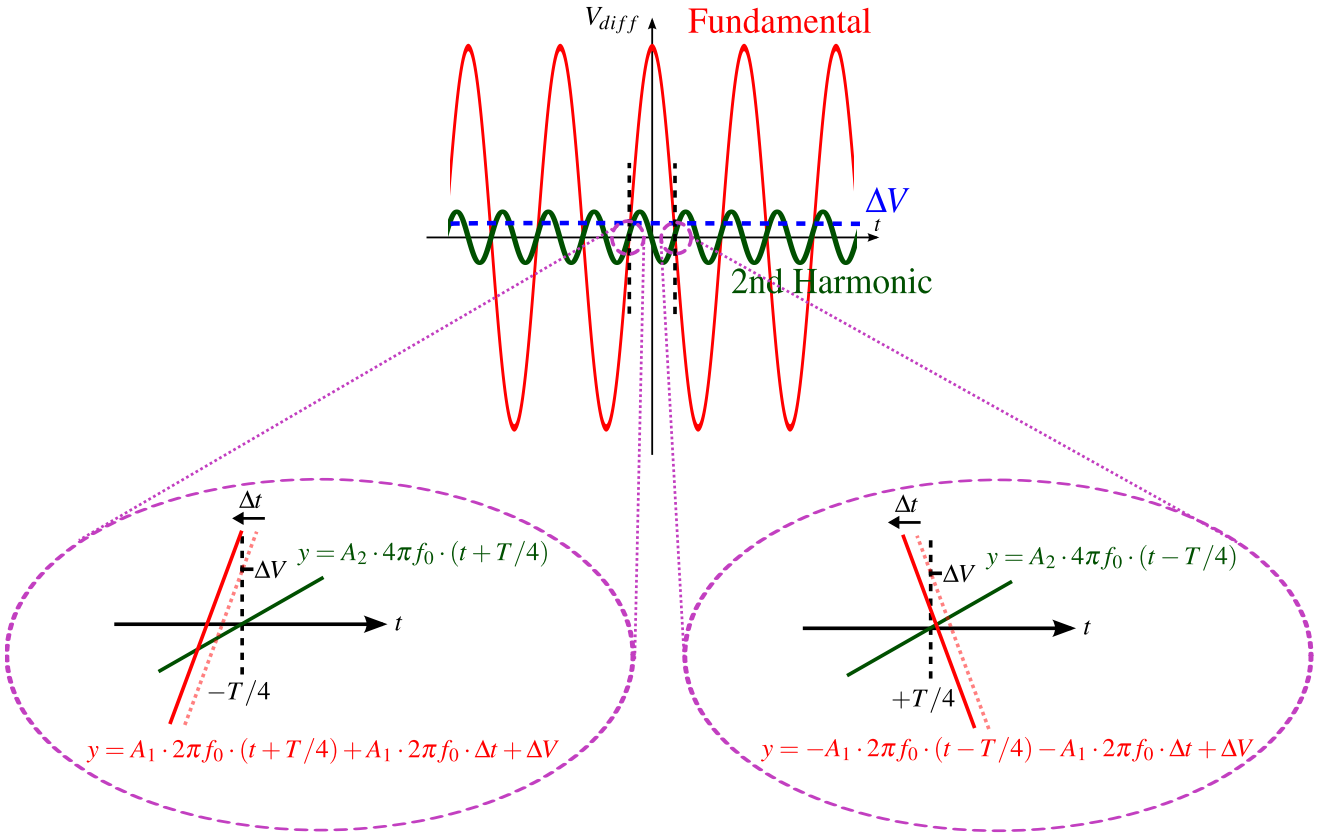

Figure 6.16: If zooming into the zero-crossings, sinusoidal functions may be approximated by linear functions, simplifying the calculation without losing too much accuracy.

is shifted to the left by Δt. Then, if just focusing on the zero-crossings, the sinusoidal waveforms can be approximated using linear functions as shown in Fig. 6.16. The zero-crossing of the left part would be:

$$t_{left} = -\frac{A_1 \cdot \Delta t + \Delta V / 2\pi f_0}{A_1 + 2A_2} - T/4, \tag{6.20}$$

where A_1 and A_2 are the amplitudes of the fundamental and second harmonic differential voltage $(V_R - V_L)$. Since I_{diff}'s frequency plots are shown in Fig. 6.12(b), and the frequency response for the tank's impedance Z_1 is shown in Fig. 6.13, it could be calculated that

$$\frac{A_2}{A_1} = \frac{2\alpha\pi}{3Q} \triangleq A_{21}, \tag{6.21}$$

in which Q is the quality of the LC tank. Similarly, the zero-crossing of the right part is:

$$t_{right} = \frac{A_1 \cdot \Delta t - \Delta V / 2\pi f_0}{-A_1 + 2A_2} + T/4. \tag{6.22}$$

They should be symmetric around the vertical axis:

$$|t_{left}| = |t_{right}|. \tag{6.23}$$

Combining (6.20), (6.22), and (6.23), it could be calculated that

$$\Delta t = \frac{\Delta V}{\pi f_0} \cdot A_{21} \cdot \frac{1}{A_1}. \tag{6.24}$$

Given (6.21), (6.24) is further simplified to

$$\Delta t = \frac{2\alpha\pi}{3Q} \cdot \frac{\Delta V}{\pi f_0} \cdot \frac{1}{A_1} = \frac{2\alpha\Delta V}{3Qf_0} \cdot \frac{1}{A_1}. \tag{6.25}$$

The Δt shift in time domain maps to a $\Delta\phi$ shift in frequency domain:

$$\frac{\Delta t}{\frac{1/f_0}{4}} = \frac{\Delta\phi}{\frac{\pi}{2}} \tag{6.26}$$

$$\Rightarrow \quad \Delta\phi = \Delta t \cdot 2\pi f_0 = \frac{4\alpha\pi\Delta V}{3Q} \cdot \frac{1}{A_1}. \tag{6.27}$$

This can only be achieved if the fundamental frequency f_0 is shifted to the left to a new f_0' as shown in Fig. 6.15.

For the phase vs. frequency of $Z_1(j\omega)$ as shown in Fig. 6.15, at the zero-crossing of that, the slope is roughly $-2Q$, meaning that:

$$\frac{\Delta\phi}{log(\omega_0) - log(\omega_0')} = 2Q \tag{6.28}$$

$$\Rightarrow \quad \frac{\Delta\phi}{2Q} = log\left(\frac{\omega_0}{\omega_0'}\right) = log\left(\frac{2\pi f_0}{2\pi f_0'}\right). \tag{6.29}$$

This gives

$$log\left(\frac{f_0}{f_0'}\right) = \frac{2\alpha\pi \cdot \Delta V}{3Q^2} \cdot \frac{1}{A_1} \tag{6.30}$$

$$\Rightarrow \quad \frac{f_0}{f_0'} = exp\left(\frac{2\alpha\pi \cdot \Delta V}{3Q^2} \cdot \frac{1}{A_1}\right). \tag{6.31}$$

Moreover, by the definition (6.17), and assuming that the amplitude of fundamental component, A_1, is roughly equal to the amplitude of the entire waveform, A, the following conclusion can be arrived at:

$$\frac{f_0}{f_0'} = exp\left[\frac{2}{3Q^2} \times \left(\frac{\Delta V}{A}\right)^2\right]. \tag{6.32}$$

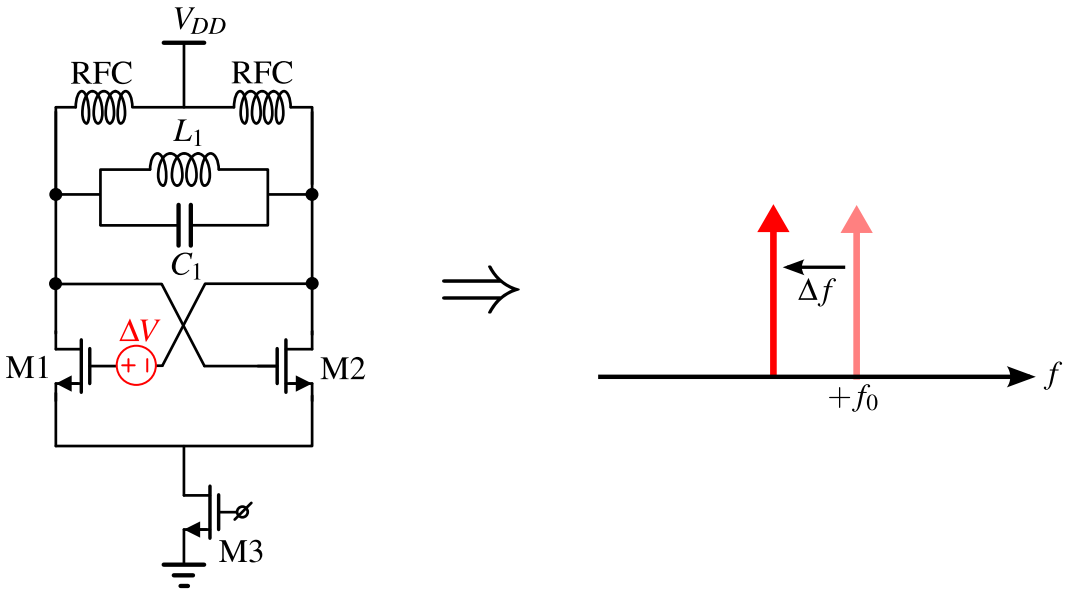

Figure 6.17: In conclusion, a ΔV mismatch in threshold voltage of the switching FETs result in a Δf, expression given in (6.33), shift in oscillation frequency.

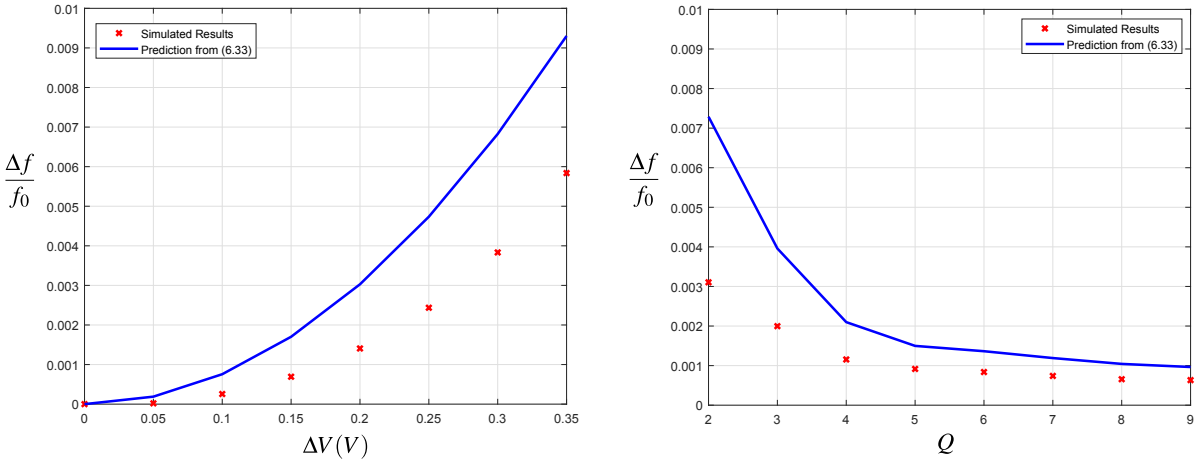

(a) (b)

Figure 6.18: (a) Simulated and predicted Δf vs. ΔV. The larger the mismatch is, the more the frequency deviation gets. (b) Simulated and predicted Δf vs. Q. With increasing quality of the tank, the frequency difference becomes smaller.

The actual frequency shift, $\Delta f = f_0 - f_0'$, as a result of a ΔV mismatch in threshold voltage is

$$\boxed{\Delta f = f_0\left(1 - exp\left[-\frac{2}{3Q^2} \times \left(\frac{\Delta V}{A}\right)^2\right]\right).} \tag{6.33}$$

To check if (6.33) is valid, simulation was performed for varying ΔV, and varying Q. The simulated results (Fig. 6.18) indicate that, even with many approximations mentioned earlier, (6.33) still manages to predict the actual values within a factor of two, and captures the right trend of Δf vs. ΔV as well as Δf vs. Q.

As a matter of fact, (6.33) may also explain the mechanisms of flicker-noise up-conversion. Since flicker noise dominates over thermal noise at low frequencies, then they are almost like a DC mismatch at the threshold voltages for the FETs. Therefore, the fact that (6.33) shows ΔV causes a shift in f_0 indicates low-frequency flicker noise can cause the spectrum of oscillation to not just limited at f_0, but spread a certain range on the spectrum, which is equivalent to having a phase noise at the oscillation output.

CHAPTER 7

Conclusion

7.1 Innovative Claims

In summary, this work was motivated by the demand of next-generation biomedical implants to have a robust wireless power and data interface. It started with theoretical analysis of coupled resonators, and then guided by theories realized a successful design of robust wireless power and a robust design methodology that extends the power level from mW to W. Utilizing a unique property of the implemented wireless power system, it proposed and implemented a novel data modulation scheme, Load-Induced Resonance-Shift Keying (L-RSK), which, for the first time, enables the simultaneous regulated poewr and high-rate reverse data flow over the same pair of coupled coils. Finally, it went back to the theories related to LC oscillators and analyzed their second harmonics.

Below are the major innovations of this work that can hopefully contribute something useful to the scientific and engineering community:

- It introduced a design-oriented analysis on coupled resonators which offers good intuitions on how they work.
- It realized a robust wireless power transfer system that self-regulates against distance variations, misalignment, and load changes, with much extended range.
- It proposed L-RSK, a new data modulation scheme for simultaneous, high-rate, low-power, reverse data transmission, through only a single pair of coils.
- It presented a robust design methodology for wireless power system to easily scale up

the transferred power (by more than 100×).

- It analyzed the second (even) harmonics in LC oscillators, which provides valuable insights on how to improve power-conversion efficiency for oscillator drivers in power systems and on how to explain the mechanisms of flicker-noise up-conversion.

7.2 Future Improvements

It is the author's belief that this work is still imperfect, but hopefully it can at least lighten up a spark in a new field, and eventually let it become a prairie fire. Among many possible directions for improvements, there are a few worth noting here:

- In terms of the theories, this work has developed theories for coupled resonators that provide both design-oriented advice and good intuitions. However, there is still room for improving the analyses on the second harmonics in oscillators. The theories in Chapter 6 involve some approximations (e.g. it assumed that $V_{th} \approx 0$) and future work can take into considerations of more non-idealities.

- In terms of the wireless power design, this work has presented robust wireless power systems for biomedical implants (mW-level power), and for portable consumer electronics (Watt-level power). If possible, it would be interesting to further scale up the power level to kilo-Watt level, so that it can be used for electric vehicle charging. The unique advantage of the given system is its immunity against change in coil separation and against load variations. If it can be successfully scaled to power up electric vehicles (EV), it has the potential to revolutionize the existing static charging scheme where EVs can only be charged when parked, and makes it possible that EVs can also be powered while driving on the roads. It may be envisioned that large coils can be buried consecutively under roads, each taking care of a certain range (because the proposed system is agnostic to change in distance up to a certain range). When a EV is driving on the road, it will be wirelessly and seamlessly charged. This may solve the problem

that EVs require too long wait time for charging; now they can be charged almost everywhere, even while driving.

- In terms of the L-RSK and reverse data system, one future possible improvement is to make the oscillation quenching adiabatic. Right now, the oscillation quenching needs to drain all the stored energy in the LC tanks. This can cause a 5% to 10% reduction in the wireless power transfer efficiency. If, during oscillation quenching, rather than wasting all the energy, it can be transferred to some other temporary storage, then during oscillation start-up, the stored energy can be recycled. This will improve the power transfer efficiency while reverse data is being sent.

BIBLIOGRAPHY

[1] A. E. Mendrela et al. "A Bidirectional Neural Interface Circuit With Active Stimulation Artifact Cancellation and Cross-Channel Common-Mode Noise Suppression". In: *IEEE Journal of Solid-State Circuits* 51.4 (Apr. 2016), pp. 955–965.

[2] W. Chen et al. "A Fully Integrated 8-Channel Closed-Loop Neural-Prosthetic CMOS SoC for Real-Time Epileptic Seizure Control". In: *IEEE Journal of Solid-State Circuits* 49.1 (Jan. 2014), pp. 232–247.

[3] B. C. Johnson et al. "An implantable 700µW 64-channel neuromodulation IC for simultaneous recording and stimulation with rapid artifact recovery". In: *Symposium on VLSI Circuits*. June 2017, pp. C48–C49.

[4] P. Cong et al. "A 32-channel modular bi-directional neural interface system with embedded DSP for closed-loop operation". In: *ESSCIRC 2014 - 40th European Solid State Circuits Conference (ESSCIRC)*. Sept. 2014, pp. 99–102.

[5] D. Rozgić et al. "A True Full-duplex 32-channel 0.135cm^3 Neural Interface". In: *2017 IEEE Biomedical Circuits and Systems Conference (BioCAS)*. Oct. 2017, pp. 1–4.

[6] N. I. Korman. "Coupled Resonant Circuits for Transmitters". In: *Proceedings of the IRE* 31.1 (Jan. 1943), pp. 28–32.

[7] JR. George E. Valley and Henry Wallman. *Vacuum Tube Amplifiers*. McGraw-Hill Book Company Inc., 1948.

[8] R.A. Martin and R.D. Teasdale. "Input Admittance Characteristics of a Tuned Coupled Circuit". In: *Proceedings of the IRE* 40.1 (Jan. 1952), pp. 57–61.

[9] Seymour B. Cohn. "Direct-Coupled-Resonator Filters". In: *Proceedings of the IRE* 45.2 (Feb. 1957), pp. 187–196.

[10] Douglas C. Galbraith, M. Soma, and Robert L. White. "A Wide-Band Efficient Inductive Transdennal Power and Data Link with Coupling Insensitive Gain". In: *Biomedical Engineering, IEEE Transactions on* BME-34.4 (Apr. 1987), pp. 265–275.

[11] B.L. Cannon et al. "Magnetic Resonant Coupling As a Potential Means for Wireless Power Transfer to Multiple Small Receivers". In: *Power Electronics, IEEE Transactions on* 24.7 (July 2009), pp. 1819–1825. ISSN: 0885-8993. DOI: 10.1109/TPEL.2009.2017195.

[12] A.P. Sample, D.A. Meyer, and J.R. Smith. "Analysis, Experimental Results, and Range Adaptation of Magnetically Coupled Resonators for Wireless Power Transfer". In: *Industrial Electronics, IEEE Transactions on* 58.2 (Feb. 2011), pp. 544–554.

[13] J. Kim et al. "A Splitting Frequencies-Based Wireless Power and Information Simultaneous Transfer Method". In: *IEEE Transactions on Circuits and Systems I: Regular Papers* (2018), pp. 1–12.

[14] R.D. Middlebrook. "Low-entropy expressions: the key to design-oriented analysis". In: *Frontiers in Education Conference, 1991. Twenty-First Annual Conference. 'Engineering Education in a New World Order.' Proceedings.* Sept. 1991, pp. 399–403.

[15] MIT Dept. of EE Staff. *Magnetic Circuits and Transformers*. New York, NY: Wiley, 1943.

[16] Jiacheng Pan. "A General Theory of Wireless Power Transfer via Inductive Links". MA thesis. University of California, Los Angeles, June 2015.

[17] R.D. Middlebrook. "The general feedback theorem: a final solution for feedback systems". In: *Microwave Magazine, IEEE* 7.2 (Apr. 2006), pp. 50–63.

[18] R.D. Middlebrook. "Null double injection and the extra element theorem". In: *Education, IEEE Transactions on* 32.3 (Aug. 1989), pp. 167–180.

[19] Y. K. Lo et al. "22.2 A 176-Channel 0.5cm^3 0.7g Wireless Implant for Motor Function Recovery after Spinal Cord Injury". In: *2016 IEEE International Solid-State Circuits Conference (ISSCC)*. Jan. 2016, pp. 382–383.

[20] K. G. Moh et al. "12.9 A Fully Integrated 6W Wireless Power Receiver Operating at 6.78MHz with Magnetic Resonance Coupling". In: *2015 IEEE International Solid-State Circuits Conference - (ISSCC) Digest of Technical Papers*. Feb. 2015, pp. 1–3.

[21] C. Huang, T. Kawajiri, and H. Ishikuro. "A Wireless Power Transfer System with Enhanced Response and Efficiency by Fully-Integrated Fast-Tracking Wireless Constant-Idle-Time Control for Implants". In: *2016 IEEE Symposium on VLSI Circuits (VLSI-Circuits)*. June 2016, pp. 1–2.

[22] M. Kiani, Uei-Ming Jow, and M. Ghovanloo. "Design and Optimization of a 3-Coil Inductive Link for Efficient Wireless Power Transmission". In: *Biomedical Circuits and Systems, IEEE Transactions on* 5.6 (Dec. 2011), pp. 579–591.

[23] André Kurs et al. "Wireless Power Transfer via Strongly Coupled Magnetic Resonances". In: *Science* 317.5834 (2007), pp. 83–86.

[24] A.K. RamRakhyani, S. Mirabbasi, and Mu Chiao. "Design and Optimization of Resonance-Based Efficient Wireless Power Delivery Systems for Biomedical Implants". In: *Biomedical Circuits and Systems, IEEE Transactions on* 5.1 (Feb. 2011), pp. 48–63.

[25] Juseop Lee et al. "Impedance-Matched Wireless Power Transfer Systems Using an Arbitrary Number of Coils With Flexible Coil Positioning". In: *Antennas and Wireless Propagation Letters, IEEE* 13 (2014), pp. 1207–1210.

[26] X. Li, C. Y. Tsui, and W. H. Ki. "12.8 Wireless Power Transfer System Using Primary Equalizer for Coupling- and Load-Range Extension in Bio-Implant Applications". In: *2015 IEEE International Solid-State Circuits Conference - (ISSCC) Digest of Technical Papers*. Feb. 2015, pp. 1–3.

[27] J. H. Choi et al. "A Resonant Regulating Rectifier (3R) Operating at 6.78 MHz for a 6W Wireless Charger with 86% Efficiency". In: *2013 IEEE International Solid-State Circuits Conference Digest of Technical Papers*. Feb. 2013, pp. 64–65.

[28] L. Cheng et al. "21.7 A 6.78MHz 6W Wireless Power Receiver with a 3-level 1× / 1/2× / 0× Reconfigurable Resonant Regulating Rectifier". In: *2016 IEEE International Solid-State Circuits Conference (ISSCC)*. Jan. 2016, pp. 376–377.

[29] M. Kiani et al. “12.7 A Power-Management ASIC with Q-Modulation Capability for Efficient Inductive Power Transmission”. In: *Solid- State Circuits Conference - (ISSCC), 2015 IEEE International*. Feb. 2015, pp. 1–3.

[30] N. Liu and T. G. Habetler. “Design of a Universal Inductive Charger for Multiple Electric Vehicle Models”. In: *IEEE Transactions on Power Electronics* 30.11 (Nov. 2015), pp. 6378–6390.

[31] C.M. Zierhofer and E.S. Hochmair. “The class-E concept for efficient wide-band coupling-insensitive transdermal power and data transfer”. In: *Engineering in Medicine and Biology Society, 1992 14th Annual International Conference of the IEEE*. Vol. 2. Oct. 1992, pp. 382–383.

[32] C.M. Zierhofer and E.S. Hochmair. “High-efficiency coupling-insensitive transcutaneous power and data transmission via an inductive link”. In: *Biomedical Engineering, IEEE Transactions on* 37.7 (July 1990), pp. 716–722.

[33] Dukju Ahn and Songcheol Hong. “Wireless Power Transmission With Self-Regulated Output Voltage for Biomedical Implant”. In: *Industrial Electronics, IEEE Transactions on* 61.5 (May 2014), pp. 2225–2235.

[34] F.W. Grover. *Inductance Calculations: Working Formulas and Tables*. Dover phoenix editions. Dover Publications, 2004.

[35] J. Pan et al. “An inductively-coupled wireless power-transfer system that is immune to distance and load variations”. In: *IEEE International Solid-State Circuits Conference (ISSCC)*. Feb. 2017, pp. 382–383.

[36] S. Mandal and R. Sarpeshkar. “Power-Efficient Impedance-Modulation Wireless Data Links for Biomedical Implants”. In: *IEEE Transactions on Biomedical Circuits and Systems* 2.4 (Dec. 2008), pp. 301–315.

[37] A. Yousefi et al. “A Distance-immune Low-power 4-Mbps Inductively-coupled Bidirectional Data Link”. In: *Symposium on VLSI Circuits*. June 2017, pp. C60–C61.

[38] Y. K. Lo et al. “A Fully Integrated Wireless SoC for Motor Function Recovery After Spinal Cord Injury”. In: *IEEE Transactions on Biomedical Circuits and Systems* 11.3 (June 2017), pp. 497–509.

[39] R. Muller et al. “A Minimally Invasive 64-Channel Wireless µECoG Implant”. In: *IEEE Journal of Solid-State Circuits* 50.1 (Jan. 2015), pp. 344–359.

[40] Y. P. Lin and K. T. Tang. “An Inductive Power and Data Telemetry Subsystem With Fast Transient Low Dropout Regulator for Biomedical Implants”. In: *IEEE Transactions on Biomedical Circuits and Systems* 10.2 (Apr. 2016), pp. 435–444.

[41] F. Inanlou and M. Ghovanloo. “Wideband Near-Field Data Transmission Using Pulse Harmonic Modulation”. In: *IEEE Transactions on Circuits and Systems I: Regular Papers* 58.1 (Jan. 2011), pp. 186–195.

[42] M. Kiani and M. Ghovanloo. “A 13.56-Mbps Pulse Delay Modulation Based Transceiver for Simultaneous Near-Field Data and Power Transmission”. In: *IEEE Transactions on Biomedical Circuits and Systems* 9.1 (Feb. 2015), pp. 1–11.

[43] S. Ha et al. “Energy Recycling Telemetry IC With Simultaneous 11.5 mW Power and 6.78 Mb/s Backward Data Delivery Over a Single 13.56 MHz Inductive Link”. In: *IEEE Journal of Solid-State Circuits* 51.11 (Nov. 2016), pp. 2664–2678.

[44] A. Mirzaei et al. “The Quadrature LC Oscillator: A Complete Portrait Based on Injection Locking”. In: *IEEE J. of Solid-State Circuits* 42.9 (Sept. 2007), pp. 1916–1932.

[45] J. T. Hwang et al. “21.8 An all-in-one (Qi, PMA and A4WP) 2.5W fully integrated wireless battery charger IC for wearable applications”. In: *2016 IEEE International Solid-State Circuits Conference (ISSCC)*. Jan. 2016, pp. 378–380.

[46] M. Huang et al. “22.4 A reconfigurable bidirectional wireless power transceiver with maximum-current charging mode and 58.6% battery-to-battery efficiency”. In: *2017 IEEE International Solid-State Circuits Conference (ISSCC)*. Feb. 2017, pp. 376–377.

[47] Thierry Roz. “Using low power transponders and tags for RFID applications”. In: (Mar. 2018).

[48] L. Fanori and P. Andreani. “Class-D CMOS Oscillators”. In: *IEEE Journal of Solid-State Circuits* 48.12 (Dec. 2013), pp. 3105–3119.

[49] D. Murphy, J. J. Rael, and A. A. Abidi. “Phase Noise inLCOscillators: A Phasor-Based Analysis of a General Result and of Loaded$Q$”. In: *IEEE Transactions on Circuits and Systems I: Regular Papers* 57.6 (June 2010), pp. 1187–1203.

[50] A. Hajimiri and T. H. Lee. “A general theory of phase noise in electrical oscillators”. In: *IEEE Journal of Solid-State Circuits* 33.2 (Feb. 1998), pp. 179–194.